

Stable crack growth geometries as a strategy to circumvent FIB artefacts in small scale fracture testing

Zur Erlangung des akademischen Grades einer
DOKTORIN DER INGENIEURWISSENSCHAFTEN (Dr.-Ing.)

von der KIT-Fakultät für Maschinenbau des
Karlsruher Instituts für Technologie (KIT)
angenommene

DISSERTATION

von

Eloho Okotete, M.Sc.,
geboren am 16. Oktober 1990 in Ughelli, Nigeria

Tag der mündlichen Prüfung:	13. Juni, 2024
Hauptreferentin:	Prof. Dr. Christoph Kirchlechner
Koreferent:	Priv. Doz. Dr. Steffen Brinckmann

Abstract

The present thesis is focused on stable crack growth geometries studied through *in-situ* micro cantilever bending experiments. Multiple experiments are conducted on cantilever geometries inside a Scanning Electron Microscope (SEM) to extract fracture properties of different material systems. The first part of the experiments uses bridge notches to reduce the effect of notch artefacts from focused ion beam (FIB) milled notches on fracture experiments conducted using single cantilever beam geometries. Secondly, the liquid metal ion (Ga^+) source of the FIB is replaced by a gas field ion source (GFIS) (Ne^+) to determine the role of notching ion species on fracture experiments using the single cantilever beam geometry. Single crystalline silicon is used as test material for both set of experiments where the single cantilever beam geometry was used. In the last set of experiments, a test protocol for stable crack growth experiments using a new micro cantilever geometry is presented. After preliminary finite element method (FEM) calculations, the geometry is validated on a hard-coating substrate material system. Subsequently, extensive FEM calculations are used to provide guidelines where the geometry can be successfully used for stable crack growth experiments.

The results show that crack arrest is observed in cantilevers with deep notches and thin material bridges. In the case of shallow notches with similar material bridges, crack arrest was not observed experimentally, but the fracture toughness for silicon was within the same range as deep notches ($1.1 \pm 0.1 \text{ MPa m}^{0.5}$). Thicker bridges lead to a geometry-dependent apparent fracture toughness about 50 % higher than the expected value for single crystalline silicon. Changing notching ion species from gallium to neon creates sharper notches, but the silicon-neon interactions produce an ion-induced damage layer that promotes the formation of neon-containing bubbles at the notch front. This damage layer increases the apparent fracture toughness of a sharp notch. Thermal treatment is shown to release trapped neon from the damaged layer producing a sharp notch front, and measured fracture toughness is similar to values calculated for gallium notches. These findings document the need for in-depth analysis of ion effect during micro cantilever testing using noble gas ions such as Ne^+ .

The suitability of the new single cantilever delamination geometry for stable crack growth experiments is demonstrated. The crack driving force reduces with crack extension in the geometry preventing catastrophic failure. As a result, a natural crack is formed from the FIB notch and final fracture occurs after the crack has grown beyond the region of the FIB milled notch. This reduces the influence of FIB-induced artefacts such as residual stresses due to ion implantation, finite notch radius, crystalline defects redeposition on the fracture toughness of materials tested at small length scales. Additionally, the new geometry shows evidence of crack deflection as a natural crack grows away from the FIB-affected zone. Interface delamination occurs in a stable manner, and interface toughness between 3–7 J/m^2 . Finite element calculations show that interface crack nucleation in the new geometry requires a short cantilever length, short crack length, thick film, and large angle between the film and substrate. A high film modulus also prevents crack branching into the film. After crack nucleation at the interface, delamination continues along the interface as the crack driving force reduces. For very long cracks, the cantilever becomes more compliant, and film fracture may become possible.

Kurzfassung

Die vorliegende Arbeit befasst sich mit stabilen Risswachstumsgeometrien, die durch in-situ-Mikrobiegeexperimente untersucht werden. Es werden mehrere Experimente an unterschiedlichen Geometrien in einem Rasterelektronenmikroskop (REM) durchgeführt, um Brucheigenschaften verschiedener Materialsysteme zu ermitteln. Im ersten Teil der Experimente werden Brückenkerben verwendet, um die Auswirkung von Kerbartefakten aus mit dem fokussierten Ionenstrahl (FIB) gefrästen Kerben auf Bruchexperimente zu verstehen, die mit einzelnen Kragarmgeometrien durchgeführt werden. Zweitens wird die Flüssigmetall-Ionenquelle (Ga^+) des FIB durch eine Gasfeld-Ionenquelle (Ne^+) ersetzt, um die Rolle der Ionenspezies bei Bruchexperimenten zu bestimmen. Einkristallines Silizium wird als Testmaterial für beide Versuchsreihen verwendet. Im letzten Kapitel wird ein Versuchsaufbau für Experimente zum stabilen Risswachstum unter Verwendung einer neuen Geometrie vorgestellt. Nach ersten Finite-Elemente-Methode (FEM)-Berechnungen wird die Geometrie an einer Hartstoffschicht auf Silizium als Modellmaterial validiert. Anschließend werden umfangreiche FEM-Berechnungen durchgeführt, um Leitlinien für den erfolgreichen Einsatz der Geometrie für Experimente zum stabilen Risswachstum zu erstellen.

Die Ergebnisse zeigen, dass Proben mit tiefen Kerben und dünnen Materialbrücken ein Rissstillstand beobachtet wird. Bei flachen Kerben mit ähnlichen Materialbrücken wurde der Risstopp experimentell nicht beobachtet, aber die Bruchzähigkeit für Silizium lag im selben Bereich wie bei tiefen Kerben ($1,1 \pm 0,1 \text{ MPa m}^{0,5}$). Dickere Brücken führen zu einer geometrieabhängigen scheinbaren Bruchzähigkeit, die etwa 50 % höher ist als der erwartete Wert für einkristallines Silizium. Der Wechsel der Kerb-Ionenspezies von Gallium zu Neon erzeugt schärfere Kerben, aber die Silizium-Neon-Wechselwirkungen erzeugen eine ioneninduzierte Schadensschicht, die die Bildung neonhaltiger Blasen an der Kerbfront fördert. Diese Schädigungsschicht erhöht die scheinbare Bruchzähigkeit einer scharfen Kerbe. Durch thermische Behandlung wird das eingeschlossene Neon aus der beschädigten Schicht freigesetzt, wodurch eine scharfe Kerbfront entsteht. In diesem Fall entspricht die gemessene Bruchzähigkeit den für Galliumkerben gemessenen Werten. Diese Ergebnisse belegen die Notwendigkeit einer eingehenden Analyse der Ionenwirkung bei der Prüfung von Mikro-Cantilevern mit Edelgasionen wie Ne^+ .

Die Eignung der neuen einseitig auskragenden Delaminationsgeometrie für Experimente zum stabilen Risswachstum wird nachgewiesen. Die Rissantriebskraft nimmt mit der Rissausdehnung in der Geometrie ab, was ein katastrophales Versagen verhindert. Infolgedessen bildet sich ein natürlicher Riss aus der FIB-Kerbe, und der endgültige Bruch erfolgt, nachdem der Riss über den Bereich der FIB-Fräskerbe hinausgewachsen ist. Dadurch wird der Einfluss von FIB-induzierten Artefakten wie Eigenspannungen aufgrund von Ionenimplantation, endlichen Kerbradien und anderen kristallinen Defekten auf die Bruchzähigkeit von Materialien, die auf der Mikroebene getestet werden, reduziert. Darüber hinaus zeigt die neue Geometrie Anzeichen von Rissablenkung, wenn ein natürlicher Riss von der FIB-beeinflussten Zone weg wächst. Die Delamination der Grenzflächen erfolgt auf stabile Weise, und die Grenzflächenzähigkeit liegt zwischen 3-7 J/m². Finite-Elemente-Berechnungen zeigen, dass die Bildung von Rissen an der Grenzfläche in der neuen Geometrie eine kurze Auskrägung, eine kurze Risslänge, eine dicke

Schicht und einen großen Winkel zwischen der Schicht und dem Substrat erfordert. Ein hohes Elastizitätsmodul des Films verhindert auch die Rissverzweigung in den Film. Nach der Rissentstehung an der Grenzfläche setzt sich die Delamination entlang der Grenzfläche fort, da die Rissantriebskraft abnimmt. Bei sehr langen Rissen wird die Auskrägung nachgiebiger, und es kann zum Bruch der Dünnschicht kommen.

Table of Contents

Abstract	i
Kurzfassung	ii
Table of Contents	iv
List of Figures	viii
List of Tables	xii
List of abbreviations	xiii
List of notations	xiv
Acknowledgements	xv
1.0 Motivation	1
2.0 Fundamentals and Background	3
2.1 Linear elastic fracture mechanics	3
2.2 Small scale fracture	4
2.3 Sample fabrication methods for micro fracture test specimens	5
2.3.1 Lithography	6
2.3.2 Deep reactive ion etching	7
2.3.3 Focused ion beam milling (FIB)	8
2.3.4 Femtosecond laser ablation	8
2.4 Current methods to measure fracture toughness in single phase materials	9
2.4.1 Semi-quantitative methods	9
2.4.2 Quantitative methods at the micron scale	10
2.4.3 Notches	14
2.5 Current methods to measure fracture toughness in interfaces and multi-layered materials	16
2.5.1 Semi-qualitative methods	16
2.5.2 Quantitative methods	19
2.6 Artefacts in FIB-based small scale fracture testing	20
2.6.1 Artefacts at notch	20

3.0	Optimisation of bridge notch geometry in single cantilever beams: an approach for minimising FIB artefacts	22
3.1	Introduction	22
3.2	Experimental procedure.	23
	3.2.1 Material	23
	3.2.2 Cantilever preparation	23
	3.2.3 Notching of cantilevers	25
	3.2.4 <i>In situ</i> SEM deformation testing	26
3.3	Results	26
	3.3.1 Fracture response via crack arrest	26
	3.3.2 Effect of notch and bridge geometry on crack arrest	27
	3.3.3 Experiments vs. simulation predictions	32
3.4	Discussion	34
	3.4.1 Crack arrest in single crystalline silicon cantilevers	34
	3.4.2 Geometry for valid fracture measurement	35
	3.4.3 Fracture toughness of silicon	36
3.5	Conclusion	37
4.0	Role of notching ion species on fracture toughness of single crystalline silicon	38
4.1	Introduction	38
4.2	Experimental details	39
	4.2.1 Notching, annealing and <i>in situ</i> SEM testing of cantilevers.	39
4.3	Results	40
	4.3.1 Analysis of data from <i>in situ</i> test	40
	4.3.2 Effects of ion beam aperture size	41
	4.3.3 Effects of ion beam energy	42
	4.3.4 Effects of annealing	46
4.4	Discussion	49
	4.4.1 Sputtering efficiency of silicon using neon ions	49
	4.4.2 Damage evolution and annihilation in silicon	50
	4.4.3 Fracture toughness of neon notched micro cantilevers	50
4.5	Conclusion	51

5.0	Novel single cantilever delamination geometry for fracture toughness measurements	52
5.1	Introduction	52
5.1.1	Validation of single cantilever delamination (SCD) geometry.	53
5.2	Experimental procedure.	54
5.2.1	Material	54
5.2.2	Cantilever preparation	55
5.2.3	Micro fracture tests	57
5.3	Results	59
5.3.1	Observation of stable crack growth	59
5.3.2	Quantitative analysis of interface toughness	61
5.4	Discussion	65
5.4.1	Stable crack growth	65
5.4.2	Crack deflection at interface	65
5.4.3	Interface toughness	66
5.5	Conclusion	66
6.0	Numerical analysis of single cantilever delamination (SCD) geometry	68
6.1	Introduction	68
6.2	FEM Model	69
6.2.1	Modelling experimental data	71
6.3	Results	72
6.3.1	Stress distribution at the crack tip	72
6.3.2	Stress intensity analysis of the SCD geometry	72
6.3.3	Relationship between stress intensity factor of SCB geometry and critical geometry and material parameters	75
6.3.4	Comparing fracture toughness from experimental result and simulation calculations.	78
6.4	Discussion	79
6.4.1	Guidelines for geometry optimization	79
6.4.2	Interface fracture toughness	81
6.5	Conclusion	81

7.0	Summary and outlook	82
7.1	Summary	82
7.2	Outlook	83
	References	84
	Appendix	103
	Contribution of co-authors	103
	List of Publications	1044

List of Figures

Figure 2.1: Description of stress fields at a crack tip, reprinted from [1] 4

Figure 2.2: Schematic of steps to fabricate a micro sample on a substrate using lithography 7

Figure 2.3:(a) Schematic representation and (b) SEM image single cantilever beam fabricated by combination of lithography and FIB 11

Figure 2.4: (a) Schematic representation of a clamped beam cantilever showing the bending direction and (b) SEM image of same cantilever, reprinted from [33]. 11

Figure 2.5: Schematic representation of a DCB showing bending direction for (a) wedge tip, (b) flat punch, while SEM images of the two variations of the DCB specimen during testing is shown in (c) and (d), reprinted from [97] and [33] 13

Figure 2.6: (a) Sketch of a pillar with a pyramidal tip and (b)SEM of a pillar at the beginning of an *in situ* test, reprinted from [103]. 14

Figure 2.7: (a) *Post mortem* SEM image of a through notch fractured in a rectangular single cantilever beam (reprinted from [75]), and (b) SEM image of a through notch fractured in a pentagonal single cantilever beam (reprinted from [85]) 15

Figure 2.8: *Post mortem* SEM image of bridge notched silicon microcantilever 15

Figure 2.9: *Post mortem* SEM image of samples with chevron notches in (a) rectangular, (b) pentagonal and (c) triangular single cantilever beams, reprinted from [108], [110], [85], respectively. 16

Figure 2.10: Schematic representation of a peel test set up, reprinted from [124]. 17

Figure 2.11: Schematic of scratch test, reprinted from [128] 18

Figure 2.12: Schematic of the delamination evolution in a brittle coating on a hard substrate scratch test, reprinted from [123]. 19

Figure 2.13: (a) and (b) SEM image of single cantilever beam containing an interface before and after fracture test (reprinted from [135]), and (c), (d) and (e) Transmission electron microscope (TEM) image showing stages of interface fracture (reprinted from [137]) 20

Figure 3.1: (a) SEM image of one sample etched by DRIE (b) cantilevers in one row of etched sample and (c) a single free standing cantilever showing sharp edges. 25

Figure 3.2: Schematic drawing of the cantilever geometry from Figure 3.1c showing the designations of the geometry; W — beam thickness, B — beam width, b — notch width, L — beam length, and a — notch length. The black arrow represents the loading direction and the contact point 26

Figure 3.3: (a) Load – displacement plot from experiment, (b) SEM image of cantilever at the start of test, (c) SEM image after failure of bridge 1 at F_{B1} , (d) SEM image showing extension of crack at F_{B1} and failure of bridge 2 at F_{B2} and (e) SEM image of fractured cross section	27
Figure 3.4: K_{IQ} assuming through-thickness notch for samples with different bridge and notch geometries. Filled circles and unfilled circles represent observation and absence of crack arrest, respectively. For filled circles, the assumption of through-thickness notch is fulfilled	30
Figure 3.5: Corrected apparent fracture toughness ($K_{IQ_corrected}$) for samples where crack arrest was not observed (unfilled circles), and K_{IQ} for samples where crack arrest was observed (filled circles) where geometry correction was not needed	31
Figure 3.6: (a) shallow notch, thin bridge, (b) shallow notch, thin bridge (c) deep notch, thin bridge and (d) deep notch, thick bridge	32
Figure 3.7: Cumulative probability function of the fracture toughness at the bridge (K_{IC}^*) and the notch (K_{IC})	33
Figure 3.8: Cumulative probability function of the stress intensity ratio	34
Figure 3.9: Cumulative distribution of fracture toughness in silicon cantilevers with crack arrest assuming a through thickness notch (K_{IC}), and apparent fracture toughness (K_{IQ} and $K_{IQ_corrected}$) for cantilevers without crack arrest	36
Figure 4.1: Load-displacement plot of a neon bridge-notched silicon cantilever showing crack arrest	41
Figure 4.2: Cumulative distribution of influence of aperture diameter on apparent fracture toughness of silicon. Note that bridge failure and subsequent crack arrest was not observed in these samples	42
Figure 4.3: SEM images showing the top view of notches milled at beam energies (acceleration voltages) of (a) 10 kV, (b) 15 kV and (c) 25 kV. (d) Cross-section SEM image showing sub-surface damage in a fractured cantilever	43
Figure 4.4: Cumulative distribution of through-thickness fracture of toughness and bridge fracture toughness of silicon cantilevers notched with different beam energies	44
Figure 4.5: Cumulative distribution of corrected and uncorrected apparent fracture of toughness of silicon cantilevers notched with different beam energies	45
Figure 4.6: Fracture cross section of cantilevers milled with (a) 10 kV, (b) 15 kV and (c) 25 kV beam energies	46
Figure 4.7: A sketch of damage layers after neon ion beam interaction	46

Figure 4.8: Influence of annealing on fracture morphology of cantilevers notched using different acceleration voltages	47
Figure 4.9: Cumulative distribution of through-thickness fracture toughness of as-milled and annealed notches averaged for different acceleration voltages.	48
Figure 4.10: Cumulative distribution of fracture toughness of 25 kV milled through-thickness notches, before and after annealing.	49
Figure 5.1: Sketch of the SCD geometry showing the crack length a lying on the interface (blue line) between the substrate and film, adapted from [208]	53
Figure 5.2: Crack driving force in SCD as a function of crack length; experimental window shown with dashed rectangle, reprinted from [208]	54
Figure 5.3: Steps to achieve the SCD geometry from cut sample piece, to etched geometry and finally milled cantilever, adapted from [208].	55
Figure 5.4: (a) Milling strategy to avoid redeposition in cantilevers and (b) SEM image showing side view of milled cantilever with film and substrate labelled	56
Figure 5.5: SEM image with top plane sketch of (a) through notch and (b) chevron notch, reprinted from [208]	57
Figure 5.6: (a) Side view SEM image of custom made wedge tip and (b) front view of wedge aligned to a cantilever for <i>in situ</i> test	58
Figure 5.7: Indenter positioned to measure the compliance of the tapered specimen, reprinted from [208]	59
Figure 5.8: (a) Load-displacement plot of a through notched cantilever showing partial unload segments with points of different events during <i>in situ</i> test labelled and (b–h) SEM image of crack extension in the cantilever, reprinted from [208]	60
Figure 5.9: (a) Load-displacement of a chevron notched cantilever plot showing partial unload segments with points of different events during <i>in situ</i> test labelled and (b–h) SEM image of crack extension in the cantilever, reprinted from [208]	61
Figure 5.10: Effective crack length measured from SEM, calculated from unloading slope and compliance corrected, adapted from [208]	62
Figure 5.11: Critical energy release rate plotted as a function of effective crack length of interface, reprinted from [208]	63
Figure 5.12: (a) Interface toughness, G_{c_H} for all cantilevers (reprinted from [208]) and (b) cumulative distribution of energy loss (ΔH) during crack growth for all cantilevers with different notch shape.	64

Figure 5.13: (a) sketch of the top plane of straight notch showing the actual notch (AC*D*B) and (b) SEM image showing crack propagation along the assumed plane notch before deflection, reprinted from [208]	66
Figure 6.1: Schematic representation of the single cantilever beam geometry with an amplified crack-opening presented in the previous chapter showing applied boundary conditions for FEM simulation and the designations on the geometry are defined as follows; W —beam thickness, S_W —sample thickness, S_L —sample length, P —applied load, L — free cantilever length (distance from loading point to the substrate), a —crack length, a^* —effective crack length and α —angle between substrate and film	69
Figure 6.2: A crack with coordinates x and y describing the deformation field at the crack tip, and Γ showing the contour used for line integral evaluation	70
Figure 6.3: Meshed geometry with focused mesh at the crack tip	71
Figure 6.4: Stress distribution profile for a crack extending along the interface (a) and (b) perpendicular to the interface	72
Figure 6.5: Influence of cantilever and crack length on (a) stress intensity of interface crack and (b) stress intensity of film fracture. Figure (b) shows also the individual simulation parameters that were used to create the contour diagram	73
Figure 6.6: Influence of substrate angle and film thickness on the stress intensity factor of (a) interface crack and (b) film crack. Figure (b) shows also the individual simulation parameters that were used to create the contour diagram	74
Figure 6.7: Influence of elastic modulus and film thickness on stress intensity factor of (a) interface crack and (b) film crack. Figure (b) shows also the individual simulation parameters that were used to create the contour diagram	74
Figure 6.8: FEM simulated points and power law fit function of stress intensity factor in relation to (a) substrate modulus, (b) film modulus, (c) crack length, (d) cantilever length (e) substrate angle, and (f) film thickness.	77
Figure 6.9: Stress intensity factor of SCD geometry calculated from FEM and analytical equation	78
Figure 6.10: Fracture toughness from one experimental sample compared to data extracted from simulation calculations	79
Figure 6.11: Crack driving force for interface and film propagation as a function of increasing crack length	80

List of Tables

Table 3.1: Average fracture toughness calculated for tested samples	29
Table 6.1: Fitting coefficients for simulated parameters.	75
Table 6.2: Comparison of fracture toughness obtained by different methods	81

List of abbreviations

BDT	Brittle to ductile
BOX	Buried oxide layer
DCB	Double cantilever beam
DRIE	Deep reactive ion etching
FEM	Finite element method
FIB	Focused ion beam
GFIS	Gas field ion source
HAZ	Heat affected zone
HIM	Helium ion microscope
ICP	Inductively couple plasma
LIPSS	Laser induced periodic surface structures
LMIS	Liquid ion metal source
MEMS	Micro-electro-mechanical systems
NPVE	Nano patterning visualization engine
PMMA	Polymethyl methacrylate
SCD	Single cantilever delamination
SEM	Scanning electron microscope
SOI	Silicon on insulator
SRIM	Stopping range of ions in matter
TEM	Transmission electron microscope
TRIM	Transport of ions in matter

List of notations

$l-b/B$	Bridge geometry
a^*	Effective crack length
a/W	Notch depth
C_0	Compliance of initial unloading slope
C_B	Compliance of beam
C_{F-C}	Calculated frame compliance
C_{F-M}	Compliance measured from cantilever
C_M	Compliance measured from unloading slope
C_M^*	Corrected measured compliance
E_f	Elastic modulus of film
E_s	Elastic modulus of substrate
$f(a/W)$	geometry correction factor
F_{B1}	Maximum load at bridge 1
F_{B2}	Maximum load at bridge 2
F_C	Maximum load at final fracture
f_{corr}	Bridge geometry correction factor
G_b	Driving force for crack deflection into bulk
G_C	Critical energy release rate
G_{c_H}	Critical energy release rate of interface
G_i	Driving force for interface crack growth
K_I	Stress intensity at mode I
K_{I_film}	Stress intensity for film fracture
K_{I_int}	Stress intensity for interface fracture
K_{IC}	Critical stress intensity factor at mode I
K_{IC}^*	Bridge notch fracture toughness
K_{IC_Exp}	Fracture toughness calculated from experimental data
K_{IC_FEM}	Fracture toughness calculated from FEM
K_{IQ}	Conditional fracture toughness
$K_{IQ_corrected}$	Corrected conditional fracture toughness
L	Free cantilever length
R_i	Interface crack resistance
S_L	Sample length
S_W	Sample thickness
W	Beam thickness
α	Angle between film and substrate
Γ	Contour around a crack tip
γ_s	Surface energy
ΔH	Energy consumed for crack growth
σ_f	Fracture stress

Acknowledgements

First, I would like to express my sincere gratitude to my main supervisor, Prof. Christoph Kirchlechner, for offering me the opportunity to pursue my doctorate studies in his small scale mechanics group at the Max-Planck-Institut für Eisenforschung (MPIE), Düsseldorf, and subsequently inviting me to join him at the Institute of Applied Materials - Mechanics of Materials and Interfaces (IAM-MMI), Karlsruhe Institut für Technologie (KIT). I am grateful for the analytical and research skills he has imparted to me over the past few years, fostering productive discussions and ideas that have made me a better scientist. I also appreciate the atmosphere, facilities, and personnel provided for carrying out high-quality research, despite COVID-19 related setbacks. The opportunities provided for scientific exchange with peers within the institute (seminars and summer schools), and outside the institute (conferences) have all contributed to shaping and balancing my academic experience over the past few years. Lastly, I admire his commitment to unbiased knowledge transfer for raising young scientists in the field of material science. I hope he achieves his goal at the end of his career. I would also like to appreciate Priv. Doz. Dr. Steffen Brinckmann for agreeing to be my second supervisor and for all the contributions he made towards the topic from the first year at MPIE. I extend my special thanks to him for the oversight regarding finite element simulations.

A significant part of my doctorate studies took place in the in-situ microscopy group under the leadership of Dr. Subin Lee. I appreciate him for the discussions and the room he provided for learning and growing in my core project as well as other tasks and responsibilities that have sharpened my overall research skills. Additionally, I am grateful for the group outings and social events organized for team building and relaxation. I am personally glad he accepted the position.

I also thank Leon Christiansen (MPIE) for training and introduction to microscopes, Dr. Subin Lee for training on microscopes and in-situ indenter at IAM-MMI, Dr. Steffen Brinckmann, and Dr. Oleg Birkholz for introduction to Abaqus. I would also like to thank Dr. Judith Hohmann and Dip.-Ing. Muslija Alban in charge of equipment at Karlsruhe Nano Micro Facility, KIT, used for making batch silicon cantilevers.

From the early days, I thank Dr. Reza Hosseinabadi and Dr. Viswanadh Arigela for being great friends who contributed to settling into PhD life at MPIE. I am grateful to Ass. Prof. Hariprasad Gopalan, who was a constant source of encouragement through the different phases of my PhD both at MPIE, and later at KIT. At the KIT, I appreciate all my present and past group members, as well as all the colleagues at IAM-MMI who have contributed to my PhD in diverse ways. I extend my special thanks to my office mate, Camila Aguiar Teixeira, for the discussions, troubleshooting machines, and all the fun times in the office (especially acknowledging who the funny one is). Dr. Ujjval Bansal, Dr. Divya Sri Bandla, Yinxia Zhang, and Angelica Medina Gomez are all appreciated for being open to scientific discussion and sharing ideas on how to better our research.

I would also like to appreciate my lovely parents, Mr. and Mrs. D.O. Okotete, for their love, encouragement, and support throughout the program. My siblings, Omokinovo, Akpobome, Emujevoke, Oghenekevwe, and Ogheneruona, provided the emotional support I needed to push through difficult phases of this program. My friends, specifically Ayomide Osundare, Bolarinwa Ogunlayi, and Femi Ibitolu, who showed up and contributed to fun times outside academics, are greatly appreciated. You all helped prevent burnout during my program. My mentor and life coach, Dr. Stanley Orji, is deeply appreciated for the long conversations that kept me going throughout the years of research.

Finally, I acknowledge the International Max Planck Research School for Interface Controlled Engineering for Energy Conversion (IMPRS-SurMat) for funding the first year of my doctorate studies at the MPIE. I am also deeply grateful to the Robert Bosch Foundation for funding my doctorate research at Karlsruhe Institut für Technologie as well as the KNMFi for providing lithographic facilities.

Karlsruhe, March, 2024

Eloho Okotete

1.0 Motivation

Catastrophic failure that results in the separation of components into two or more parts due to the application of internal or external loads has detrimental consequences in practical applications. These components often fail at stresses below their assumed strength. Therefore, experimental and theoretical concepts have been developed to better understand the mechanics and mechanisms behind such failures, taking into account the role of pre-existing flaws such as micro-voids and micro-cracks [1]. Fracture mechanics is a well-established field today for designing against catastrophic failures in components across several applications.

In fracture mechanics, material failure is attributed to stress heterogeneities in the presence of pre-existing flaws, which lead to crack initiation and crack propagation before a final separation [2]. The measure of a material's resistance to crack extension is known as fracture toughness, and to measure it, sample geometries are designed to meet dimensional requirements from established theories. However, small components used in crucial load-bearing and functional applications in new technologies are only a few millimetres in size. Hence, millimetre-sized sample geometries developed for bulk-scale fracture testing would not suffice for scale fracture studies of small volumes. Also, the size limitation of the sample results in sample size effect which may alter fracture behaviour compared to known bulk fracture properties [3,4]. Therefore, material scientists interested in bridging material properties across different scales prioritise developing geometries and testing setups that adequately fulfil conditions for accurate fracture mechanics experiments [5]. In the absence of standardised specimens for testing samples of a few microns' dimension, several quantitative, semi-quantitative and qualitative approaches are currently used to measure fracture properties of material systems using nanoindentation based techniques.

For the approaches where sample geometries are required for fracture testing, geometries are mostly fabricated using high-energy ions to displace atoms of a target material to form desired sample shapes at the micron scale. This fabrication method enables the creation of precise small structures with high accuracy using a focused ion beam (FIB) microscope [6]. However, high-energy ions can also introduce damage to the target material resulting in a local change in material composition and stresses, making cracks nucleate and grow under conditions not reflective of the target's material property [7,8]. Since material removal by ion bombardment (sputtering) is still the most efficient and effective way for making small test samples, there is a need to find other ways to minimize the influence of this damage on fracture experiments. One way to do this is the growth of a sharp crack from the notch produced by FIB. This is a common strategy used to create sharp cracks from machined pre-notches in macro samples. Sharp cracks are initiated when stable crack growth geometries are used in experimental investigations.

Attempts to measure artefacts at FIB-milled notches using notches or sample geometries at small length scales have not been very successful to date. This thesis intends to address typical concerns associated with fracture toughness investigation of samples produced with focused ions by:

1. Developing protocols to optimise an existing notch type, namely so-called bridge notches, for fracture measurements in an otherwise unstable test geometry.

2. Substituting liquid metal ion source with a gas field ion source (GFIS) for production of notches in an existing fracture test geometry.
3. Designing and validating a new cantilever-based testing protocol for stable crack growth using experiments and finite element method (FEM) calculations.

Single crystalline silicon is used as test material for the first two objectives, because of its significance in micro-electro-mechanical applications and well-established fracture properties across length scales. The last objective was validated using a hard coating-silicon system, where interface delamination can lead to failure.

The first part of this thesis gives some background knowledge on fracture mechanics and summarise the state of the art in small scale fracture (Chapter 2). Subsequently, details on how the single cantilever geometry for micro fracture was optimised for crack arrest is presented and discussed (Chapter 3). The influence of alternate ion species on fracture toughness obtained from the same geometry is discussed in Chapter 4. Chapter 5 presents a new geometry for small scale fracture and guidelines for utilising the geometry (Chapter 6). Summary of all the results is finally provided in Chapter 7.

2.0 Fundamentals and Background

2.1 Linear elastic fracture mechanics

Understanding fracture of materials which show purely linear elastic behaviour was approached using different models about a century ago. One of the earliest concepts which attributed fracture in real materials to the presence of flaws was proposed by Inglis [9]. In his work, stress concentration at elliptical crack tips was identified as the reason why materials fail below their theoretical cohesive strength when subjected to intrinsic or extrinsic stresses. This model, however, predicted infinite stresses at the crack tip of an infinitely sharp crack which did not translate to physical significance in real materials [10]. Motivated by the lapses in Inglis's approach to fracture model in brittle solids, Griffith [11] came up with the energy balance approach based on thermodynamic equilibrium of the energies present in a cracked body. In order to minimise the total energy in a system, a crack will only grow if the elastically stored strain energy in that system (from intrinsic or external stresses) is sufficient to overcome the energy required for the creation of new surfaces. Based on this assumption the critical stress, σ_f for a crack of length a to fracture in a material with elastic modulus E and surface energy γ_s is given by Eqn 2.1 [1].

$$\sigma_f = \left(\frac{2E\gamma_s}{\pi a} \right)^{1/2} \quad (2.1)$$

Since Griffith's concept was based on assumption of ideally brittle materials, only the surface energy requirement was considered for creation of new surfaces. In ductile materials, work done by plastic deformation at the crack also needs to be accounted for. Thus, Eqn 2.1 was individually modified by Irwin and Orowan to include the plastic work done per unit crack surface area as the crack grows [1]. From Griffith's relation (Eqn 2.1), the critical energy release rate (material's toughness) G_c , for crack growth can be calculated (Eqn 2.2) and σ_f can be expressed in terms of the critical energy release rate (Eqn 2.3).

$$G_c = \frac{\sigma^2 \pi a}{E} \quad (2.2)$$

$$\sigma_f = \left(\frac{G_c E}{\pi a} \right)^{1/2} \quad (2.3)$$

Furthermore, Irwin [12] became interested in the analyses of stresses in the immediate vicinity of the crack tip (Figure 2.1). Using formulations already established globally by the energy release rate approach and knowledge from prior works of Sneddon [13] and Westergaard [14] who individually analysed stress distribution near a crack, Irwin was able to develop the now existing crack tip stress field solution for a homogeneous linear elastic material. A generalized form of the solution for crack in opening loading configuration (Mode I) is presented in Eqn 2.4.

$$\sigma_{ij} = \frac{K_I}{\sqrt{2\pi r}} f_{ij}(\theta) \quad (2.4)$$

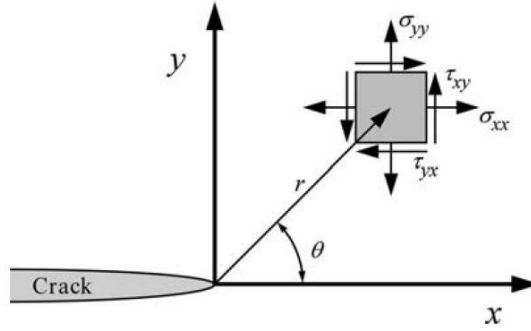


Figure 2.1: Description of stress fields at a crack tip, reprinted from [1].

In Eqn. 2.4, σ_{ij} is the stress tensor at the crack tip, K_I is a scalar describing the stress intensity at mode I, $f_{ij}(\theta)$ is a dimensionless angular function at the crack tip, and r and θ are polar coordinates at the crack tip. As r approaches zero, the stresses at crack tip approaches infinity and this region is known as the singularity zone where the stresses approach singularity with a $1/\sqrt{r}$ dependence. The amplitude of the stress tip singularity is defined by K_I . In a planar crack under tensile loading, the stress intensity factor is a function of the far-field applied stress, crack length a , and a dimensionless geometry parameter Y (Eqn 2.5) [1,2]. A critical value of the stress intensity factor is used to determine the intensity at which an existing crack in a material will grow when subjected to load. The critical stress factor is geometry dependent varying with sample thickness as stress state conditions of crack tip changes. A plane strain fracture toughness representative of intrinsic material's properties can be obtained when the sample thickness is large enough to suppress plastic deformation and promote high stress triaxiality. To achieve this, it is recommended that sample dimensions adhere to requirements in Eqn 2.6 relative to the plastic zone size[15],

$$K_I = Y\sigma \sqrt{\pi a} \quad (2.5)$$

$$a, B, (W - a) \geq 2.5 \left(\frac{K_{IC}}{\sigma_{YS}} \right)^2 \quad (2.6)$$

where B is the sample thickness, $W - a$ is the ligament size, K_{IC} is the critical stress intensity factor and σ_{YS} is the yield strength of the material.

2.2 Small scale fracture

Miniaturized devices which have dimensions ranging from a few micrometres to several hundreds of micrometres are increasingly used in microelectronics, micro-electro-mechanical systems (MEMS), medical devices, and coatings [3]. Thus, the last two decades have been dedicated to understanding how material behaviour changes with scale for effective prediction of reliability. Extrapolating bulk properties to much smaller scale would have been the easiest path to understand material behaviour, however this would not suffice because data from macroscale experiments are usually obtained from large sample volumes with a higher number of defects. As the sample size shrinks approaching characteristic microstructure / defect length scale (for example, grain size or average dislocation spacing), material properties become governed by boundary conditions of the sample volume. The change in material properties as a result of small sample volume is nowadays known as the "sample size effect". Following the work of Uchic et al [16] on micro compression

of single crystal pillars with a few micrometres diameter, plastic deformation in small volumes have been a subject of many studies. These investigations provide a mechanistic-based understanding of material behaviour at small length scales which is useful for predicting reliability of small devices. Additionally, testing of small volumes can be used to understand how constituent microstructural building blocks influence bulk properties of materials [5]. Information extracted using tools available for small scale studies also contributes to extending the frontiers of material science by providing complementary understanding to existing material behaviour concepts.

Size effects may play a critical role in fracture toughness investigations as sample sizes become smaller as well. As the critical sample dimensions get smaller, the plastic zone size becomes large compared to sample dimensions. Consequently, the conditions for valid fracture toughness experiments using linear elastic fracture mechanics assumptions (Eqn 2.6) might get dissatisfied. Once the small scale yielding criterion at the crack tip is no longer fulfilled because of decreased sample size, only an apparent sample thickness dependent fracture toughness is measured. It has also been reported that the defect density of thin samples leads to a change in fracture mechanism observed in some material systems. One study reports that micro-defects present in thin samples caused brittle fracture in metallic foils which was not observed in thicker samples of the same material [17]. Similar change in fracture mode as film thickness is reduced is reported for very thin copper films due to suppressed dislocation activity [18,19]. Furthermore, increase fraction of interfaces and grain boundaries in nanocrystalline thin films do not only suppress dislocation activity at the crack tip, but also promotes intergranular fracture [5,20–22]. Another consequence of small volumes is seen single crystal silicon where there is a downward shift of temperature at which brittle-ductile transition occurs [23,24]. This is because small samples have high surface-volume ratio, and dislocation nucleation at the free surface demands lower energy compared to nucleation within the bulk [25,26]. These size dependent change in fracture behaviour at small scales justifies why there is a need for materials to be tested at the scale which they will be used in real applications [27].

In addition to testing thin films / coatings [28–31], small scale fracture experiments can complement bulk scale experiments to study the influence of microstructural features on global fracture properties [32]. For instance, subcritical crack growth studies at slow crack tip velocities is possible with small samples. In addition, loss of information on fracture behaviour due to overload or during fatigue pre-cracking in bulk scale experiments can be avoided in materials showing stable crack with small scale fracture tests [32,33].

2.3 Sample fabrication methods for micro fracture test specimens

Since scaled down ASTM-approved macroscale test geometries would not suffice in testing volumes, the first step to extracting fracture properties is developing geometries for micro fracture experiments. Hence, advanced micro patterning techniques are required to achieve desired geometries at these scales. Fabricating miniature test samples is made possible by the advent of technologies in the MEMS industry designed for manipulating and structuring small scale devices. Today, most of the available techniques in that industry have either been directly transferred or modified for laboratory use to probe changing mechanical properties at small length scales. A brief

summary of the methods currently used for sample fabrication in the micro fracture community is presented in this section.

2.3.1 Lithography

In this top-down fabrication approach, structures are created on a radiation sensitive organic film (resist) placed on the surface of a substrate using light, electrons or ions [34]. Ultraviolet light exposure of photoresist (light sensitive polymer) through a photomask is commonly used to transfer patterns to substrates through several steps. Electron beam lithography is often used for patterning of smaller features where higher resolution is required because of its much shorter wavelength. Hence, precise and accurate patterning is possible, but this requires more time for creating desired structures [35,36]. Direct writing on the substrate without the use of a mask is another advantage of using the electron beam for fabricating of samples [37]. Figure 2.2 shows the steps to pattern a substrate using electron beam lithography to desired structures. In the first step, a thin layer of electron beam resist is spin coated on the surface of a clean substrate. Then, the coated substrate is exposed to electron beam where the beam is accurately directed to create desired patterns on the substrate. The area of the resist exposed to the electron beam becomes chemically modified enabling solubility in a developer solution [38,39]. Subsequently, the exposed substrate is dipped into an organic solvent which dissolves only the area of the resist modified by electron beam in a development step. After development, either etching or lift off technique is used to transfer desired pattern to the substrate. For the etching method, the area of the substrate not covered by resist is chemically removed, and afterwards the resist is removed from the rest of the substrate to reveal an underlying pattern. In the lift-off method, a metal layer is deposited on the entire area of the substrate after development. Then, the resist is removed along with the metal layer from areas that were not exposed to electron beam in the second step. Leaving a final pattern in the electron beam exposed area [37]. The process described here applies to a positive tone electron beam resist. For a negative tone resist, the unexposed part of the resist is removed in the development step [40]. In some sample fabrication processes, lithography steps are used together with reactive ion etching to create structures with high aspect ratios.

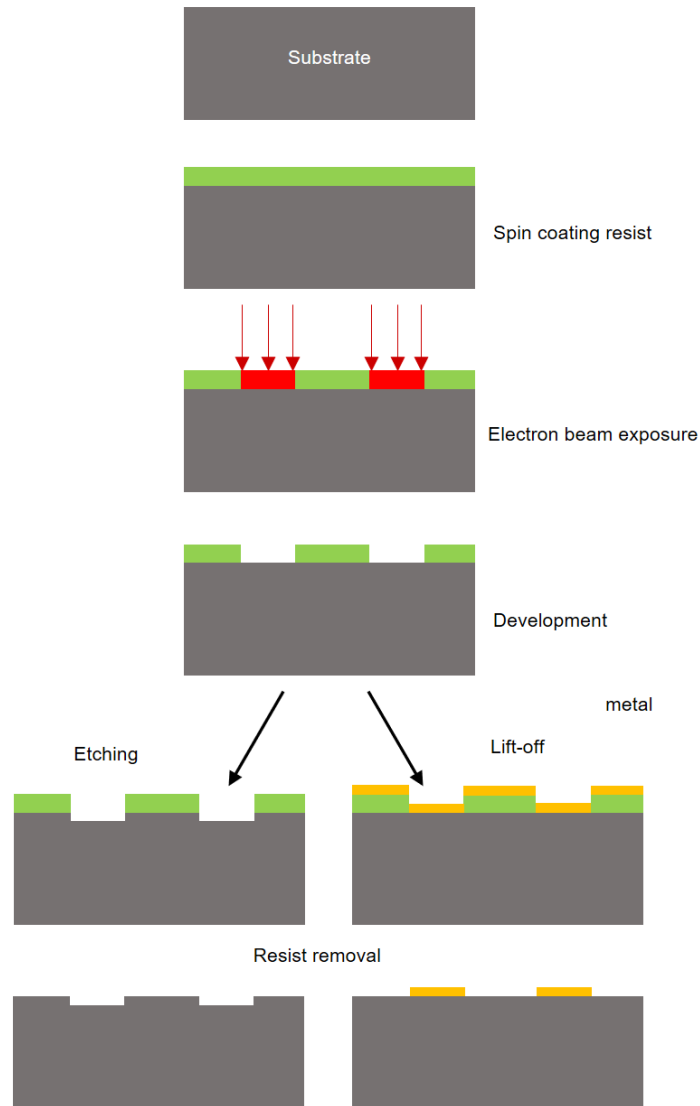


Figure 2.2: Schematic of steps to fabricate a micro sample on a substrate using lithography.

2.3.2 Deep reactive ion etching

The metal deposited in the lift-off step is used to protect parts of the substrate with the desired pattern before dry etching. Dry anisotropic etching using chemically reactive and ionic species produced from a reactive gas in a radio-frequency glow discharge [41–43] is used to fabricate structures on semiconductor materials. Energetic ions from the plasma bombards the substrate to initiate material removal at low chamber pressures (10^{-2} – 10^{-3} Torr) [44,45]. The chemically reacting species reacts with the atoms of the substrate to form reaction by-products that desorb from the surface. Sulphur hexafluoride (SF_6) plasma is used for dry etching silicon at room temperatures. Etching can be by the Bosch process, where a silicon substrate is bombarded with fluorine radicals in the plasma. Fabrication involves alternating steps of etching and passivation of sidewalls to prevent reactions on the surface [46,47]. This two-step process produces scalloped sidewalls on the final sample. An alternative method for etching silicon is cryogenic etching. Here, the substrates are subjected to cryogenic cooling before etching to reduce the reaction of radicals

on the sidewalls, eliminating the need for a passivation step [48]. In cryo etching, oxygen can also be added to the plasma simultaneously to the primary etchant and this creates a thin passivation layer on the sidewalls to enable deep anisotropic etching [49,50]. After etching, the metal layer (from the lift-off lithographic step) is removed and the sample is ready, e.g. for micromechanical testing. The advantage of the combine lithography and dry etching method for fabricating micron-sized samples is the production of a large number of samples in one batch of etching. This saves time and provides data for statistical analysis. However, optimisation of the individual steps requires a lot of iterations. Also, this method can only be used for selected material systems which can be etched to get freestanding samples. A combination of lithography and cryogenic reactive ion etching is used to fabrication micron-sized free-standing silicon micro cantilevers in Chapter 3.

2.3.3 Focused ion beam milling (FIB)

Originally developed in the semiconductor industry for integrated circuit and photolithographic mask repairs, FIB has become a powerful tool for ultra-precision processing and microfabrication [51,52]. Ion beam used for sample modification is generated from a liquid metal ion source (LMIS) [53] or GFIS [54] by the application of a strong electric field in a vacuum. The ions generated are accelerated towards a target sample and used to create patterns on the sample surface by sputtering events [6]. This process is the most used method for micro fabrication in laboratories for making small samples. However, the ion-sample interaction can lead to undesired artefacts such as redeposition, swelling, ion implantation, swelling depending on the energy of the incoming ion [52]. Therefore, it is necessary to optimize the microscope conditions to avoid undesired reactions. Also, removal of large amount of materials is time consuming using FIB leading to the production of only a few samples without statistical information. A detailed description of the influence of artefacts at the notch on small scale fracture experiments is discussed in Section 2.6.

2.3.4 Femtosecond laser ablation

Ultrafast lasers are currently also used for direct solid material ablation because short pulses (femtosecond or picosecond) deliver energy to the target before thermal diffusion occurs which minimises the formation heat affected zone (HAZ) in the vicinity of the exposed region [55–57]. Thus, this method is able to produce microscale structures at high removal rate compared to the FIB (4 - 6 orders of magnitude higher for Ga⁺ FIB) [56,58–60]. Microstructures can be fabricated in materials which are susceptible to Ga⁺ embrittlement using the femtosecond laser. Non-conducting materials can also easily be patterned using this technique [58]. A major shortcoming in using this technique is the large spot size dictated by the laser optics which limits the precision of patterned shapes. For instance, the laser cannot be used to machine sharp notches, which are required for valid small scale fracture experiments, because the optics limits minimum features to a few microns similar to sample size) [61,62] and other subsurface laser-material interactions introduces damage in the ablated region which could be of the order of the sample's critical dimensions [60,63]. Hence, this method could be best suited for samples where the damage region is small compared to the sample dimensions. In some applications, the high removal rate of the femtosecond laser is combined with the FIB to introduce notches, thereby improving efficiency and statistics of measurements.

2.4 Current methods to measure fracture toughness in single phase materials

Resistance of small volume of materials to crack propagation has been measured with several techniques till today. Some of these techniques require extensive sample fabrication using one of the methods presented in the previous section. Methods for measuring fracture properties of specific phases, grains, thin films, coatings are presented in this section.

2.4.1 Semi-quantitative methods

2.4.1.1 Indentation toughness

Indentation fracture mechanics started many decades ago when hardness testers were used to introduce radial cracks in brittle materials such as ceramics and glasses [64,65]. For most investigation, sharp indenters like Vickers or Knoop diamond pyramids are preferred over hard spheres for fracture measurements because the reduced contact area enables direct observations of fracture process since surface cracks are produced [66,67]. These pyramidal tips introduce a plastically deformed area in the material during loading and pile up of material displaced under the indenter creates a tensile stress field below the indenter tip [67]. At critical loads, tensile stresses present at the elastic-plastic interface interacts with existing or indentation-induced flaws causing the formation of a median / radial crack beneath the indenter [65,68,69]. As the indenter is retracted from the material, the media crack attempts to close but is prevented by deformed material in its vicinity and residual tensile stresses induced by elastic-plastic mismatch in the contact zone. This leads to the formation of lateral cracks from the plastic zone which propagate towards the surface during unloading [64,65,67,70].

At small length scales, the same principle is use to create cracks in thin films using nanoindenters [71]. It was however discovered that cracking threshold for introducing radial cracks in brittle materials at small length scales is higher than what is obtainable using the three-sided Berkovich indenter. This challenge is surpassed by using the much sharper cube corner tip which displaces more material in the contact area thereby providing the stresses needed for crack initiation and propagation [71,72]. Then the indentation fracture toughness (K_C) can be calculated using the formulation for half penny cracks corrected for indenter half angle (Eqn. 2.7) [73],

$$K_C = \frac{0.0352}{(1 - \nu)} (\cot \psi)^{2/3} \left(\frac{E}{H}\right)^{1/2} \frac{P_{max}}{C^{3/2}} \quad (2.7)$$

where ν is the Poisson's ratio, ψ is the indenter half angle, E is elastic modulus, H is the hardness, P_{max} is the maximum indentation load and c is the radial crack length measured from the center of the indent.

The availability of indentation-based testing technique made site specific fracture experiments possible for small volumes at relative ease, since little sample preparation is required. Ease and quick sample preparation and measurements make it possible for high throughput investigations in a short period. On the other hand, fracture toughness measured from this technique is often not considered as a material property because of complexities arising from testing setup. For instance, the influence from substrate could occur due to the large contact area required to create conditions

(plastic zone development) for crack nucleation under the indenter [74]. Furthermore, residual stresses arising from growth stresses and thermal mismatch in thin films and coatings on a substrate can alter fracture behaviour, for example overestimation of fracture toughness occurs when compressive residual stresses are present [75,76]. Crack type and size is usually dependent on indenter geometry leading to huge scatter in experimental data [77,78]. Finally, a starting crack length which is needed for fracture mechanics studies is absent in indentation toughness measurements. Hence, this method can only be regarded as a semi-quantitative method for calculating critical stress intensity factor for materials.

2.4.2 Quantitative methods at the micron scale

Availability of sample fabrication techniques described in section 2.3 in the microelectronic industry made quantitative laboratory analysis of small volume of materials possible using micro cantilevers, micro tensile samples and other microelements [79–81]. Since there was no standardised geometry for small scale fracture testing, geometries were developed based on micro structures used for MEMS testing.

2.4.2.1 Single Cantilever beam

Nearly two decades ago the first micro fracture experiment established following fracture mechanics guidelines. Notched pentagonal freestanding micro cantilever beams were fabricated in silicon using FIB and tested using a nanoindenter [82]. In this geometry, a single cantilever is prepared in a specific site of a test sample, a notch is introduced perpendicular to the top surface of the cantilever at some distance from the fixed end, and a load is introduced using a nanoindenter to cause fracture. Following the success of the first work, a much simpler rectangular cantilever beam was proposed and utilised by Matoy [83] (Figure 2.3).

Today, the single cantilever geometry is frequently used for many micro fracture experiments because of ease of fabrication of samples using existing technologies. Samples can either be milled from bulk materials using pentagonal and triangular beams [32,84,85] or at the edges of sample for fracture analysis of thin films / coatings [75,86–88], specific grains [32,89] and phases [90–92]. Also, testing can also be done *in situ* in a scanning electron microscope (SEM) for precise position of the indenter and direct observation of fracture process. In thin films, this geometry eliminates substrate and residual stress influences on fracture toughness. However, the single cantilever beam is prone to unstable crack growth, which is a major concern for fracture testing of brittle materials. In such cases, the fracture experiment yields only a single toughness value, measured at a FIB notch. The fracture toughness is then calculated using the maximum load at fracture (Eqn. 2.8) and a geometry correction factor calculated from FEM for rectangular beams [83],

$$K_I = \frac{P_{max}L}{BW^{3/2}} f\left(\frac{a}{W}\right), \quad (2.8)$$

$$f\left(\frac{a}{W}\right) = 1.46 + 24.36\left(\frac{a}{W}\right) - 47.21\left(\frac{a}{W}\right)^2 + 75.18\left(\frac{a}{W}\right)^3$$

where P_{max} is the maximum fracture load, L is the loading arm (distance from the notch to the indenter), B is width of the beam, W is the thickness of the beam, and $f(a/W)$ is factor dependent on the geometry.

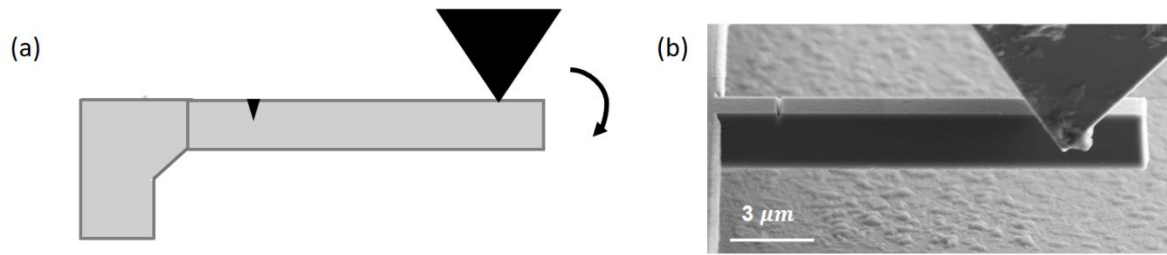


Figure 2.3:(a) Schematic representation and (b) SEM image single cantilever beam fabricated by combination of lithography and FIB.

2.4.2.2 Clamped beam

Another geometry which has been used for fracture testing in the small scale fracture community is the clamped beam which is a scaled down version of three-point bending macro testing geometries (Figure 2.4). In this test geometry, the cantilever beam is clamped at both ends and an edge notch is milled at the bottom center to serve as a starter crack. Then a blunt wedge indenter is placed at the center of the beam for fracture [93,94]. Since no analytical formulation exists for calculating the fracture toughness from this geometry, FEM models based on experimental geometry is used to calculate the stress intensity factor for every test. Studies have shown that the clamped beam geometry offers crack arrest in brittle materials because the location of the maximum tensile stress moves from the notch tip to the fixed ends of the cantilever at critical values of a/W depending on the cantilever length [93,95]. However, cracking at the fixed ends renders an experiment invalid for analysis. Therefore, an optimum notch dimension has to be chosen to delay cracking at the fixed edges while crack arrest is promoted at the main notch [95]. Even with crack arrest and stable crack growth the clamped beam geometry is not suitable for every analysis because residual stresses are present since the beam is still attached to the bulk [33]. Also, notches can only be milled from the side limits fabrication of this geometry to sample edges. Overestimation of fracture toughness can also arise from bluntness and asymmetry the edge milled notches [33].

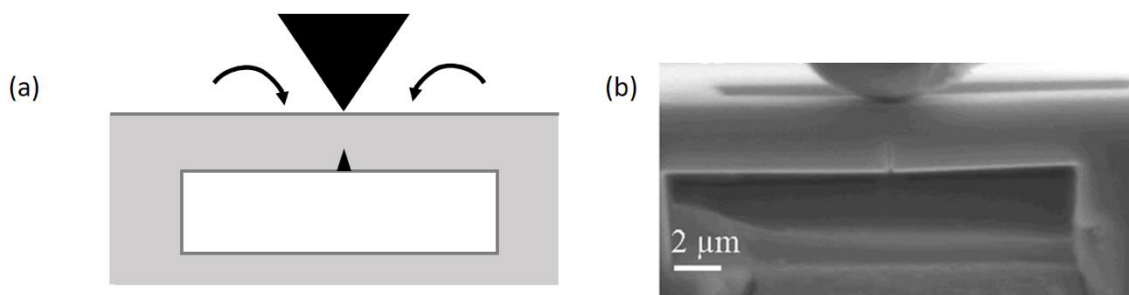


Figure 2.4: (a) Schematic representation of a clamped beam cantilever showing the bending direction and (b) SEM image of same cantilever, reprinted from [33].

2.4.2.3 Double cantilever beam (DCB)

This geometry has been used to perform stable crack growth experiments at the bulk scale for displacement-controlled experiments. In this experiments, the crack driving force reduces with increasing crack length because the energy stored in the beams reduces with crack extension [2]. Traditionally, a beam is symmetrically pre-cracked and bending moments are applied to the two arms to drive the crack under mode I loading [96]. The same principle has been used for small volumes where a notch is placed in the trough of a rectangular pillar and compression or wedging of the two arms drives a crackdown the central axis of the beam (Figure 2.5) [33,97–99]. DCB samples can be milled in the bulk unlike the clamped beam geometry. In the compression version of this geometry, a flat punch is used to apply load that translates to moment on each beam arm leading to tensile loading on the crack plane [98]. However, plasticity at the beam arm could prevent fracture when critical beam dimensions are not adhered to during sample fabrication. This is not a problem when a wedge is placed in the central axis of the beam to drive open a crack, but friction between the wedge and the side walls of the cantilever requires additional analysis. Due to frictional effects, load drops may be absent from load-displacement curves. Thus, the maximum load is determined using lateral displacement values measured via digital image correlation [98]. Misalignment is an issue that cuts across both modifications of DCB testing at small scales. Positioning the wedge tip at the sample's central axis is a major source of misalignment causing asymmetric displacement of the beams during testing which is not the case with the flat punch [33,97]. Also, misalignments between the tip's displacement axis and the sample's surface will cause both beams to be loaded at different wedge angles which would affect the crack driving force. Simultaneous contact of both beams is required when testing DCB with the compression approach. Otherwise, there would be asymmetry in the bending moment in the sample which would create mixed mode loading at the crack tip. Fracture toughness in this geometry is calculated from the strain energy release rate G stored in the loading arms of the beam during crack growth. Liu et al [98] proposed Eqn. 2.9 for calculating K_I from G with a correction made for friction between the flat punch and the sample surface,

$$K_I = \sqrt{3} \frac{(e - \mu h)}{bd^{3/2}} P_c \quad (2.9)$$

where e is the distance between the load point and the neutral axis of the beam, μ is the coefficient of friction, h is the distance from the top of the beam to the crack tip, b is the sample thickness in the direction parallel to the crack plane, d is the beam width, and P_c is the maximum fracture load.

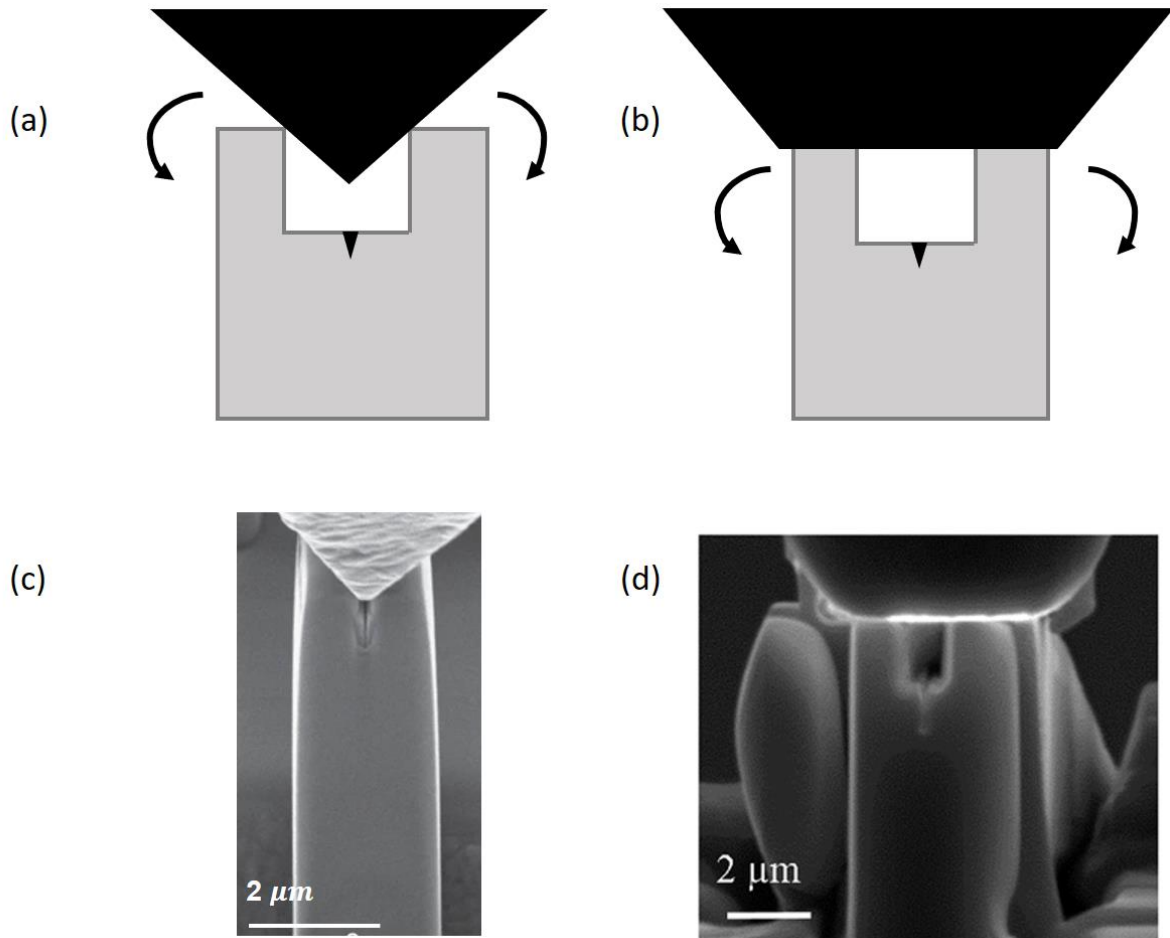


Figure 2.5: Schematic representation of a DCB showing bending direction for (a) wedge tip, (b) flat punch, while SEM images of the two variations of the DCB specimen during testing is shown in (c) and (d), reprinted from [97] and [33].

2.4.2.4 Pillar splitting

Sebastiani et al. [100] proposed splitting a FIB-milled micro pillar using a sharp indenter for measuring fracture resistance of brittle materials (Figure 2.6). A requirement for validity of measurements made using this technique is propagation of radial cracks from beneath the indenter to the edge of the pillar and split into three parts. Similar to indentation toughness measurement, this technique is simple to set up and it improves on the drawbacks of the indentation method. For instance, the *post mortem* measurement of the crack length is not required because fracture toughness is calculated with a simple relation involving the fracture load (P_c), pillar radius (R) and a coefficient relating elastic and plastic properties of the material (γ) (Eqn 2.10). Also, residual stresses at the top of the pillars is minimal at critical pillar aspect ratio of 1.0, thus, does not influence fracture toughness measurement [74,101,102]. Substrate effects do not affect the results measured because pillar splitting occur at shallow indentation depths [74,100]. Since no notch is introduced to this geometry, it is difficult to differentiate between crack initiation and propagation events. On the other hand, the geometry is only suitable for materials which low limited plasticity where the stress fields under the indenter can promote the nucleation of radial cracks [33]. For every material system, the material property coefficient, γ , needs to be calculated using cohesive

FEM formulations. These formulations have so far been calculated using homogeneous, linear elastic, isotropic materials assumptions. There are currently debates on the validation of fracture toughness data obtained from this geometry in the absence of a notch.

$$K_c = \gamma \frac{P_c}{R^{3/2}} \quad (2.10)$$

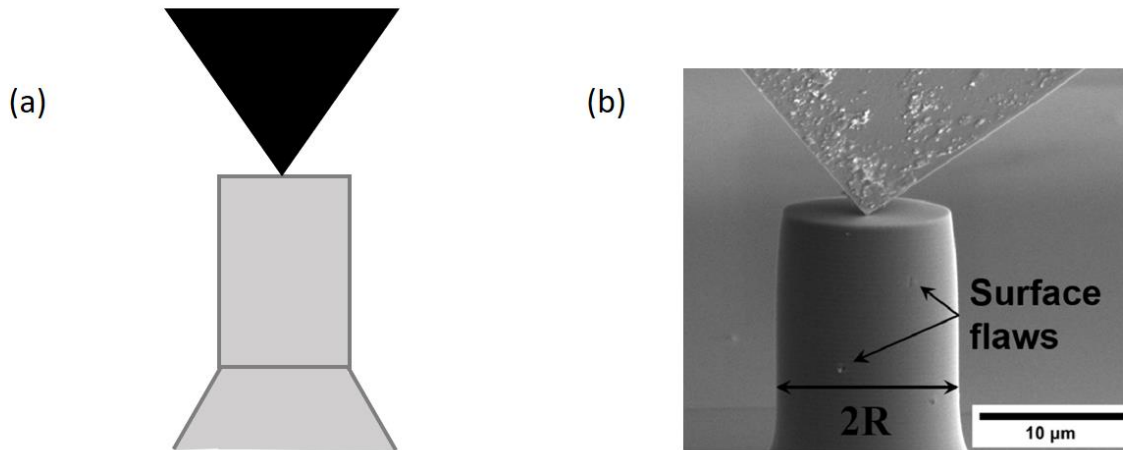


Figure 2.6: (a) Sketch of a pillar with a pyramidal tip and (b) SEM of a pillar at the beginning of an *in situ* test, reprinted from [103].

2.4.3 Notches

Atomically sharp cracks are needed for fracture toughness measurements because they act as stress raisers in the presence of infinitesimal load [1]. Fatigue pre-cracking on machined notches is used to create sharp notches for fracture experiments at the macro scale. Introducing fatigue pre-cracks through cyclic bending or compression is very complicated and has low success rates [85]. Hence, FIB milled notches are used in micro fracture test geometries with the advantage of being accurately placed in a region of interest (crystallographic plane or interface) [27]. Existing strategies to create notches in some of the testing geometries presented in Section 2.4.2 will be discussed below.

2.4.3.1 Through thickness / straight notch

This is the most used notch in many test geometries because it is easy to analyse. It usually entails using a line pattern to create a notch in a region of interest under optimised FIB microscope conditions (Figure 2.7a and b). Although, this notch is versatile and can be used for both brittle and elastic-plastic materials, it is challenging to mill without over-fibbing effects. This effect occurs due to higher milling rates at sample edges which introduces error and a huge scatter to experimental data [7]. Hence, great expertise is required to make through notches with a straight crack front through multiple milling steps.

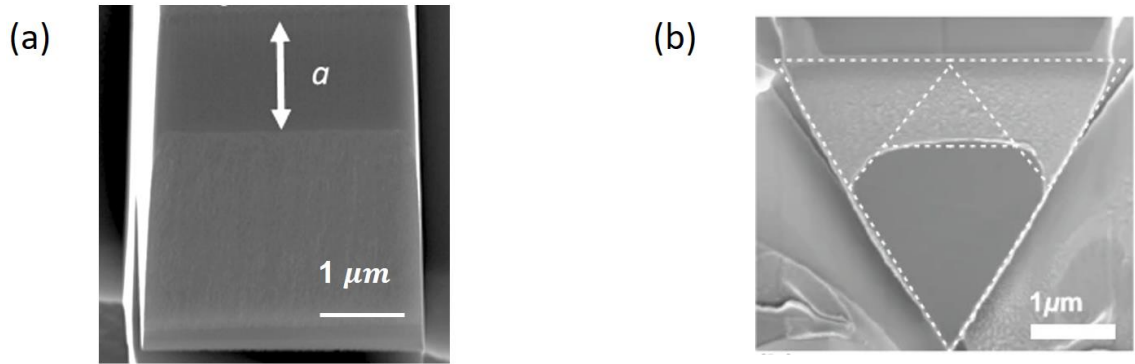


Figure 2.7: (a) *Post mortem* SEM image of a through notch fractured in a rectangular single cantilever beam (reprinted from [75]), and (b) SEM image of a through notch fractured in a pentagonal single cantilever beam (reprinted from [85]).

2.4.3.2 Bridge notch

To overcome the issues of over-fibbing in the through notch, Matoy and his co-investigators [83] proposed the bridge notch geometry using through notches with material bridges at the edges of the cantilevers (Figure 2.8). On loading, the material bridges experience a higher stress intensity factor than the notch front under certain geometrical requirements, and will fracture first to create a crack which grows towards the FIB milled notch front before final fracture. This notch type is easier to mill compared to the notch without bridges and has less experimental scatter in the results. Overestimation of fracture toughness can be an issue using this notch when notch and bridge geometry are not optimized to ensure the bridges fail before final fracture [7]. Also, testing in displacement controlled systems is encouraged for using bridge notches because catastrophic failure of the cantilever does not succeed bridge failure, thereby allowing the creation of a natural crack [7,104].

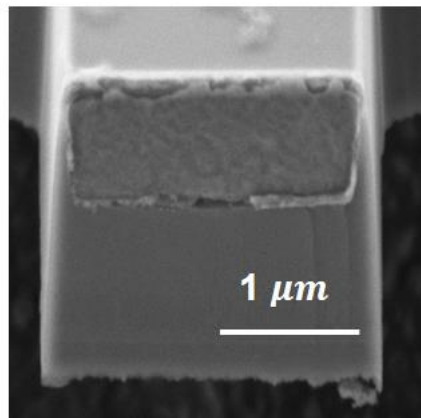


Figure 2.8: *Post mortem* SEM image of bridge notched silicon microcantilever.

2.4.3.3 Chevron / bowtie notch

Notches shaped as a triangular ligament with notch width varying with sample thickness are used for fracture toughness of brittle materials because they eliminate the need for fatigue pre-cracking. The apex of the notch serves as a point for stress concentration for crack initiation at low loads. After a crack is initiated, it grows in a stable manner with increasing load until it becomes unstable at a critical crack length dependent on sample and notch geometry [105–107]. Stable crack growth capability of the chevron notch has also been utilised in different micro fracture geometries for materials showing limited plasticity (Figure 2.9) [32,84,85,108–110]. Many research groups shy away from using this notch despite the stable crack advantage because of the complicated crack analysis. Also, notch asymmetry (Figure 2.9a) resulting from milling errors can lead to mixed mode fracture toughness.

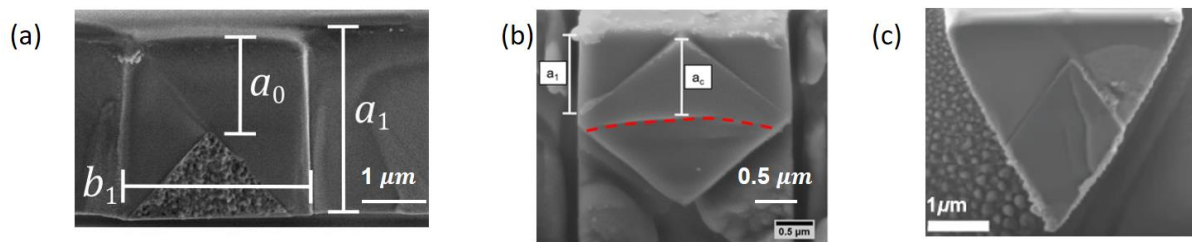


Figure 2.9: *Post mortem* SEM image of samples with chevron notches in (a) rectangular, (b) pentagonal and (c) triangular single cantilever beams, reprinted from [108], [110], [85], respectively.

2.5 Current methods to measure fracture toughness in interfaces and multi-layered materials

In some cases, single phase materials are combined in material stacks to give rise to functionality in specific applications. Functional interfaces in these material stacks find application across different fields including aerospace application, energy storage and conversion systems, and semiconductor devices [111–113]. Functionality is usually accompanied with local property mismatch in the vicinity of interfaces owing to dissimilar materials at adjoining sides of the interface leading to regions of stress concentrations and crack nucleation at the interface [114–116]. This intrinsic driving force for failure and other environmental factors lead to loss of mechanical and functional performance in these material systems [117–119]. Hence, there is a need to also study the strength of interfaces that exist in small volumes.

2.5.1 Semi-qualitative methods

Some methods which have been used to measure interface strength by considering adhesion energies are summarized below.

2.5.1.1 Peel test

Originally called tape test, a peel test (Figure 2.10) is performed to analyse the adhesion of coatings or films to substrates by attaching an adhesive tape to a film or a coating and pulling off the tape at angles between 0° and 180° to observed possible delamination [120,121]. The peel strength

which represents the adhesion energy is calculated by dividing the debonding force by the width of the adhesive tape for tests done at 90° peel angle [122]. Simplicity, minimal cost, ease of measurement, and suitability for both hard and soft substrates have made the peel test a method of choice for adhesion property measurement in the microelectronic industry [121,123,124]. The use of this method is however limited to thick, tough and flexible films with poor adhesion [123,124].

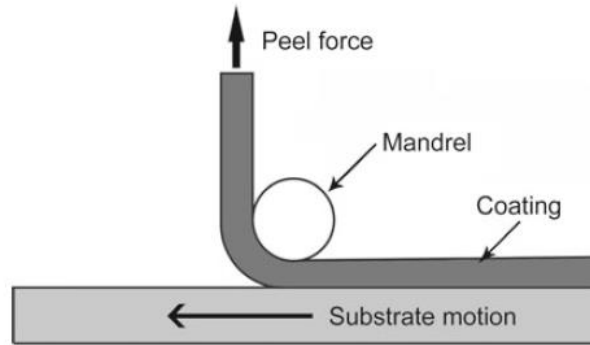


Figure 2.10: Schematic representation of a peel test set up, reprinted from [124].

2.5.1.2 Scratch test

Another simple method to check the interface adhesion of coatings is the scratch test (Figure 2.11). In this test, a spherical tip is drawn across the surface of a coating / substrate sample under a continuous or stepwise load to cause delamination either by buckling (thin films) or wedge spallation (thick films)[125,126]. The critical load which causes failure is used as a measure of the interface adhesion. Although this test is straightforward to set up and requires no extensive specimen preparation, the critical load is heavily influenced by external factors related to the testing conditions such as scratching speed, loading rate, indenter tip radius and indenter wear [127]. From the coating-substrate end, scratch test is influenced by substrate behaviour relative to film, coating thickness, friction coefficient, and residual stresses in coatings [124]. Also, the stress state around the indenter scratching the sample is complex and isolating the stresses which led to delamination is challenging. Hence, this method is best suited for qualitative analysis of coatings [126].

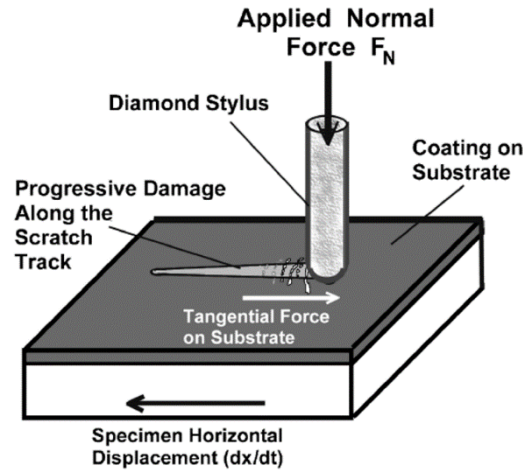


Figure 2.11: Schematic of scratch test, reprinted from [128].

2.5.1.3 Stressed overlayer / Superlayer test

Interface adhesion of ductile films using an overlayer to increase overall thickness and residual stresses was developed by Bagchi et al. [129]. Delamination is induced by the presence of tensile stresses introduced by the deposition of a thick film (overlayer) on a film already lying on a substrate [129,130]. This external thick film has to be unreactive with the existing film on which it has to be deposited, it has to have large intrinsic stresses and deposition has to be at ambient temperatures. Despite its potential to accurately calculate adhesion energy using stress analysis, using this method requires extensive work to achieve film thickness that would induce sufficient residual stresses to drive delamination. Additionally, delamination is only possible if the interface between the film and the overlayer is stronger than the film / substrate interface [123,130].

2.5.1.4 Indentation

Using a nanoindenter, delamination can also be induced in brittle films when lateral cracks (see section 2.4.1.1) generated under the contact region which propagates along the interface [131]. When this crack propagating along the interface reaches a critical length depending on indentation depth buckling of the film occurs at both sides of the indenter. On removal of the constraint by the tip on the film, a single buckle is formed. The indentation stress and / or buckling stress can be used to calculate the strain energy release rate as a measure of interface adhesion [131]. Delamination stages in a hard coating is presented in Figure 2.12

In thinner films, through thickness film cracking precedes delamination due to high bending stresses introduced during nanoindentation thereby dissipating the energy available in the system [132]. Hence, nucleation of new cracks is required for interface delamination which would increase the overall adhesion energy calculated from the tests [132]. For ductile strongly bonded films, delamination is difficult because plastic deformation is dominant during indentation. In such cases, stressed overlayer (section 2.5.1.3) is used to increase the overall thickness and residual stresses of the film to induce delamination [133,134].

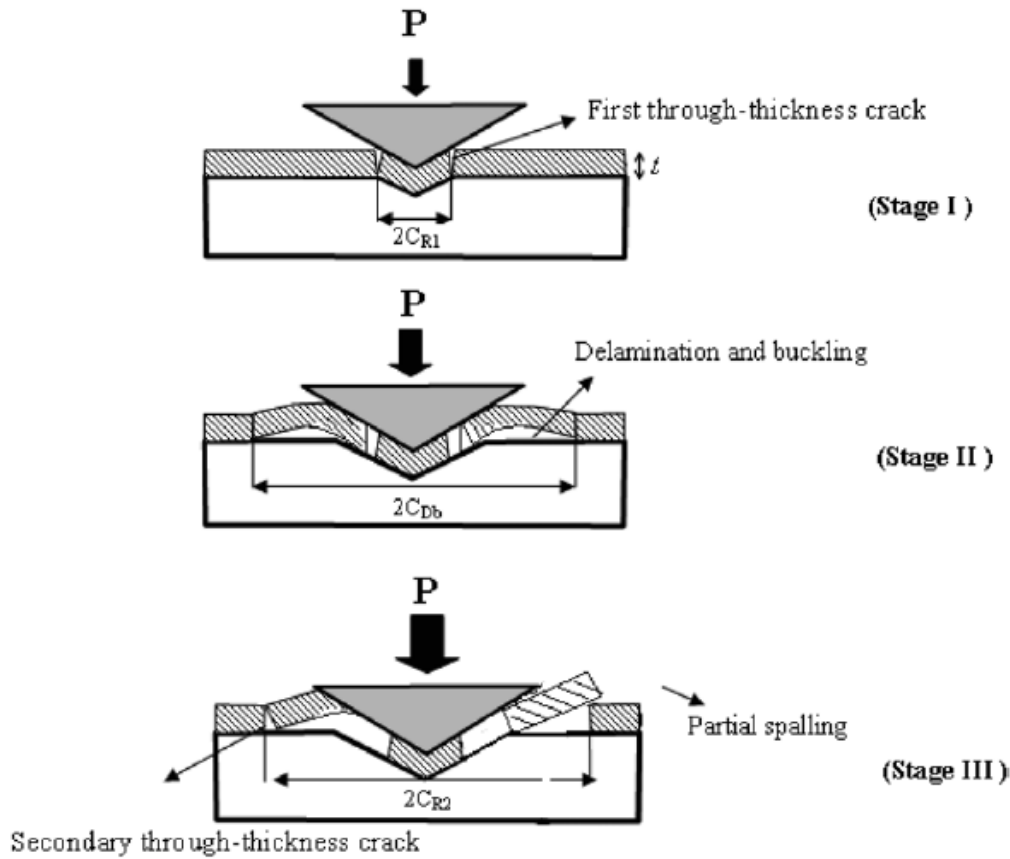


Figure 2.12: Schematic of the delamination evolution in a brittle coating on a hard substrate scratch test, reprinted from [123].

2.5.2 Quantitative methods

Currently, fracture mechanics-based investigations of interfaces in film-substrate system makes use of geometries and set ups already existing for single phase systems discussed in section 2.4.2. One of the first recorded use of existing quantitative geometries for isolating interface properties at the micron scale was by Matoy and co-workers (Figure 2.13a and b) [135]. In their study, a single cantilever beam was used to calculate the fracture toughness of interfaces in a multi-layered system. Subsequently, several groups [136–140] have used the same geometry for fracture tests of interfaces by placing a FIB notch on the interface plane. Figure 2.13c–e shows SEM images of interface fracture inside a TEM using a single cantilever beam. Positioning a notch on the interface plane is difficult in the clamped beam like geometry, since notches can only be milled from the side. Similarly, positioning of the notch on the interface is also problematic in the DCB specimen, because of the relative complicated fabrication process. Sernicola et al. [97] was able to use the DCB to test diffusion bonded SiC single crystals but the application of this geometry to other interfaces still needs to be proven.

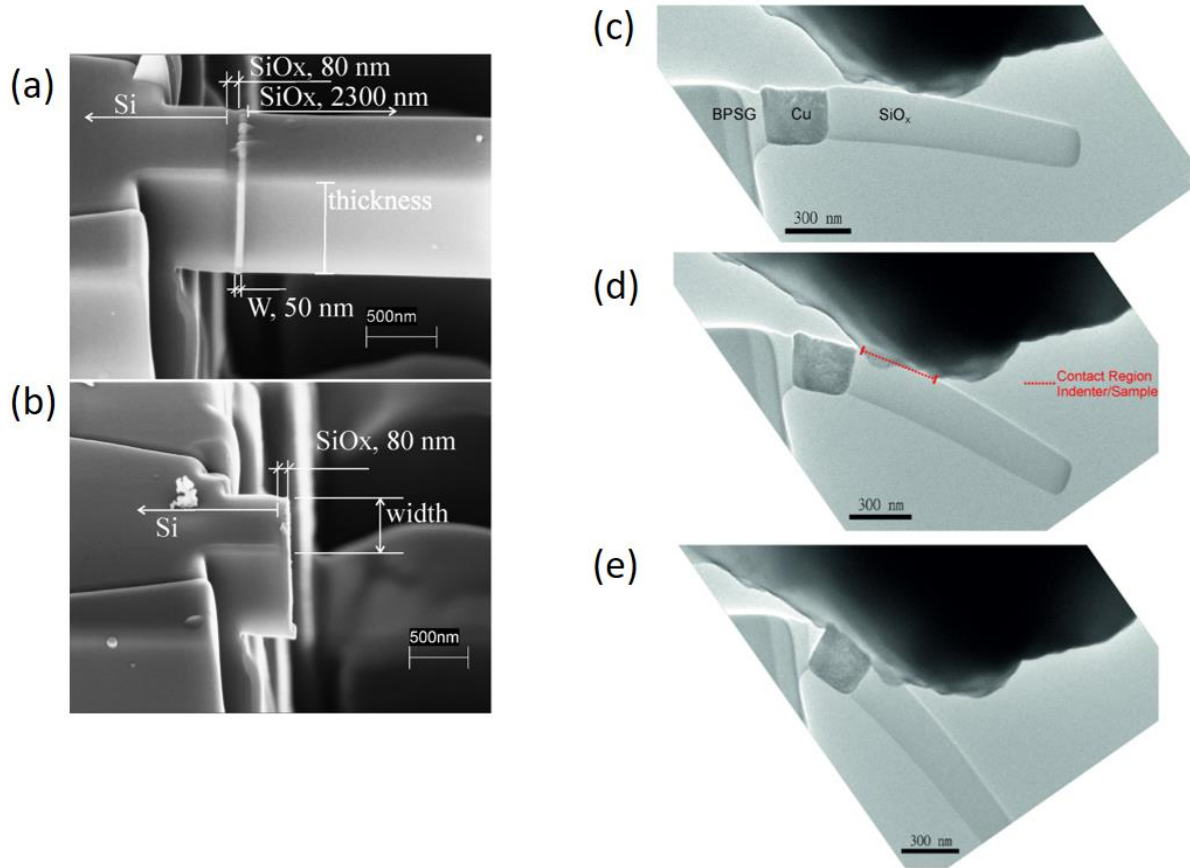


Figure 2.13: (a) and (b) SEM image of single cantilever beam containing an interface before and after fracture test (reprinted from [135]), and (c), (d) and (e) Transmission electron microscope (TEM) image showing stages of interface fracture (reprinted from [137]).

2.6 Artefacts in FIB-based small scale fracture testing

As discussed in section 2.3.3, the FIB offers good precision for making nanometer to micrometre sized samples, but ion-sample interactions pose a challenge. Since starter notches (2.4.3) of a few nanometres are needed for micro fracture experiments, the role of artefacts introduced by the FIB is reviewed in this section.

2.6.1 Artefacts at notch

2.6.1.1 Notch radius

Sharp notches are a primary requirement for fracture experiments, however the spot size and beam tails of the FIB system limits the size of notch radius achievable. It is well known that a large notch root radius leads to apparent increases in fracture toughness due to change in stress field at the notch [141–143]. Geometric effects of the FIB milled notch on fracture toughness have received conflicting reports thus far. One group showed no evidence of notch radius [33,89,144], while the blunt notches increased fracture toughness in other reports [32,145].

2.6.1.2 Residual stresses due ion implantation

When accelerated ions used for microfabrication travel into a target, sputtering occurs in a series of events, after which the incident ion comes to rest after losing all its energy [6,146]. These ions trapped in the target material causes local damage in the exposed area which introduces strains to the lattice [147]. In notches milled with high energetic ions, strains at the milled area can introduce compressive stresses at the notch root [147,148]. Increase in fracture toughness due to implantation induced residual stresses from Ga⁺ have been reported in some micro fracture studies [8,32]. In sapphire the fracture toughness increased by factor of 2 in the presence of stresses between 12–15 GPa at the notch [32].

2.6.1.3 Crystalline defects

Point defects, dislocation loops, and precipitates formed in ion-bombarded area due to atomic displacement of target atoms by incident ions leads to knock-on damage [149–151]. The presence of such defects at notch can also lead to embrittlement at the crack tip. Preiß et al. [152] observed local brittle like fracture processes round a Ga⁺ milled notch, but as crack moved away from notch ductile processes were more prevalent.

2.6.1.4 Redeposition

Sputtered atoms which are not evacuated into vacuum during milling attach to the target's surface forming a layer of new material on milled surfaces [153–155]. This new redeposited material has a been reported to have significant gallium concentration with a different crystal structure from the target material [156–159]. Such changes in local composition of material at the notch would lead to false measurements which in not reflective of true fracture toughness.

2.6.1.5 Chemical interaction and segregation

Embrittlement caused by chemical interaction of gallium with some metals is also one outcome of FIB milling [148,160–162]. Segregation of gallium to grain boundaries changes the fracture behaviour of materials; and failure is by intergranular decohesion of grain boundaries [163,164]. Change of fracture behaviour attributed to gallium diffusion was reported in CrN micro cantilevers during high temperature fracture testing [145].

One or more of these artefacts may be present in a FIB notched sample and may interact depending on the target material, and the milling conditions (acceleration voltage of ions, and exposure time).

3.0 Optimisation of bridge notch geometry in single cantilever beams: an approach for minimising FIB artefacts

Chapter 3 is intended to be submitted as a journal publication.

The subsequent researchers have contributed to the experiments and their interpretations. A detailed description of the individual contributions can be found in the appendix.

E. Okotete¹, S. Brinckmann², S. Lee¹, C. Kirchlechner¹.

¹Institute for Applied Materials, Mechanics of Materials and Interfaces, Karlsruhe Institute of Technology

²Institute for Energy and Climate Research, Forschungszentrum Jülich, 52425 Jülich

3.1 Introduction

The single cantilever beam geometry is the most popular geometry for measuring fracture toughness at small length scale, see details in Chapter 2, Section 2.2.1. However, the single cantilever geometry is inherently prone to unstable crack growth. Hence, artefacts from sample fabrication procedure might influence the test results. Specifically, the quality of FIB-milled FIB notches affect the reliability of fracture measurements obtained using the single cantilever geometry.

In small scale fracture, bridge notches were first introduced to curb experimental imperfections such as over-fibbing associated with creating through thickness notches on single cantilever bending beams [83]. This was proposed under an assumption that the bridges experience high stress intensities and fail ahead of the FIB-milled notch [7]. These notches are prepared by milling a line perpendicular to the free surface of the cantilever leaving material bridges on both ends of the cantilever (see Figure 3.2). After the introduction of the bridge notch, FEM calculations were made by Brinckmann et al. [7] to evaluate the stress intensity at the bridge in comparison to a through thickness notch. This work provided guidelines for bridge geometries which will fail ahead of FIB-milled notches. However, direct observation of bridge failure was not reported in the small scale fracture community until the recent work of Zhang et al. [104]. This work was able to clearly experimentally observe failure of thin material bridges, and crack arrest ahead of final unstable fracture in micro cantilevers made from CrN/AlN multi-layers and CrN hard coatings. Crack arrest during the bend test of a single cantilever beam helped to interrupt the unstable crack growth expected in such geometries. This implies that a natural crack is grown from the failed bridges which is independent of the FIB-milled notch. This new natural crack front has less FIB artefacts compared to the originally milled notch.

In the work of Zhang et al. [104], crack arrest was observed in experiments conducted on cantilevers with fixed notch depths and bridge using geometry predicted by simulations. It was expected that failure at a natural crack after crack arrest would result in FIB-independent fracture toughness. The results showed higher fracture toughness at the natural crack compare to the toughness at the top of the bridge. The authors attributed these to several factors including embrittlement of the bridges by Ga^+ . If this argument holds true, then the chemical interaction between Ga^+ and target material would affect the extent of embrittlement. Thus, it would be interesting to investigate if the embrittlement at the bridge assumption holds true for all materials. Also, since the bridge failure was observed in cantilevers with very thin bridges and relatively deep notches, a systematic investigation of the influence of different notch and bridge geometries is still missing. Such investigation will serve as an experimental guide to the use of bridge notches complementary to the simulation work of Brinckmann et al. [7].

With the above in mind, this chapter aims to provide notch and bridge geometries for the optimisation of bridge-notched single cantilever beam. This is necessary to ensure that natural cracks independent of FIB artefacts are created during testing after crack arrest. Single crystalline silicon is chosen as model system, because of its significance in the MEMS industry and the well-established fracture mechanics in the micro fracture community [165,166]. To this effect, hundreds of micro cantilevers produced via the batch processes explained in section 3.2 were used. These cantilevers were notched with different depths and widths within the range where reliable fracture toughness values can be extracted without geometric artefacts influencing the data. Additionally, the bridge geometry was varied for each notch depth to clearly identify the regions where the width of the material bridges affects crack arrest and fracture toughness.

3.2 Experimental procedure

3.2.1 Material

A silicon on insulator wafer (SOI) was used as starting material to make test samples for the investigations in this Chapter. This wafer design has a thin single crystalline silicon device layer deposited on a silicon handle substrate with an insulating buried oxide layer (BOX) lying between the device and the handle. The BOX layer acts as a barrier to isolate the device from the handle thereby preventing processes such as etching from progressing between the silicon layers making it possible to fabricate high-aspect ratio MEMS devices and other similar structures [167,168].

A 100 mm diameter wafer having 3 μm thick silicon device layer deposited on a 525 μm thick silicon substrate separated by a 5 μm BOX layer (Siegert GMBH, Germany) was used for the investigations in this chapter. The device and substrate were in the (110) normal orientation.

3.2.2 Cantilever preparation

Cantilevers were produced via a combination of lithography method and reactive ion etching using facilities at the Karlsruhe nano micro facility (KNMFi). The as-received wafer was first spin coated with polymethyl methacrylate (PMMA) (Labspin6, Süss MicroTec SE, Germany) electron beam resist to protect the surface of the wafer from contamination during the subsequent cutting process. Then the wafer was cut into 20×20 mm chips, and each chip was marked by a parallel line on the backside to identify the in-plane crystallographic orientation of the chip for subsequent steps.

3.2.2.1 Electron beam lithography

The chip (hereafter referred to as sample) was ultrasonically cleaned using acetone for 10 minutes, then rinsed in isopropanol and subsequently dried by nitrogen gas. The sample was then coated with a bi-layer of PMMA in a spin coater (Labspin6, Süss MicroTec SE, Germany). The first layer was spin coated with PMMA AR-P 662.04 at a spin speed of 1000 rpm, acceleration rate of 1000 rpm/s for 60 seconds and baked on a hot plate at 180 °C for 5 minutes to achieve layer thickness of 250 nm. Similarly, the second layer was spin coated with PMMA AR-P 672.04 at a spin speed of 750 rpm, acceleration rate of 1000 rpm/s for 60 seconds and baked on a hot plate at 180 °C for 5 minutes which resulted in a layer thicknesses of 150 nm. Then the pattern for the cantilevers was exposed to the resist layers on the sample by electron beam (EPBG5200Z, Raith GmbH, Germany) equipped with Beamer (GenISys GmbH, Germany) pattern generator system at 100 kV with a dose of 900 $\mu\text{C}/\text{cm}^2$. After exposure, the sample was developed in a 1:1 solution of Methyl isobutyl ketone and Isopropanol (MIBK:IPA) for 45 seconds. Afterward, a 100 nm chromium film is deposited on the sample by electron beam evaporation at 10 rpm and 0 ° tilt angle in a coating chamber (UNIVEX 400, Leybold GmbH, Germany). Finally, the PMMA layers were lifted off by dipping the sample in acetone for 5 minutes in a 50% power ultrasonic bath to form a Chromium hard mask.

3.2.2.2 Deep reactive ion etching (DRIE)

The sample was then transferred to an inductively coupled plasma (ICP) lab system (100 ICP-RIE 380, Oxford instruments) for cryogenic DRIE. The masked sample was cryogenically cooled in the chamber to -95 °C. The etching recipe was first conditioned on a substrate for 10 minutes. Sulphur hexafluoride (SF_6) and oxygen gases were pumped into the chamber at flow rates of 245 sccm and 6 sccm, respectively. Etching was done at a radiofrequency (RF) power of 8 W and ICP power of 80 W at 5 mTorr chamber pressure. Strike steps of 4 seconds was used achieved etching rate of 1 $\mu\text{m}/\text{minute}$ resulting in a total etch time of 3 minutes 30 seconds. After etching the sample was imaged with SEM (Supra 60VP, Zeiss Microscopy GmbH, Germany).

3.2.2.3 Post etching steps

After inspection of the silicon cantilevers, the sample was wet etched to remove the BOX layer using 5 % buffered HF solution for 1 hour and then rinsed in isopropanol. Finally, the chromium mask was also wet etched in TechniEtch Cr01 etchant (ceric ammonium nitrate: Perchloric acid: water = 10.9 %: 4.25 %: 84.85 %) for 2 minutes before rinsing off in ethanol. The array of the cantilevers produced by the steps described above is shown in Figure 3.1.

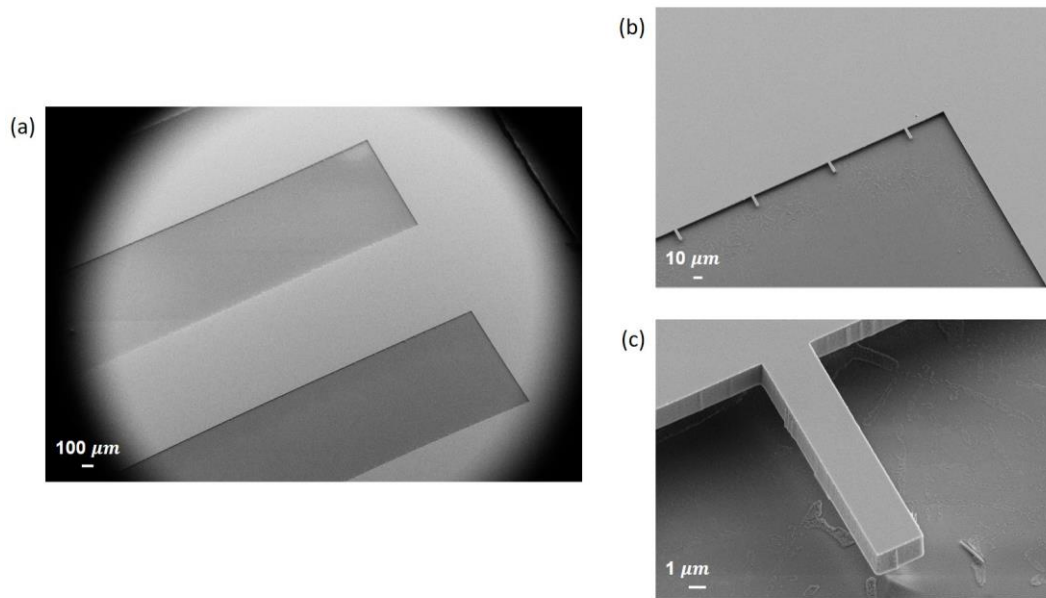


Figure 3.1: (a) SEM image of one sample etched by DRIE (b) cantilevers in one row of etched sample and (c) a single free standing cantilever showing sharp edges.

3.2.3 Notching of cantilevers

The free-standing silicon cantilevers were notched perpendicular to the low energy (111) cleavage plane of silicon. Line elements was utilised to mill bridge notches on the cantilevers using a Ga⁺ FIB (Crossbeam 550L, Zeiss Microscopy GmbH, Germany) at an acceleration voltage of 30 kV with a beam current of 20 pA. The notch depths a/W were varied from 0.20 – 0.45 and bridge factor $l-b/B$ varied from 0.01 – 0.17.

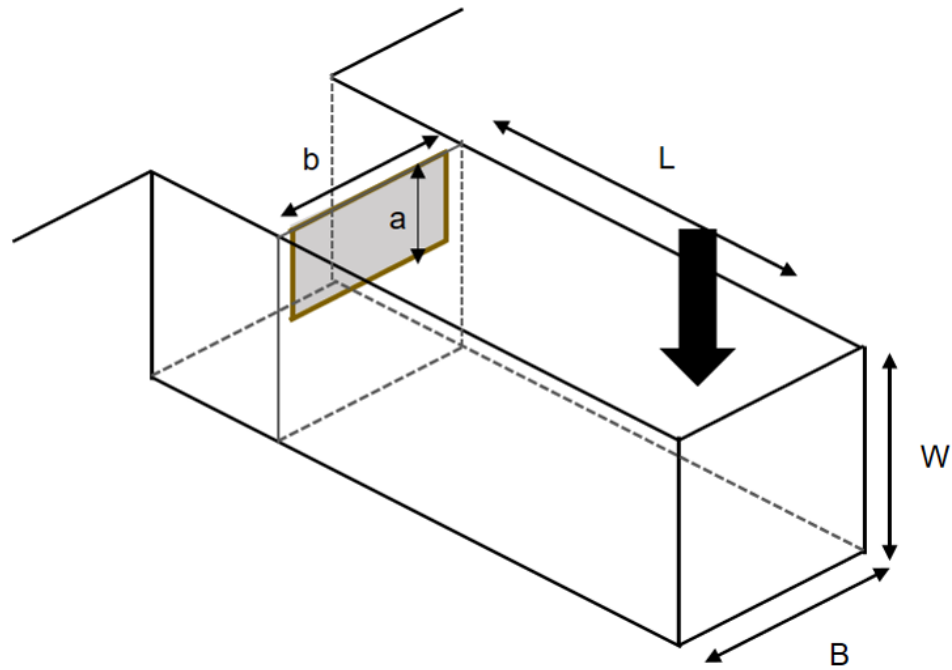


Figure 3.2: Schematic drawing of the cantilever geometry from Figure 3.1c showing the designations of the geometry; W — beam thickness, B — beam width, b — notch width, L — beam length, and a — notch length. The black arrow represents the loading direction and the contact point.

3.2.4 *In situ* SEM deformation testing

Micro cantilever bending experiments were performed *in situ* in an SEM (Merlin, Zeiss AG, Germany) using a PI 89NG indenter (Hysitron, Bruker, USA) which is equipped with an electrically conductive 10 μm wedge tip (Synton-MDP AG, Switzerland). The sample was tilted at an angle of 15 degrees using an in-house pre tilt holder to increase the signal to the secondary electron detector. First, the XYZ stage controller of the SEM was used to align the indenter stage under the electron gun. Thereafter, the indenter tip was moved towards using the Y-stage controller of the indenter and the shadowing technique was used for final alignments of the micro cantilevers and the wedge using the XYZ stage of the indenter. A low load displacement-controlled transducer with maximum load of 10 mN and noise floor of 0.4 μN was used for all the experiments in this chapter because low noise of this transducer enhances the direct observation of bridge failure [104]. Displacement rates of 10 nm/s were used in the bend tests.

3.3 Results

3.3.1 Fracture response via crack arrest

Figure 3.3a shows a load – displacement plot of one of the tested cantilevers where crack arrests precede final fracture. An elastic loading region is observed as expected for brittle single crystalline silicon subjected to constant external loading. There is no noticeable change on the top and side of the cantilever (Figure 3.3b). At point F_{B1} , the first load drop is reached at one end of the cantilever representing bridge I . Figure 3.3c shows a change in the vicinity of bridge I corresponding to the first material bridge failure and crack arrest during the bending test. As the

test continues, another load drop is observed and SEM image (Figure 3.3d shows an extension of the failed region in bridge 1 and the failure at bridge 2 corresponding to F_{B2} . Between points F_{B2} and F_C , the region where the material bridges failed grow towards the FIB-milled notch before final unstable fracture (Figure 3.3c). The final fracture takes place with a new natural crack evolved from the failure and crack arrest of the material bridges. The observation in the silicon cantilevers are comparable to the ones originally reported for CrN/AlN multi-layers and CrN hard coatings by Zhang et al. [104].

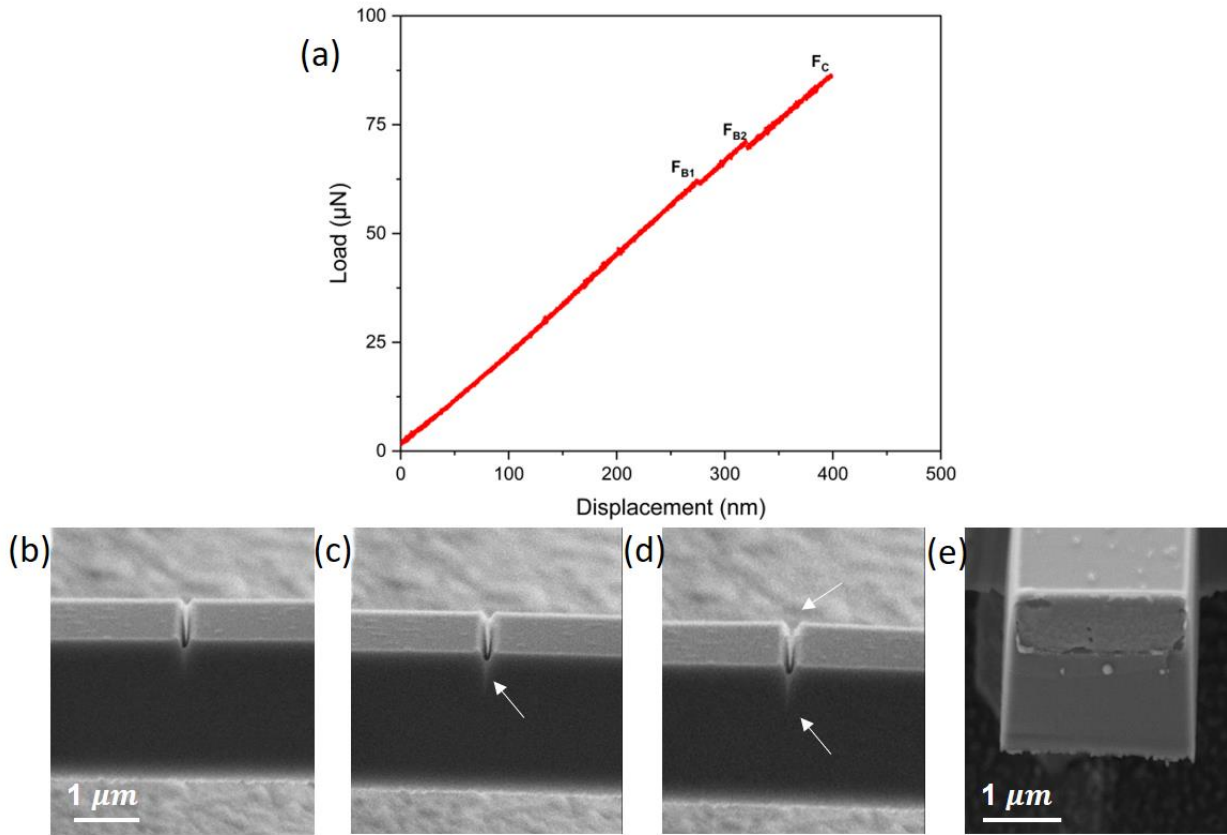


Figure 3.3: (a) Load – displacement plot from experiment, (b) SEM image of cantilever at the start of test, (c) SEM image after failure of bridge 1 at F_{B1} , (d) SEM image showing extension of crack at F_{B1} and failure of bridge 2 at F_{B2} and (e) SEM image of fractured cross section.

3.3.2 Effect of notch and bridge geometry on crack arrest

The fracture toughness (K_{IQ}) for samples which showed crack arrest is calculated from the final fracture load (*point* F_C) using fracture equation modified by [83] (Eqn 3.1) for a through thickness crack. For samples where crack arrest was not observed (no load drops), it is unclear if the final fracture occurred at the bridges or at the notch. Hence, it remains unclear whether or not the fracture toughness ($K_{IQ_corrected}$) (Eqn. 3.2) needs to be modified by a bridge correction factor (f_{corr}) [7]. f_{corr} is a notch and bridge geometry dependent factor calculated using data obtained from FEM simulations, where the stress intensity factor in the absence of a bridge divided by the average stress intensity factor at the top half of the bridge.

$$K_{IQ} = \frac{F_C L}{BW^{3/2}} f_{Matoy} \left(\frac{a}{W} \right) \quad (3.1)$$

$$K_{IQ_corrected} = \frac{K_{IQ}}{f_{corr}} \quad (3.2)$$

where F_C — maximum load at fracture, f_{Matoy} — is a geometry correction factor. K_{IQ} of all cantilevers tested is plotted in Figure 3.4 and 3.5 as a function of bridge geometry, namely the bridge width and depth. The filled circles indicate the samples where bridge failure is observed by load drops, while the open circles did not show load drops prior to final fracture. In Figure 3.4, K_{IQ} is plotted assuming fracture at the through-thickness notch for all samples independent of crack arrest observation (Eqn. 3.1). Note that for filled circles this assumption is justified. In addition, K_{IQ} for samples that did not show crack arrest (opened circles) were corrected before plotting in Figure 3.5. It is seen that bridge notch correction factor reduces the apparent fracture toughness of samples where crack arrest was not observed in the marked region (above the 1.0 line). Below the 1.0 line, the change in apparent toughness is not noticeable from the colour map.

In the lower left corner of the plot in Figure 3.4 where the cantilevers have thin material bridges ($l-b/B < 0.03$) and shallow notches ($a/W < 0.3$), no bridge failure is observed before final fracture (Figure 3.6a). The mean K_{IQ} of the samples in this region is to be $1.0 \pm 0.1 \text{ MPa m}^{0.5}$ comparable to the fracture toughness of single crystalline silicon ($1 \text{ MPa m}^{0.5}$) [169]. Cantilevers in the upper left corner of the plot, in other words, ones with thick bridges and shallow depths ($a/W < 0.3$, $l-b/B < 0.07$) (Figure 3.6b), also did not show bridge failure but a slightly higher average fracture toughness is measured; the average K_{IQ} is $1.2 \pm 0.1 \text{ MPa m}^{0.5}$ at $l-b/B$ between 0.04–0.07, and as the bridge width increases further (> 0.07) it is $1.5 \pm 0.1 \text{ MPa m}^{0.5}$. The apparent fracture toughness increases with bridge width which is linked to stiffer cantilevers as bridges get thicker and eventual fracture at the bridge with no crack arrest. Note that in this case, the geometry factor assuming a through-thickness notch was used, which does not describe the stress intensity at the bridges. The average apparent toughness after correction (Figure 3.5) using f_{corr} is $1.1 \pm 0.1 \text{ MPa m}^{0.5}$, $1.3 \pm 0.1 \text{ MPa m}^{0.5}$ and $1.5 \pm 0.1 \text{ MPa m}^{0.5}$, respectively for the different range of bridge widths stated above.

Since crack arrest was not observed in sample with shallow notches, the notch depth is increased, and the result is seen in the bottom center and bottom right of Figure 3.4. At $a/W > 0.3$, bridge failure is observed in the load-displacement curves. In this area (a/W between 0.3–0.4 and $l-b/B < 0.04$) (Figure 3.6c), average K_{IQ} of the samples which showed bridge failure ahead of final failure is $1.1 \pm 0.1 \text{ MPa m}^{0.5}$ which is also close to the expected values for fracture of single crystalline silicon. Similar to the observation made for shallow notches, increasing the bridge width (Figure 3.6d) does not result in bridge failure, but an increase in apparent fracture toughness. For similar notch depths, K_{IQ} increases to $1.3 \pm 0.3 \text{ MPa m}^{0.5}$ and $1.5 \pm 0.1 \text{ MPa m}^{0.5}$ for $l-b/B$ between 0.04–0.07 and > 0.7 respectively. The corrected values of apparent fracture toughness ($K_{IQ_corrected}$) of samples with the same bridges is $1.5 \pm 0.3 \text{ MPa m}^{0.5}$ and $1.6 \pm 0.1 \text{ MPa m}^{0.5}$. Table 3.1 shows a summary of the average fracture toughness before and after correction calculated for the cantilevers with different bridge and notch geometry.

Table 3.1: Average fracture toughness calculated for tested samples

Notch depth (a/W)	Bridge width (1-b/B)	K_{IQ} (MPa m ^{0.5})	$K_{IQ_corrected}$ (MPa m ^{0.5})	Crack arrest
< 0.3	< 0.03	1.0 ± 0.1	1.1 ± 0.1	No
	0.04–0.07	1.2 ± 0.1	1.3 ± 0.1	No
	> 0.07	1.5 ± 0.1	1.5 ± 0.1	No
0.3 – 0.4	< 0.03	1.1 ± 0.1		Yes
	0.04–0.07	1.3 ± 0.3	1.5 ± 0.3	No
	> 0.07	1.5 ± 0.1	1.6 ± 0.1	No

It can therefore be concluded from the above results that the width of material bridges is crucial to both crack arrest and nucleation of natural crack and getting a geometry independent K_{IQ} . Also, correcting the apparent fracture toughness with the bridge notch correction results in slight increase toughness. On the other hand, increase in the notch depth notch doesn't affect toughness. Therefore, K_{IQ} is only considered K_{IC} (a material property) when crack arrest is observed. All other values should be considered as K_{IQ} (geometry-dependent or, in case of FIB milled specimens even better, system-dependent).

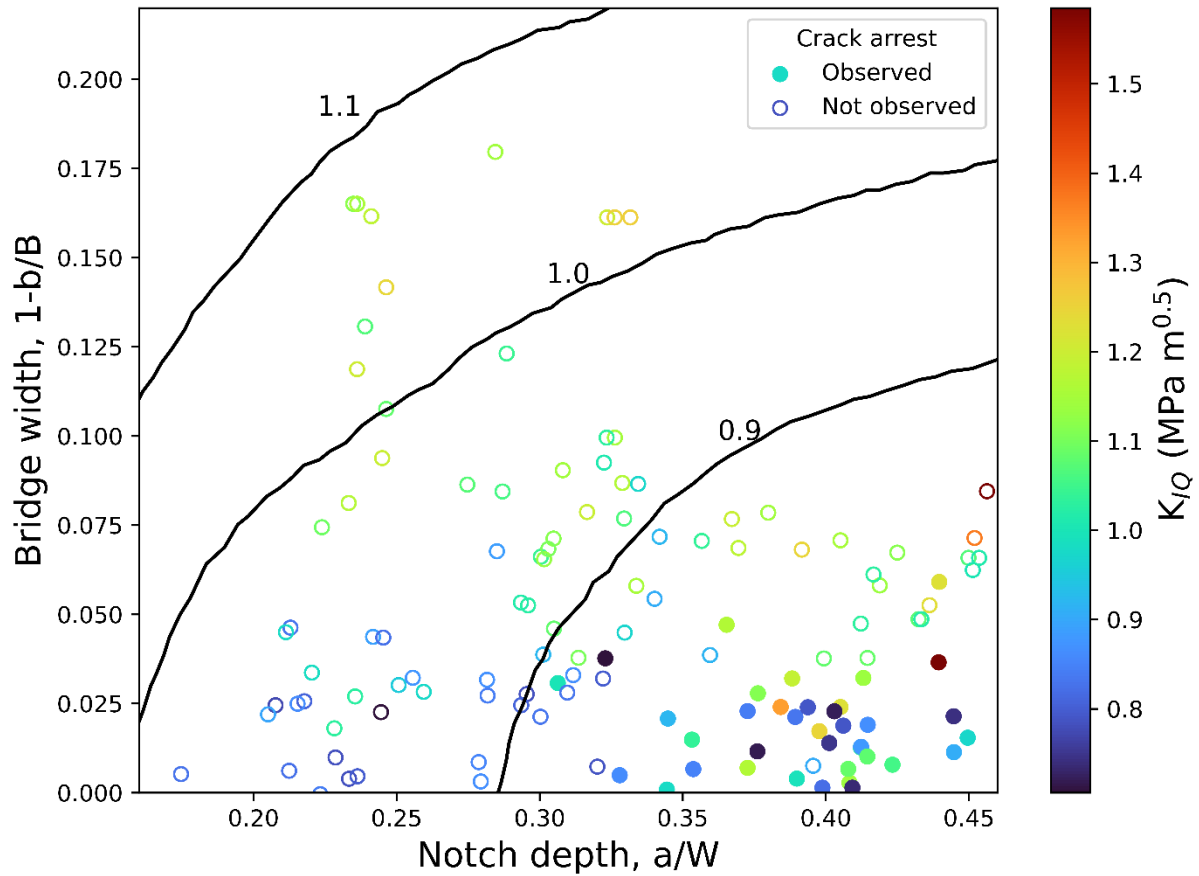


Figure 3.4: K_{IQ} assuming through-thickness notch for samples with different bridge and notch geometries. Filled circles and unfilled circles represent observation and absence of crack arrest, respectively. For filled circles, the assumption of through-thickness notch is fulfilled.

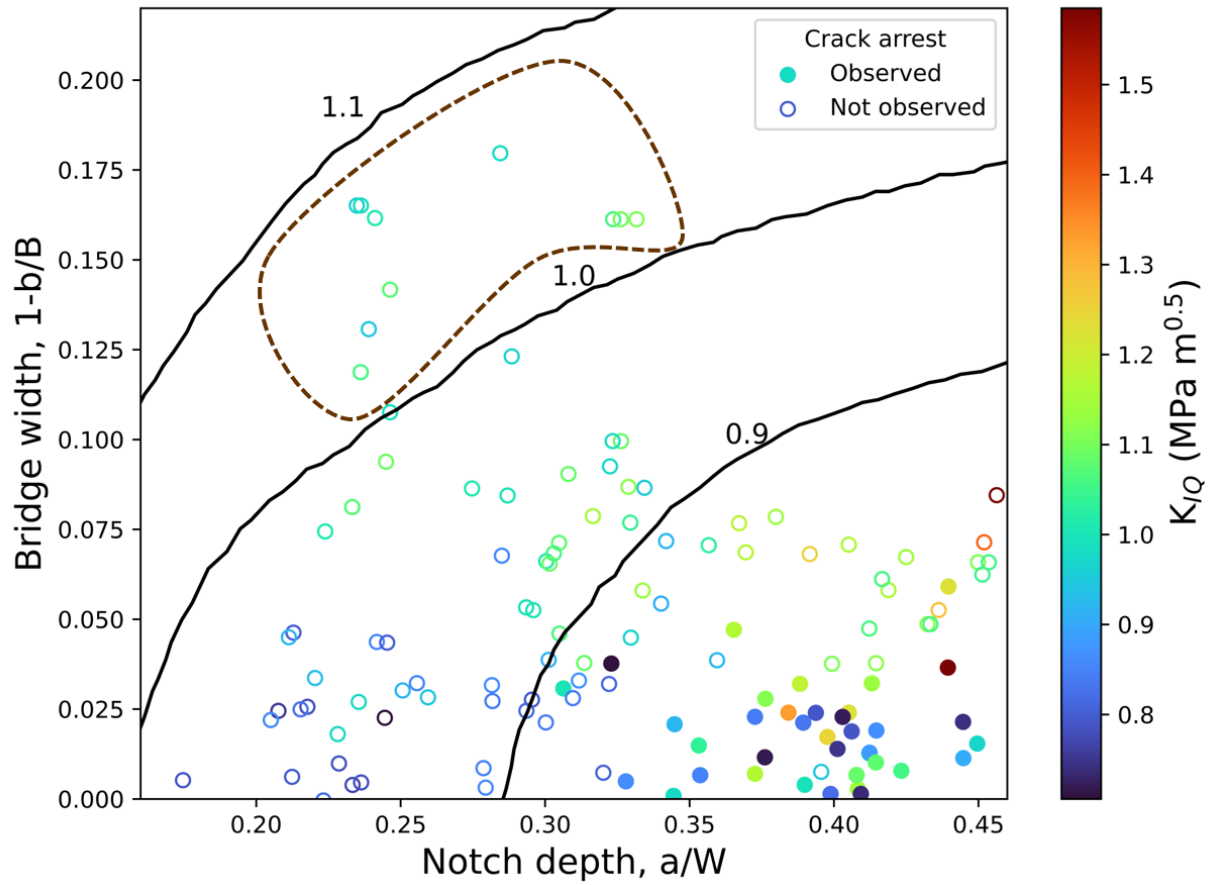


Figure 3.5: Corrected apparent fracture toughness ($K_{IQ_corrected}$) for samples where crack arrest was not observed (unfilled circles), and K_{IQ} for samples where crack arrest was observed (filled circles) where geometry correction was not needed.

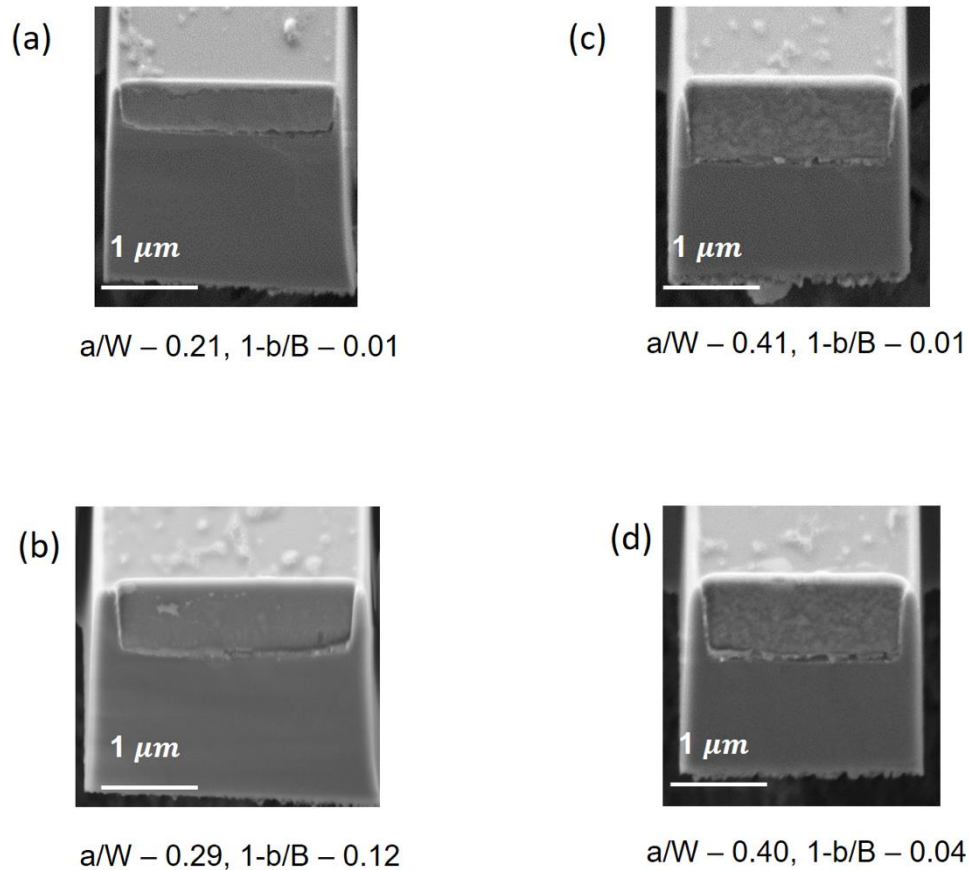


Figure 3.6: (a) shallow notch, thin bridge, (b) shallow notch, thin bridge (c) deep notch, thin bridge and (d) deep notch, thick bridge.

3.3.3 Experiments vs. simulation predictions

To compare the experimental results data to FEM calculations, K_{IQ} values are overlaid on a section of a map extracted from [7] for displacement controlled experiments. f_{corr} of 0.9, 1.0 and 1.1 extracted from the original map are shown in Figure 3.4 Bridge failure is expected at stress intensity ratio less than 1.0 when the stress intensity at the bridges is high than at notch front. It is seen that the experimental data is in agreement with the prediction of FEM calculations from the work of Brinckmann et al., [7] where bridge failure is expected in cantilevers with thin material bridges and deep notches. The superimposed plot also shows that the geometrical condition for failure of material bridges in a displacement controlled experiment is satisfied because the samples where bridge failure was observed fall below the 1.0 stress intensity ratio line (excerpt from [7]). From Figure 3.5, it is seen that the apparent fracture toughness reduces after correction for data points lying above the 1.0 line. Data points lying below the 1.0 line had an increase in apparent fracture toughness. It is also seen that the 0.9 line is closer to the region where crack arrest was observed for the samples investigated than the 1.0 line.

In Figure 3.7, the cumulative distribution function of fracture toughness of fracture at the bridge (K_{IC}^*) and at the notch (K_{IC}) is presented for the samples where load drops were observed. The mean K_{IQ}^* for these samples is $1.0 \pm 0.2 \text{ MPa m}^{0.5}$ and at the notch K_{IC} is $1.1 \pm 0.1 \text{ MPa m}^{0.5}$.

Although the figure does not show a definite trend, it can be inferred that there is no significant difference in fracture toughness from the bridge and at the crack front. To find the relationship between both values of fracture toughness, the cumulative distribution of the ratio of K_{IC} / K_{IC}^* is plotted in Figure 3.8. The mean of this ratio is 1.0 ± 0.1 which suggest an almost equal toughness at the notch and bridge. However, a much larger scatters can be seen in the toughness at the bridges. The sharp notch created as a result of bridge failure has been suggested to be possibly responsible for the low scatter in fracture toughness from the crack front [104].

$$K_{IC}^* = \frac{F_B L}{BW^{3/2}} \frac{1}{f_{corr}} f_{Matoy} \left(\frac{a}{W} \right) \quad (3.3)$$

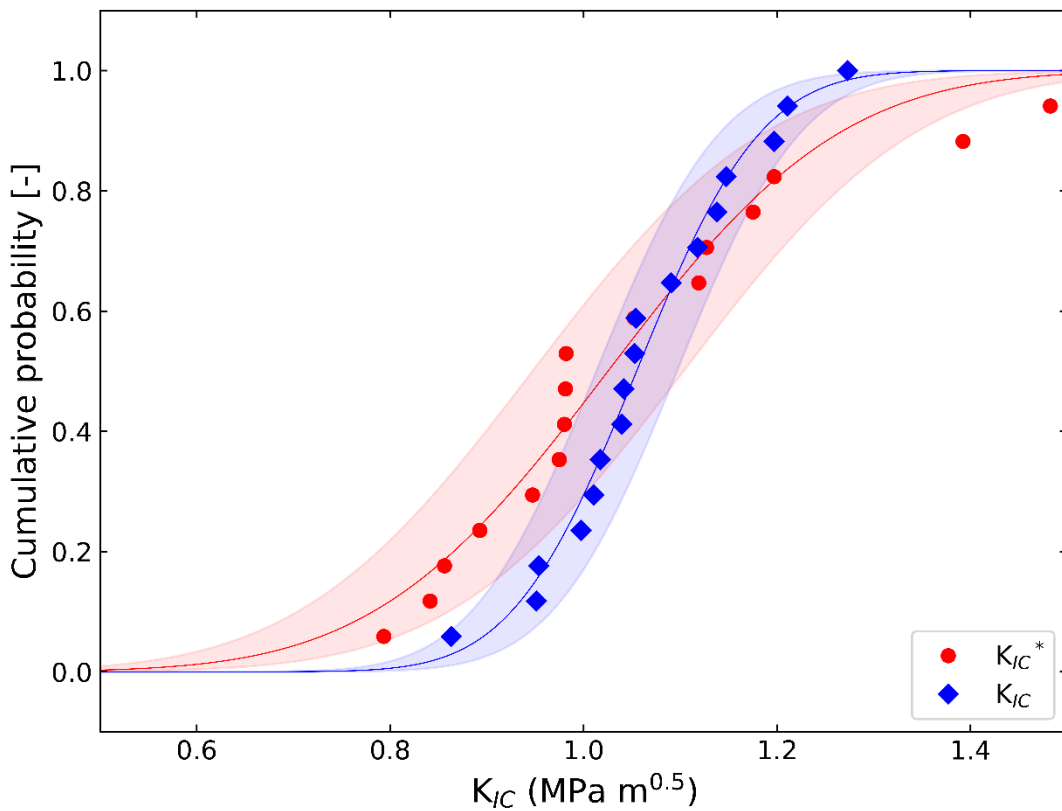


Figure 3.7: Cumulative probability function of the fracture toughness at the bridge (K_{IC}^*) and the notch (K_{IC}).

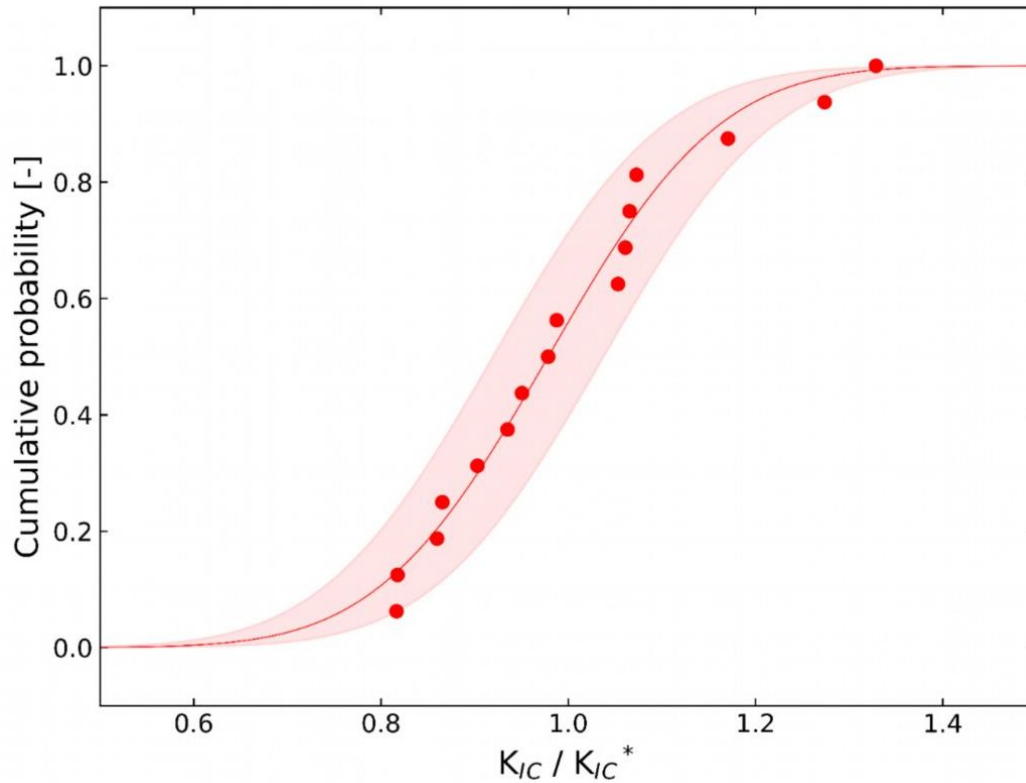


Figure 3.8: Cumulative probability function of the stress intensity ratio.

3.4 Discussion

3.4.1 Crack arrest in single crystalline silicon cantilevers

Unstable crack growth in single cantilever beam experiments have been a concern in micro fracture mechanics community because sample preparation imperfections influence the measurements significantly. A FIB notch used in this geometry is usually heavily affected by ion-material reactions such as chemical interactions, residual stresses, and segregation. Also, it is blunter compared to a natural crack or fatigue crack which are generally believed to be atomically sharp. Therefore, unstable crack growth from a FIB-milled notch may lead to an inaccurate determination of the fracture toughness. One of the approaches to circumvent this very crucial problem is the use of bridge notches to grow natural crack from FIB milled notch.

After the initial proposal of bridge notches [83] and FEM calculations on bridge geometry [7], Zhang et al. [104] first reported experimental observation of load drops as evidence of bridge failure in displacement-controlled loading condition. In Section 3.3, bridge failure is also recorded in the single crystalline silicon under certain geometrical condition. Similar to the existing literature, load drops preceding crack arrest was observed in a displacement-controlled experiment. Then the new FIB-independent natural crack at the edges of crack plane close to the free surface of the cantilever grows towards the center of the crack plane and propagates in an unstable manner.

Load drops indicative of bridge failure were only observed at thin material bridges and deep notches. Although this is tandem with the expected range from finite element calculations [7], the

region where bridge failure is observed slightly deviates from the previous study of [104] where bridge failure was observed at a/W of 0.3 and $1-b/B$ of 0.07 in CrN/AlN multi-layers and CrN hard coatings. A possible reason for this is that bridge failure is happening too fast to be captured in some samples. This is particularly relevant in silicon as model material, which is much more brittle than the hard coatings in the previous work from Zhang et al. [104] Secondly, difference between idealized simulated geometry and FIB milled experimental geometry, with the latter having rounded corners and potentially a cantilever taper, can introduce differences in the stress intensity factor [104]. Hence, the stress intensity ratio, f_{corr} in the experimental geometry may differ from the one calculated from the idealised geometry used in the FEM calculations. This could be responsible for the shift of the region where crack arrest is observed (Figure 3.4 and 3.5).

Although bridge failure was observed for most samples with deep notches and thin material bridges, data analysis is limited to a/W less than 0.4 because beyond this range there is an additional geometrical contribution from the increased compliance of the cantilever as the crack approaches the neutral axis of the beam [7]. It is worth noting that the K_{IQ} of the samples with thin material bridges was within the expected range for single crystalline silicon [33,170], irrespective of the notch depth and observation of crack arrest. This results can be attributed to similar stress intensities at thin bridges and the notch.

Also, from Figure 3.7, it was seen that there is no significant difference between the bridge notch and through-thickness notch fracture toughness for the silicon cantilevers. This is unlike the report of Zhang et al. [104] where possible Ga^+ embrittlement at the bridge led to a reduced bridge notch fracture toughness in CrN/AlN multi-layers and CrN hard coatings. One explanation for this discrepancy to the work presented in this chapter is the use of single crystalline silicon here, which might not be that prone to FIB damage at the milling conditions used in this chapter [33].

3.4.2 Geometry for valid fracture measurement

In Section 3.3.1 it was seen that the apparent fracture toughness increased with increasing bridge widths at fixed notch depths (shallow and deep notches). This increase in apparent fracture toughness has been attributed to crack tip shielding of the notch front in bridge-notched single cantilever beams [7] because the location of the highest stress intensity is shifted from the notch to the inner corners of the bridge. Hence, fracture in geometries with thick bridges is dominated load bearing capacity of the bridges. As the bridge thickness is increased, the cantilever becomes stiffer, and apparent toughness is increased too.

Figure 3.9 shows a cumulative distribution plot of the fracture toughness calculated for different silicon cantilevers with similar notch depth (a/W between 0.3–0.4). K_{IC} represents data from cantilevers which showed crack arrest, and a through-thickness notch assumption is used for analysis. For cantilevers where crack arrest was not observed, K_{IQ} is calculated using through-thickness notch assumptions, while $K_{IQ_corrected}$ is calculated including correction for the bridge notch geometry. It is seen that the cantilevers which did not crack arrest have higher apparent fracture toughness irrespective of the assumptions used in the calculations. Furthermore, the use of f_{corr} to correct for the bridge geometry in the samples led to a further overall increase in apparent fracture toughness. This could suggest that f_{corr} calculated from the simulations is not adequate for correcting the samples in the current study or that the bridges suffer from severe FIB damage

Additionally, it is observed from Figure 3.9 that the samples where crack arrest do not occur (K_{IQ} and $K_{IQ_corrected}$) have more scatter compared to K_{IC} . This huge scatter can be linked to FIB artefacts and imperfections at the bridge notch, which is not reproducible between samples [104]. This means that the contributions of experimental imperfections to the fracture investigations is higher when crack arrest is absent in bridge-notched cantilevers.

Therefore, it is recommended from this work that thin material bridges and deep notches should be used to promote bridge failure and crack arrest in bridge-notched single cantilever beams. In addition, bridge failure can only be accounted for when it is observed by load drops in an *in situ* experimental setup. If both conditions are fulfilled, then through-thickness notch assumptions can be used to extract valid fracture data from bridge-notched single cantilever beams.

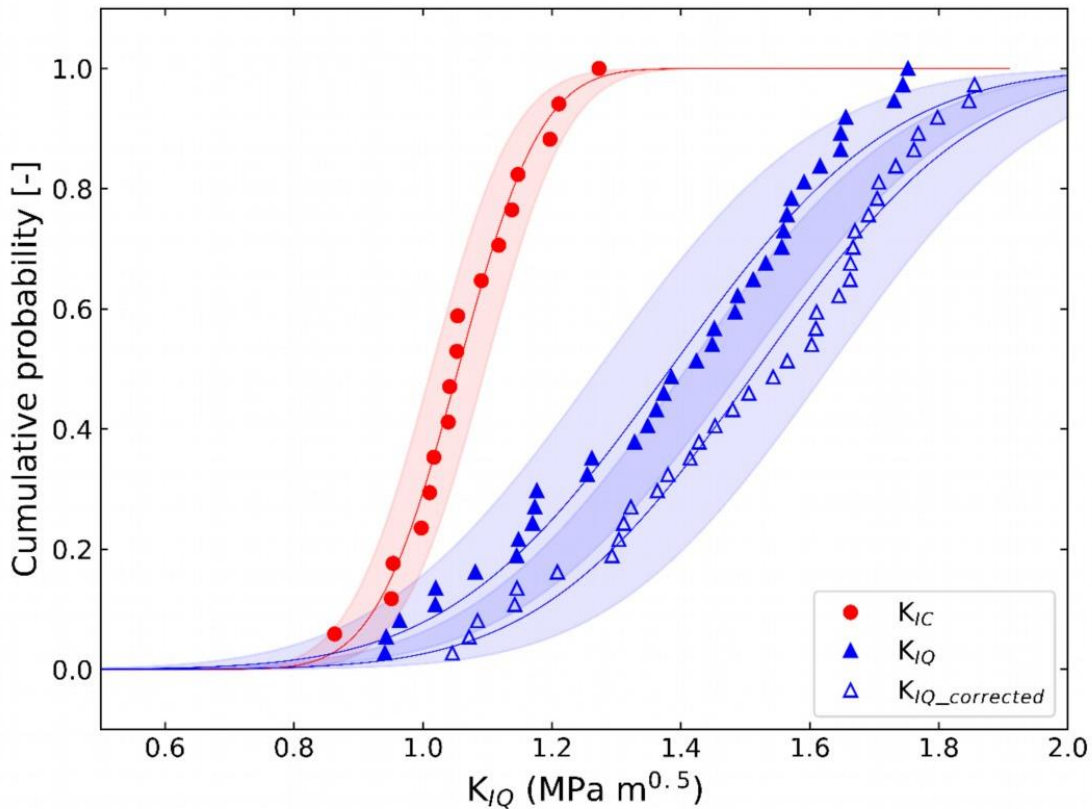


Figure 3.9: Cumulative distribution of fracture toughness in silicon cantilevers with crack arrest assuming a through thickness notch (K_{IC}), and apparent fracture toughness (K_{IQ} and $K_{IQ_corrected}$) for cantilevers without crack arrest.

3.4.3 Fracture toughness of silicon

It is expected that the fracture toughness is geometry independent [1,27,33,144], since silicon has a small plastic zone size and the critical sample dimensions are sufficient to maintain plane strain conditions. Si (111) being the lowest resistant fracture planes is expected to have lowest fracture toughness compared to other crystallographic planes [171]. At the bulk scale, the fracture toughness of the Si (111) cleavage plane scatters between 0.65 and 1.0 MPa m^{0.5} based on different measurement methods [172]. Similarly, Tanaka et al. [171] reported fracture toughness of 0.69 MPa m^{0.5} from indentation tests, while 1.1 ± 0.02 MPa m^{0.5} was reported from single cantilever

based studies by [82] (pentagonal beams) and [85] (triangular beams). In the latter studies, high fracture toughness was attributed to influence of FIB artefacts at notch root. In a recent study, DelRio et al. [99] measured fracture toughness for Si (111) using double cantilever beam (DCB). Stable crack growth in the DCB experiments made it possible to calculate fracture toughness with increase crack lengths. Final fracture toughness values between 0.7 and 0.9 MPa m^{0.5} was measured after the crack grew beyond the region with FIB artefacts. After correcting for frictional effects in longer cracks, the authors reported fracture toughness of 0.72 ± 0.07 MPa m^{0.5}, which is lower than the values recorded in through thickness after crack arrest. These literature values indicate a scatter in the fracture toughness of Si (111) measured using different geometries. The fracture toughness (K_{IC}) measured in this chapter for a through-thickness notch after crack arrest in Si (111) is 1.1 ± 0.1 MPa m^{0.5}, which is within reported range of 0.7 and 1.3 MPa m^{0.5} for single crystalline silicon [169].

3.5 Conclusion

In this chapter, experimental methods were used to elucidate the region where bridge failure is expected in single crystalline silicon. Cantilevers with $a/W > 0.30$ and $l-b/B < 0.05$ show obvious bridge failure during *in situ* testing. The result suggests the K_{IQ} is overestimated in samples with thick material bridges regardless of the incorporation a bridge notch correction factor. Fracture toughness (K_{IC}) of 1.0 ± 0.2 MPa m^{0.5} and 1.1 ± 0.1 MPa m^{0.5} was calculated from the bridge notch and through-thickness notch, respectively, indicating that there is no substantial between the bridge and notch fracture toughness in silicon. The findings show that the absence of crack arrest in bridge-notched single cantilever beams leads to inaccurate geometry-dependent fracture toughness calculations.

4.0 Role of notching ion species on fracture toughness of single crystalline silicon

Chapter 4 is intended to be submitted as a journal publication.

The subsequent researchers have contributed to the experiments and their interpretation. A detailed description of the individual contributions can be found in the appendix.

E. Okotete¹, S. Lee¹, C. Kirchlechner¹.

¹Institute for Applied Materials, Mechanics of Materials and Interfaces, Karlsruhe Institute of Technology

4.1 Introduction

Crack arrest preceding unstable fracture in single cantilever bending experiments has recently been successfully observed in the small scale fracture community and similar results have also been presented within this thesis (Chapter 3). In these works, notches were made using Ga⁺ beam which introduces artefacts including impurities and crystal defects at the notch root which change the stress state of the notch, and thus the fracture toughness [32]. For instance, chemical interaction of Ga with copper leads to the formation of secondary phases in the exposed region [173]. Additionally, liquid metal embrittlement caused by gallium segregation to grain boundaries in selected metals has been extensively reported to change the fracture behaviour of materials [163,174,175]. Thus, alternative ion species have been scantily considered to replace Ga⁺ for preparing notches for micro fracture experiments [8,148].

As stated in the previous chapter, silicon is a model material for MEMS applications which has been the centre of many micro fracture investigations. However, there are still many open topics including complexities such as BDT, fracture anisotropy, initiation fracture toughness and associated environmental effects [33,85] which herald its fracture behaviour. At small length scales, the influences of the above-named factors on the fracture response of single crystalline silicon are still rudimentary. A couple of studies have looked at the BDT phenomenon in micro fracture of silicon [23,24] but these experiments are quite challenging because of the difficulties associated with micro fracture testing at higher temperatures. Particularly, the effects of the notch root radius and impurities at the notch on the fracture of single crystalline micro cantilevers have received minimal attention till now.

Within this chapter, the role of chemically inert ion species on fracture toughness in single crystalline silicon will be investigated. In addition to the absence of chemical interactions at the notch, the small probe size of gas field ion sources (GFIS) (0.25 nm for helium and 2 nm for neon) [54,176,177] as well as smaller beam tails [178] compared to Ga⁺ ion source apparently makes these alternative ion species a good choice for making FIB notches. The high resolution of the

GFIS arises from how the ion beam is generated. A GFIS consist of a tungsten needle electrode (emitter) with a three-sided pyramid structure at its apex [177,179]. The apex of the emitter is shaped to attain a stable three-atom configuration known as a trimer [54,179] and held at high voltage. When helium (neon) gas is supplied to the emitter, the atoms are ionized by the high electric field at the trimer, and the ions are extracted and accelerated through the optical column [54,177,180]. In typical operations, the beam is aligned to select emission from a single atom from the trimer resulting a small source size [179,181]. Neon and helium are two noble gases used in GFIS microscopes because they possess high ionization energies relative to impurities which could attack the emitter [182,183]. Hence, these two ions are used for imaging and nanofabrication in commercially available ion microscope from Zeiss Microscopy. Neon is preferred for this investigation because of its high sputter yield (~ 20 times higher) and less damage (~ 5 times less) in silicon compared to helium [183–185]. Currently, there are very few studies which have explored alternative ion species for notch preparation within the micro fracture community. In this work a systematic study on the use of GFIS for preparing sharp notches will be presented using silicon, a material of know fracture toughness. In this work, neon GFIS will be used to notch silicon micro cantilevers produced via batch process (Chapter 3, section 3.2). The subsequent sections present the steps taken to optimise milling conditions for notch fabrication using neon GFIS. Thereafter, the fracture toughness of the neon-notched micro cantilever is calculated and analysed.

4.2 Experimental details

Single crystalline silicon on a SOI wafer presented in section 3.2 was also used in the fabrication of the micro cantilevers investigated in this chapter following experimental procedures outlines in section 3.2.2.

4.2.1 Notching, annealing and *in situ* SEM testing of cantilevers

Line notches were milled using a helium ion microscope (HIM) equipped a neon ion source (Orion Nanofab, Zeiss AG, Germany). For each experiment, imaging and sample alignment were done using the helium ion source at 25 kV and 5 pA. Then the GFIS is switched to neon source for the line cuts to make notches. The neon gas pressure of 7.3×10^{-6} mbar as maintained at the ion source for the generation of the ion beam. The brightest of the three atoms (trimer) at the tungsten tip is selected and used for subsequent milling operations. 20, 40 and 70 μm diameter apertures and varying spot control parameters were used to achieve currents between 10 and 20 pA. The acceleration voltage of the neon ions was also varied between 10, 15 and 25 kV to observe the influence of beam energies on the silicon-ion interaction. Nanopatterning visualization engine (NPVE) was used to mill the line patterns at doses of 1 nC/ μm and dwell time of 1 μs . After notching, selected samples were annealed in a vacuum of 2.9×10^{-5} mbar at 450 °C for 1 hour and 750 °C for 90 minutes in a quartz tube within a tubular furnace. Then all micro cantilevers were tested in the same *in situ* SEM deformation setup presented in section 3.2.4.

4.3 Results

4.3.1 Analysis of data from *in situ* test

Load-displacement plot similar to what is observed in the Ga⁺ notched cantilever is presented in Figure 4.1. Load drops signifying failure at both bridges before final fracture are also seen in the plot. Hence, fracture toughness calculations using through-thickness notch assumptions can be made on cantilevers where crack arrest occurs. When crack arrest is not observed from the load-displacement experiments (no load drops), an apparent toughness is used for the analysis.

The fracture toughness (K_{IC}) at the through-thickness notch and the bridge notch fracture toughness (K_{IC}^*) is calculated for cantilevers where crack arrest was observed using Eqn. 4.1 and 4.2,

$$K_{IC} = \frac{F_C L}{B W^{3/2}} f_{Matoy} \left(\frac{a}{W} \right) \quad (4.1)$$

$$K_{IC}^* = \frac{F_B L}{B W^{3/2}} f_{Matoy} \left(\frac{a}{W} \right) \frac{1}{f_{corr}} \quad (4.2)$$

where F_C — maximum load at fracture, L , B , and W — are length, width, and thickness of the cantilever, a — notch length, f_{Matoy} — is a geometry correction factor and f_{corr} — is a bridge notch correction factor. In samples where there is no observation of crack arrest, the conditional fracture toughness (K_{IQ}) using the final failure load is calculated in Eqn 4.1 assuming a through-thickness crack and corrected for the bridge notch geometry (Eqn 4.3).

$$K_{IQ_corrected} = \frac{K_{IQ}}{f_{corr}} \quad (4.3)$$

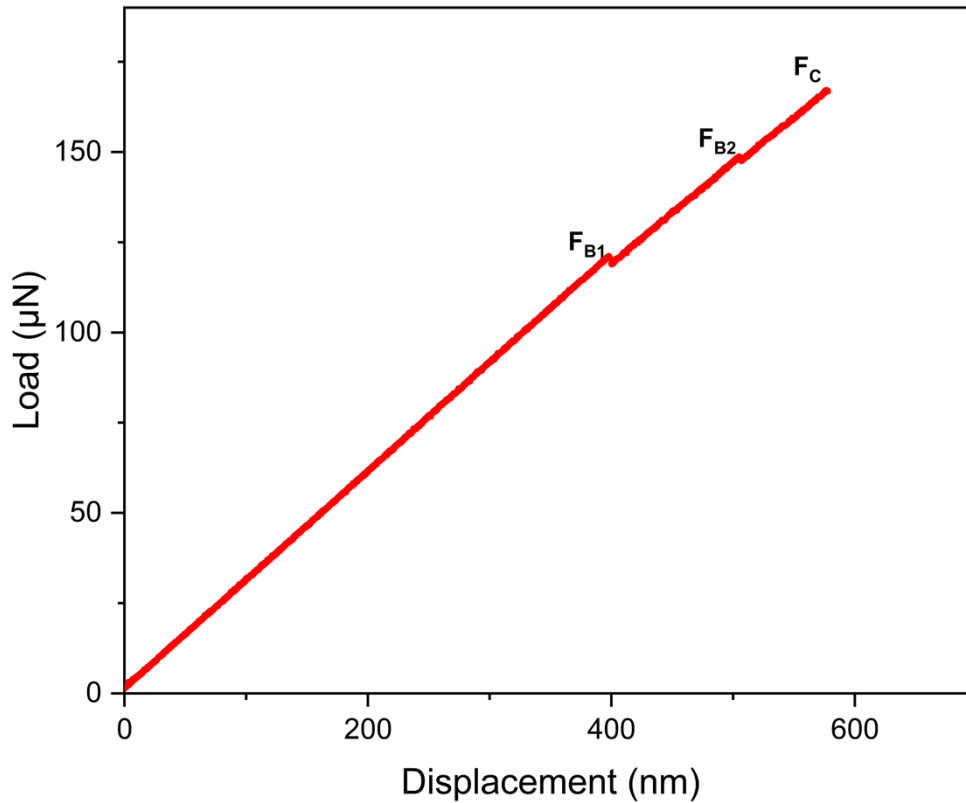


Figure 4.1: Load-displacement plot of a neon bridge-notched silicon cantilever showing crack arrest.

4.3.2 Effects of ion beam aperture size

In this section the influence of critical parameters of notch preparation using neon ions is presented. Firstly, notches were milled using different beam apertures to find a good balance of resolution and beam current since larger beam currents were needed to mill deep notches. The samples tested here did not show crack arrest, hence the results of apparent fracture (K_{IQ}) toughness are presented. Figure 4.2 shows the apparent fracture toughness of micro cantilevers milled with three different neon ion beam apertures and tested in SEM. The notches in these cantilevers were milled using acceleration voltage of 10 kV, and it can be seen that K_{IQ} varies with different aperture sizes used for preparing the notches. $K_{IQ_corrected}$ is used to analyse the data from the experiment to include the correction of bridge geometry. From the results, it is observed that notches produced using the 70 μm and 40 μm diameter apertures resulted in higher average corrected apparent fracture toughness values ($2.1 \pm 0.1 \text{ MPa m}^{0.5}$ and $2.0 \pm 0.4 \text{ MPa m}^{0.5}$, respectively) compared to notches fabricated using 20 μm aperture ($1.8 \pm 0.3 \text{ MPa m}^{0.5}$). The large scatter in the average apparent toughness has been linked to milling imperfections at the bridge notch which cannot be replicated between samples [104]. On the other hand, increase in apparent fracture toughness with increasing aperture diameter can be attributed to a larger convergence angle of large-diameter apertures which results in a broader beam diameter [186,187].

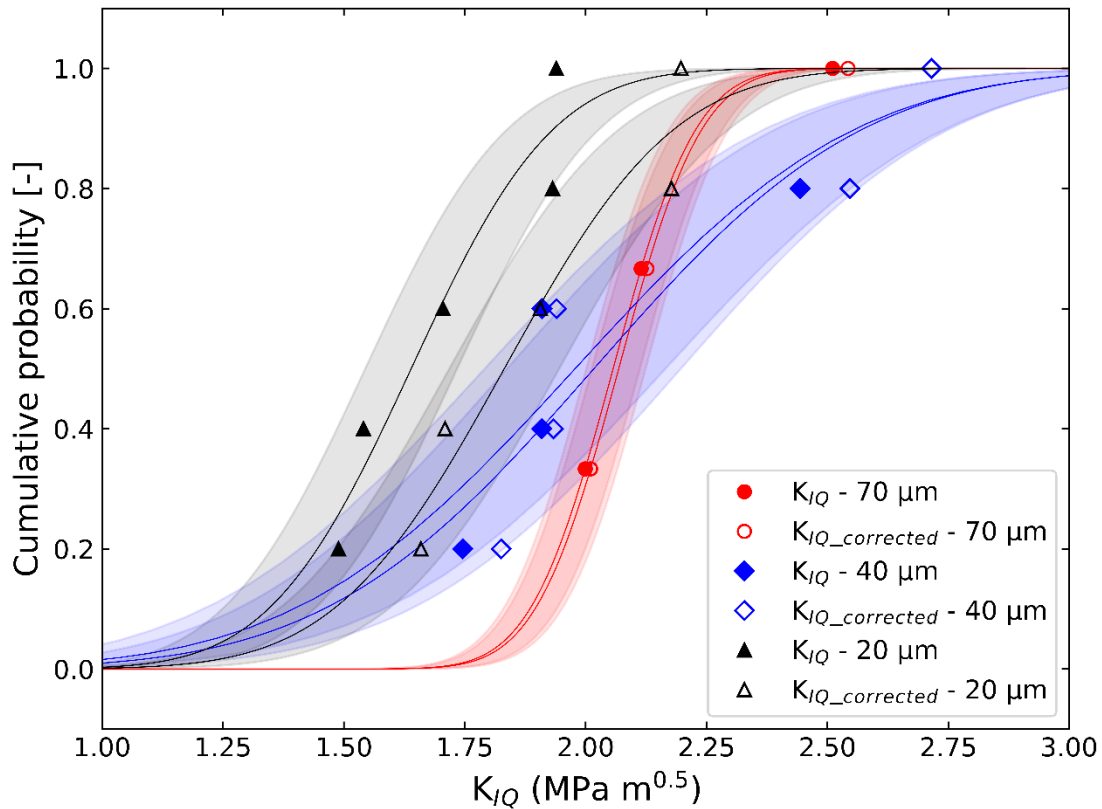


Figure 4.2: Cumulative distribution of influence of aperture diameter on apparent fracture toughness of silicon. Note that bridge failure and subsequent crack arrest was not observed in these samples.

4.3.3 Effects of ion beam energy

The 20 μm diameter aperture was further used to mill the notches for all the micro cantilevers since it produced the sharpest beam of all available apertures in the microscope. Another parameter critical to making notches using the neon source is the acceleration voltage because the impact energy of ions affects both the penetration depth and sputter yield in the target sample [184,188]. SEM images (Figure 4.3a–c) show that the width of milled notches increases with reducing acceleration voltages. At 25 kV (Figure 4.3c), the notch opening is seen to have narrowest width (95 nm) compared to other beam energies suggesting a small notch root-radius. This is because the beam probe size increases with decreasing acceleration voltages due chromatic aberrations leading to loss of resolution [189–191].

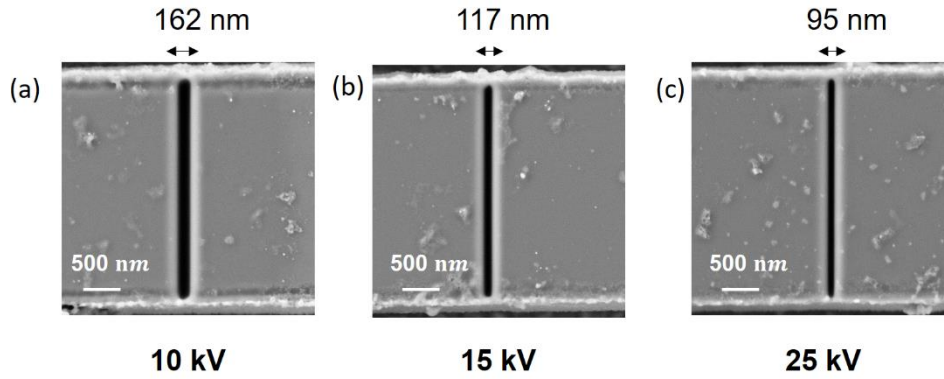


Figure 4.3: SEM images showing the top view of notches milled at beam energies (acceleration voltages) of (a) 10 kV, (b) 15 kV and (c) 25 kV. (d) Cross-section SEM image showing sub-surface damage in a fractured cantilever.

The effect of the notch radius on fracture toughness and apparent fracture toughness in cantilevers notched with different acceleration voltages notched is presented in Figure 4.4 and 4.5 for samples where crack arrest was present and absent, respectively. In Figure 4.4 the fracture toughness at the bridge (K_{IC}^*) and fracture toughness (K_{IC}) of the samples with crack arrest is shown. It is observed that the notch with the smallest width (milled at 25 kV) shows a large difference between K_{IC}^* and K_{IC} ($1.3 \pm 0.1 \text{ MPa m}^{0.5}$ and $1.6 \pm 0.2 \text{ MPa m}^{0.5}$, respectively). This is contrary to what was reported for 30 kV milled gallium notches in the last chapter, where there was no appreciable difference between fracture toughness at the bridge notch and through-thickness notch. Notches milled with the other two acceleration voltages had average bridge notch and through-thickness notch fracture toughness in the same range ($1.3 \pm 0.1 \text{ MPa m}^{0.5}$ and $1.2 \pm 0.1 \text{ MPa m}^{0.5}$, respectively), with marginal differences in both values, similar to gallium milled notches. It is also important to note that the bridge notch fracture toughness is comparable for notches produced with all three acceleration voltages. However, there is an apparent increase in fracture toughness at the through thickness notch milled with 25 kV acceleration voltage.

The apparent fracture toughness of samples without crack arrest is analysed before and after bridge geometry correction (Figure 4.5). For 25 kV milled notches, the average apparent fracture toughness is $1.3 \pm 0.1 \text{ MPa m}^{0.5}$ and $1.4 \pm 0.2 \text{ MPa m}^{0.5}$ before and after correction (K_{IQ} and $K_{IQ_corrected}$), respectively. The increase in average apparent fracture toughness after correction was linked to possible limitations of the correction factors in the last chapter. Noteworthy is the similarity of the apparent fracture toughness to bridge notch fracture toughness in samples with crack arrest (K_{IC}^*) for these 25 kV notched cantilevers. This corroborates the assertion that outside direct observation of bridge failure, it is unclear if fracture experiments reflect the conditions at the true thickness notch or at the bridge notch. The average apparent toughness for the notches milled with 15 kV acceleration voltage was within the same range as 25 kV milled notches before bridge geometry correction ($1.3 \pm 0.2 \text{ MPa m}^{0.5}$). After correction, the apparent toughness is increased further to $1.5 \pm 0.2 \text{ MPa m}^{0.5}$. The highest average apparent fracture toughness was recorded for 10 kV milled notches, $1.6 \pm 0.3 \text{ MPa m}^{0.5}$ and $1.8 \pm 0.3 \text{ MPa m}^{0.5}$ before and after correction. The 50 % increase between K_{IC} and $K_{IQ_corrected}$ for 10 kV milled notches re-emphasizes why observation of bridge failure is necessary for accurate measurements. Furthermore, high

values of $K_{IQ_corrected}$ with large scatter can possibly be measured due to milling imperfections when the notch is milled using low acceleration voltage.

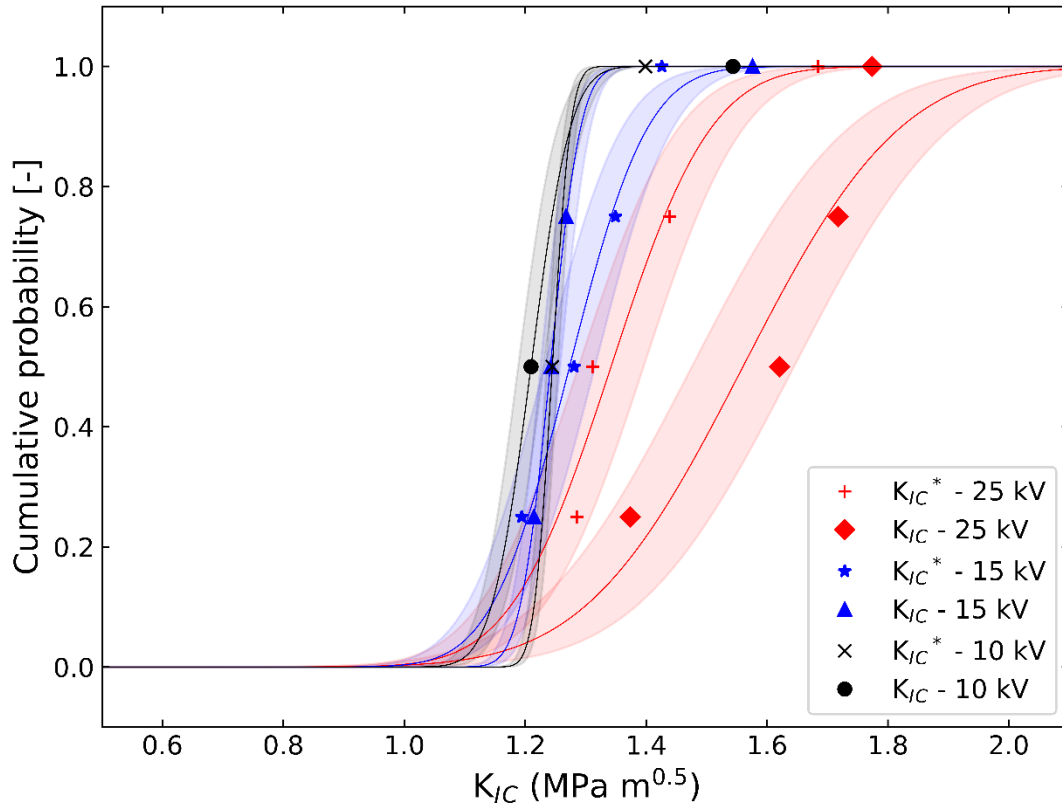


Figure 4.4: Cumulative distribution of through-thickness fracture of toughness and bridge fracture toughness of silicon cantilevers notched with different beam energies.

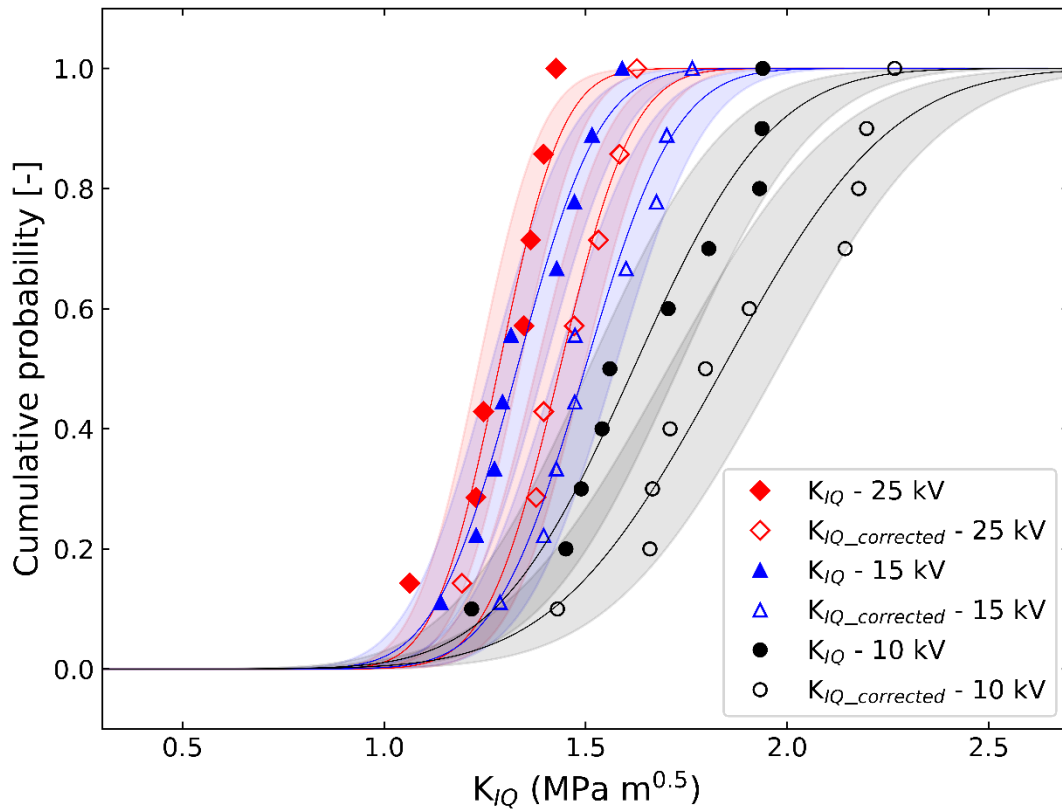


Figure 4.5: Cumulative distribution of corrected and uncorrected apparent fracture of toughness of silicon cantilevers notched with different beam energies.

Post mortem SEM images of the fractured samples notched with different acceleration voltages is shown in Figure 4.6 a–c. Firstly, it can be seen that the sputter yield of silicon using neon ions reduces with increase ion beam energy (see reduced notch depth at same dose). This observation is unlike what is observed for heavier ion species like Ga^+ where sputter yield increases with increasing beam energy (could decrease at very high impact energies). The reason for this will be discussed later in this chapter. Secondly, the notch appears to have some artefacts distributed across the surface due to neon interaction with silicon. Studies have shown that these artefacts are gas-filled bubbles form below the surface when neon is implanted in silicon at high doses [184,192,193]. A schematic of layers of sub-surface damage present in silicon that result from neon ion interaction at increasing doses is shown in Figure 4.7. When fabricating relatively deep notches, the doses required will lead to some degree of sub-surface damage at the notch. Figure 4.6a–c displays the extent of sub-surface damage on the notches of silicon micro cantilevers at a dose of $1 \text{ nC}/\mu\text{m}$ for different acceleration voltages. In Figure 4.6a, it is observed that the bubble layer is primarily concentrated around the notch root for the 10 kV milled notch. As the acceleration voltage increases, the damage layer spreads across the entire notch. The notch surface of the cantilever milled with neon ions accelerated at 25 kV (Figure 4.6c) shows the highest sub-surface damage distribution, which includes bubbles with different diameters.

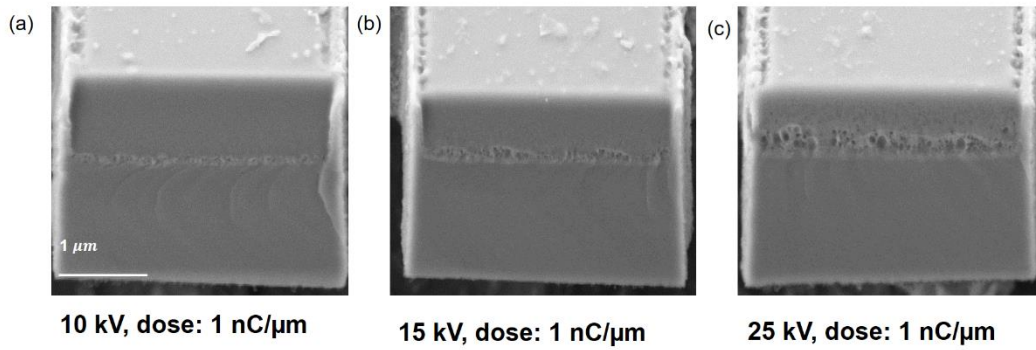


Figure 4.6: Fracture cross section of cantilevers milled with (a) 10 kV, (b) 15 kV and (c) 25 kV beam energies.

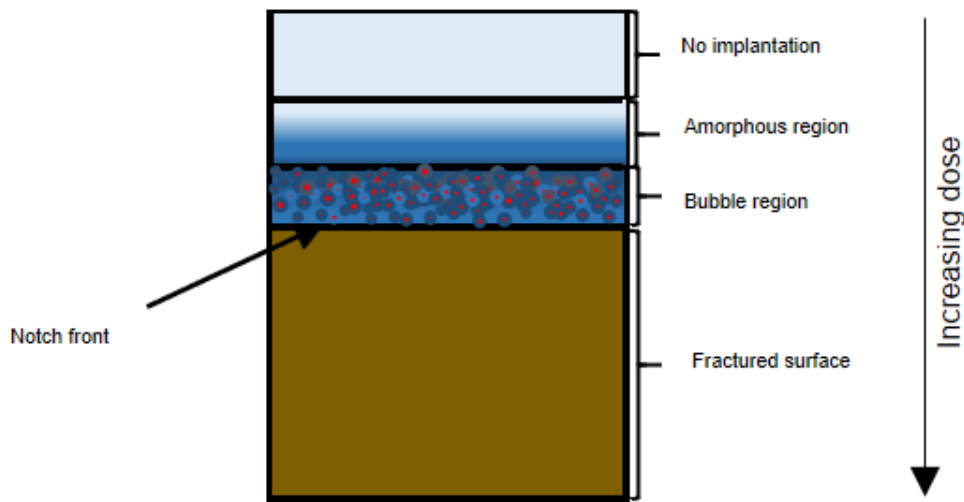


Figure 4.7: A sketch of damage layers after neon ion beam interaction.

Although notches of a few nanometre widths were fabricated using the neon ions (as shown in Figure 4.3c), the presence of bubbles at the notch leads to high apparent fracture toughness for the silicon micro cantilevers. The bubble density is reduced using ions accelerated at low voltages, but the notches become wider.

4.3.4 Effects of annealing

One of possible approaches to minimize the artefacts from the bubbles is annealing at moderate temperature which can get rid of trapped gas and release residual stress at the notch front. Annealing temperatures were selected in the range where noticeable instability of bubbles (formed from ion implantation) have been reported in literature [193–195]. In Figure 4.8, the evolution of the damage in the notch as a function of annealing temperature at different ion beam energies is presented. Comparing the SEM images before (Figure 4.8a–c) and after annealing at 450 °C (Figure 4.8d–f), there is no noticeable change in the fractured images at the SEM resolution for all ion beam energies investigated. On the other hand, a porous-like structure is seen in the *post mortem* SEM images of the samples annealed at 750 °C shown in Figure 4.8g–i. This structure can be described as a combination of pores and empty cavities / holes. After the annealing treatment,

the 25 kV milled notch displays a higher density of small, closely packed pores compared to the other two notches. Around the notch front, larger holes are seen which could be significant of bubbles breaking. Beyond the region with holes, a clean and sharp notch front is seen for all the samples, suggesting the absence of ion-induced damage.

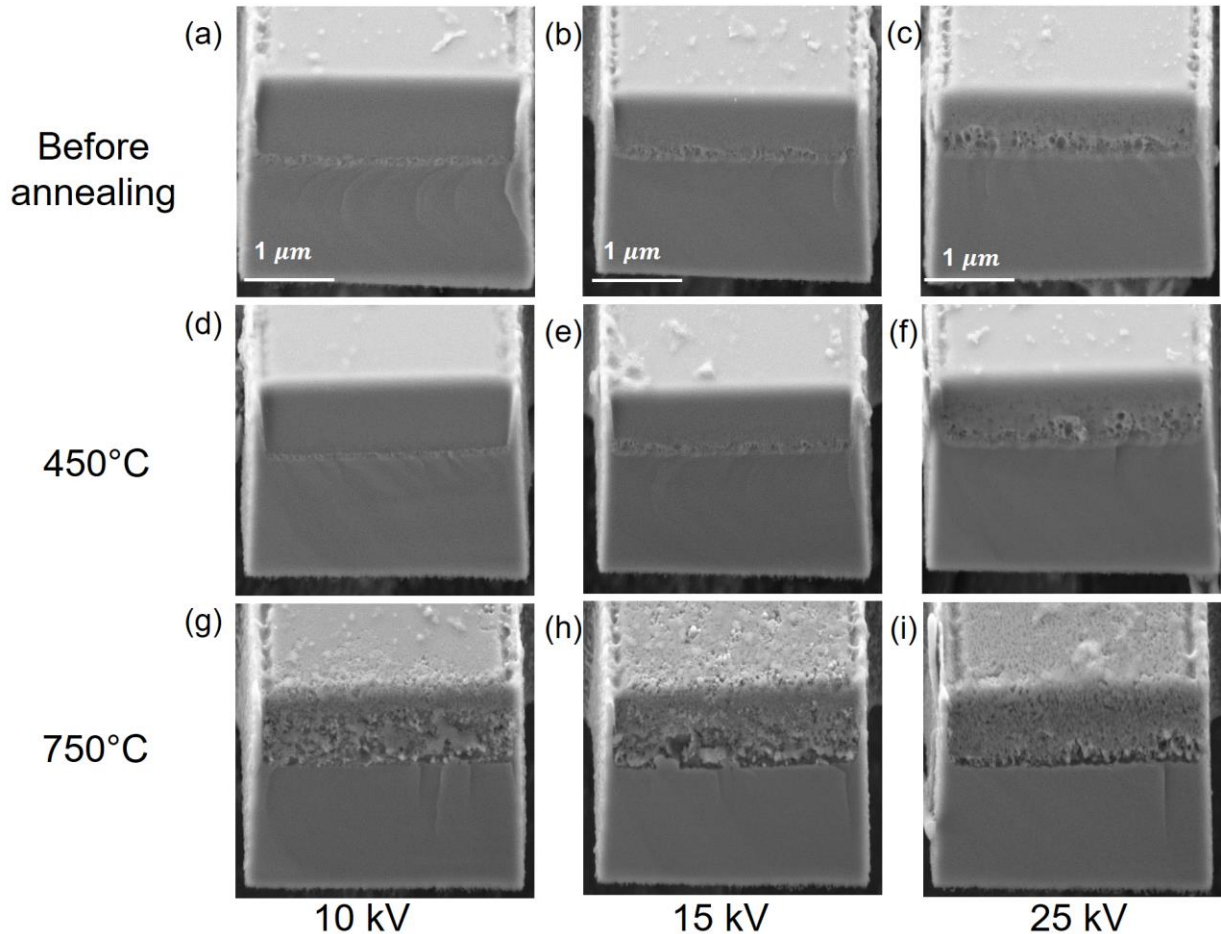


Figure 4.8: Influence of annealing on fracture morphology of cantilevers notched using different acceleration voltages.

In Figure 4.9, the impact of annealing on the fracture toughness of tested silicon cantilevers is shown. The data is presented for samples that showed crack arrest, hence the through thickness fracture toughness is discussed. It is seen the fracture toughness of cantilevers before annealing had more scatter with increasing notch depth compared to the annealed samples. After annealing, the fracture toughness of the cantilevers has decreased significantly, which could be attributed to the recovery of the damaged region. The average fracture toughness reduced from $1.4 \pm 0.3 \text{ MPa m}^{0.5}$ before annealing to $1.2 \pm 0.1 \text{ MPa m}^{0.5}$ after annealing at $450 \text{ }^\circ\text{C}$. The same holds for annealing at $750 \text{ }^\circ\text{C}$, which also resulted in an average fracture toughness of $1.2 \pm 0.1 \text{ MPa m}^{0.5}$. These results are averaged for notches milled with different acceleration voltages. However, as mentioned in Section 4.3.2, the sub-surface damage at the notch is dependent on the beam energy. Figure 4.10 illustrates the impact of annealing on fracture toughness of notches created with 25 kV acceleration voltage, because these notches had the

smallest width (notch radius) and highest largest distribution of subs-surface damage. An obvious shift of the distribution curve to the left is seen after annealing at both temperatures. In these notches, average fracture toughness reduced to $1.1 \pm 0.1 \text{ MPa m}^{0.5}$ after annealing at both $450 \text{ }^\circ\text{C}$ and $750 \text{ }^\circ\text{C}$, respectively, from $1.6 \pm 0.2 \text{ MPa m}^{0.5}$ before annealing. There is also a reduced scatter in the fracture toughness of the annealed samples. The results indicate that both annealing temperatures are potentially suitable for reducing the impact of neon ion interactions in silicon, despite the absence of visual changes in the *post mortem* SEM image of samples annealed at $450 \text{ }^\circ\text{C}$ (compare Fig. 4.8 b and e).

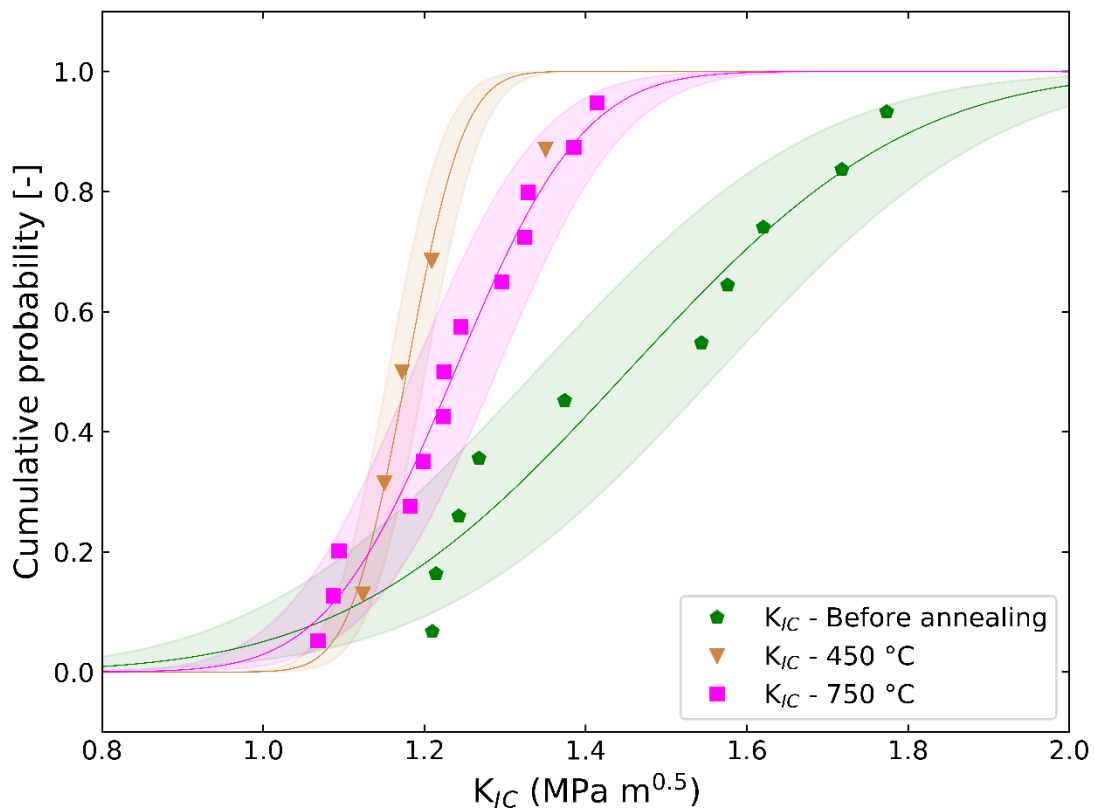


Figure 4.9: Cumulative distribution of through-thickness fracture toughness of as-milled and annealed notches averaged for different acceleration voltages.

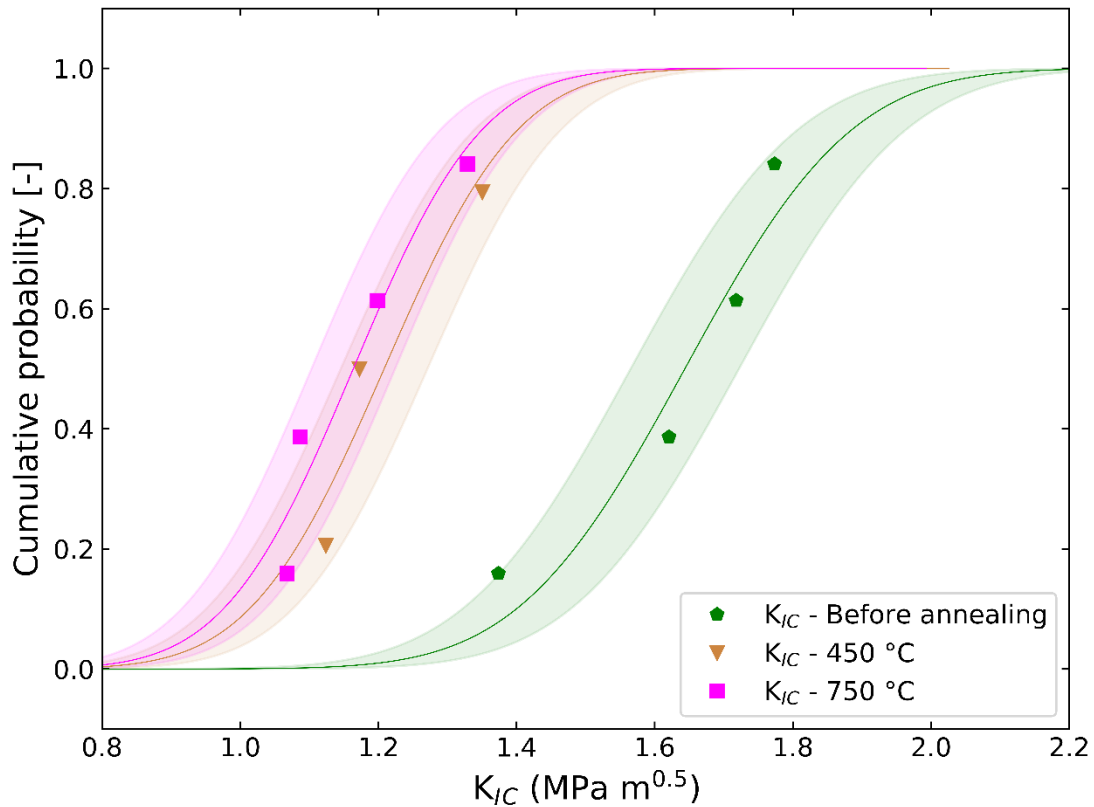


Figure 4.10: Cumulative distribution of fracture toughness of 25 kV milled through-thickness notches, before and after annealing.

4.4 Discussion

4.4.1 Sputtering efficiency of silicon using neon ions

During a sputtering event, the energy of an incident ion is transferred to a target material through electronic and nuclear collisions [6,188,196]. Electronic collision occurs when the incident energy is transferred to electrons of the target material, resulting in ionization and excitations of the target material. On the other hand, nuclear collision results in the transfer of energy to the target material's nuclei, causing displacement of surface atoms from the target material when the binding energy is exceeded [196,197]. In addition, recoil atoms generated during nuclear collision also lose energy in the target after some time through either nuclear or electronic stopping. The depth of penetration and the efficiency of sputtering in a target material are determined by the mass of the incident ion and the energy of the beam [184].

In the case of very light elements like helium, the energy of the ion is mainly dissipated through electronic collisions, as the low mass and small nuclear charge prevent nuclear collisions leading to a lower sputtering yield [184,188]. According to simulations carried out using Transport of Ions in Matter (TRIM) and Stopping and Range of Ions in Matter (SRIM), the sputter yield of silicon with neon ions reaches its peak at 10 kV [184,188,198]. Beyond this value, the interaction between ion and target atom moves from majorly nuclear collisions at the surface to sub-surface interactions

[184]. Also, the depth of an amorphous layer produced as a result of neon interaction with silicon increases with beam energy [176,184].

4.4.2 Damage evolution and annihilation in silicon

Damage density and depth in silicon after exposure to neon and helium are a function of dose, even with optimal sputtering yield. When the neon exposure surpasses a critical level of 1×10^{15} ions cm^{-2} , an amorphous region is created in silicon as a result of events that occurred during the collision cascade [199]. With higher doses, the depth of the amorphous layer increases, and neon-filled nanobubbles form inside the amorphous region [184]. These bubbles are balloon-like structures created by the deformation of the amorphous silicon layer caused by neon implants that become trapped in the subsurface. As the dose increases further, the diameter and distribution of the bubbles in the initial amorphous region increase due to loop punching and Ostwald ripening, which result from higher local ion concentration [184,200–202].

It is obvious from the SEM images in Figure 4.4 that critical doses for bubble formation was surpassed in milling the notches for the micro cantilevers in this chapter. Thermal treatment of helium and neon implanted silicon have been reported in different studies [203–206]. After annealing the notches at 750 °C (Figure 4.8), the fractured SEM images show features similar to irregularly shaped craters and surface blisters which have been reported for neon implanted silicon at annealing temperatures between 600 °C and 800 °C [193–195]. These features evolve from growth of bubbles in the amorphous region of the implanted silicon during annealing which eventually leads to blistering of the surface [194]. When the blisters break the neon gas is released, and flakes are observed on the surface [194,195]. This could be the reason for the sharp notch front seen in Figure 4.8 after annealing at 750 °C after release of neon bubbles. Recrystallization of the amorphous silicon by layer-by-layer solid epitaxial growth is likely suppressed during annealing because of large concentration of inert gas in the amorphous layer [193].

4.4.3 Fracture toughness of neon notched micro cantilevers

The silicon cantilevers tested had zero exposures to Ga^+ ion source, since they were fabricated by lithography and notched using GFIS. Hence, there will be no effect of chemical interaction and segregation at the notch. However, the results show two artefacts present which can affect measured fracture values. On one hand, sharp notches introduce lots of ion-induced damage at the notch. This damage introduced compressive residual stresses at the notch and resulted in about 40 % increase in apparent fracture toughness. Reducing the ion-implantation at the notch by changing notching parameters results in relatively blunter notches with an even higher fracture toughness.

Thermal treatment of the sharper notches results in average fracture toughness of $1.1 \pm 0.1 \text{ MPa}\cdot\text{m}^{0.5}$ which is similar to $1.1 \pm 0.1 \text{ MPa}\cdot\text{m}^{0.5}$ calculated for notches produced with Ga^+ (Chapter 3). These results show that neon ions might not be very suiting for making notches in silicon because of bubble formation at the notch. However, the density and damage layer distribution is material dependent. Hence, neon ions might be suitable for other material systems.

4.5 Conclusion

The potential of neon as a candidate for making FIB notches for fracture investigations was investigated in this chapter using silicon as a test material. It was seen that neon ions are capable of producing sharp notches in silicon using 25 kV acceleration voltage. However, this was at the expense of sub-surface bubbles, which are as a result of the neon ion-silicon interaction. Annealing milled notches helped to get a sharp notch front. The final post annealing fracture toughness is $1.1 \pm 0.1 \text{ MPa}\cdot\text{m}^{0.5}$ which is similar to the values recorded for gallium notched silicon beam, indicating that there are no significant changes of the obtained fracture toughness using inert ion species.

Based on the findings of chapters 3 and 4, it can be concluded that gallium milled notches are sufficient to obtain fracture toughness that represents material properties in silicon, provided that well-shaped bridge notches are made to promote crack arrest before failure. In contrast, neon notched cantilevers require an additional annealing step to achieve the expected fracture toughness of silicon. It is still unclear whether this conclusion will apply to other material systems that exhibit less subsurface damage after neon interaction

5.0 Novel single cantilever delamination geometry for fracture toughness measurements

Chapter 5 is based on a published journal article.

E. Okotete, S. Brinckmann, S. Lee, C. Kirchlechner, How to avoid FIB-milling artefacts in micro fracture? A new geometry for interface fracture, *Mater. Des.* 232 (2023) 112134. <https://doi.org/10.1016/j.matdes.2023.112134>

A detailed description of the contributions of all the researchers involved in experiments and interpretations can be found in the appendix.

5.1 Introduction

Several geometries (see Section 2.4.2) have been used in the last two decades to extract fracture toughness from small volumes. The question which is most prominent in the community is the reliability of existing techniques with respect to sample fabrication and testing conditions. FIB milling is the most effective way to make notches since fatigue pre-cracking has limited successes at small length scales [85,207]. However, imperfections at the notch from the ion-material interactions raise a concern which is detrimental to fracture studies. In the last two chapters of this thesis, investigations focussed on improving measurements from a single cantilever beam test geometry. In both cases, the experiments were targeted at reducing chemical impurities at notches which directly affect fracture toughness since a geometry which is known for unstable crack growth in brittle materials was used. Another way to address this problem is changing the notch type from through to chevron notch. Chevron notches have been used for fatigue pre-cracking of ceramics because they do not cause sporadic crack extension [1]. This notch geometry has also been successfully used for stable crack growth in single cantilever beam [84,85,108,110], but milling the notch requires great expertise and results are often difficult to interpret.

Another approach to optimise small scale fracture experiments is the use stable crack growth geometries. Such geometries where crack driving force reduces with crack extension are already extensively used for macroscale experiments [1,2]. Thus, some micron scale geometries have adapted the same principle to control crack for small volume experiments. Stability of a crack in these geometries is expected to promote the growth of a natural crack from FIB-milled notched with final fracture occurring in regions beyond the notch [208]. Clamped [93,95,119,209] and double cantilever beams [97–99] are two geometries which have been used for micro fracture experiments till date. Although, both geometries promote stable crack growth beyond the FIB-affected zone, experimental errors and low success rates have limited use of these geometries. For instance, residual stresses, edge milled notches and lack of analytical formulation are prevailing limitations of clamped beam experiments [33,94]. While, the double cantilever beam is prone to misalignments [97] arising from multiple sources which can either change the loading condition

at the tip or cause unstable failure in some tests [33]. Hence, the quest for stable crack growth geometries continues.

In the search for alternative geometries, factors to consider in order to improve on existing ones includes: simplicity (maybe similar to single cantilever beam), high success rate, reduced sources of experimental errors and most importantly stable crack growth. A novel geometry for the evaluation of fracture toughness at small length scales is introduced in this chapter. This geometry called single cantilever delamination geometry is first applied to a bimaterial system. A hard coating–substrate interface is first tested with the geometry where an indenter applies load to a freestanding cantilever attached to a support substrate structure and a notch is introduced between the two parts to cause delamination between two parts in mode I fracture.

The findings presented in this chapter have been peer-reviewed and published in [208] .

5.1.1 Validation of single cantilever delamination (SCD) geometry

The first step of this investigation was using finite element method (FEM) to understand the crack driving in the geometry (Figure 5.1). This preliminary FEM calculation was done using the commercially available software ABAQUS/CAE 2022, Dassault Systems, France). A two dimensional isotropic elastic model was employed for this purpose where a seam crack is placed in-between a partition which has different modulus on each side. Following existing procedures for static crack analysis [210], crack driving force was obtained from the optimized model. Then parametric studies were carried out to arrive at dimensions where stable crack growth is observed in the geometry. Details on the simulation of the model will be discussed in the next chapter.

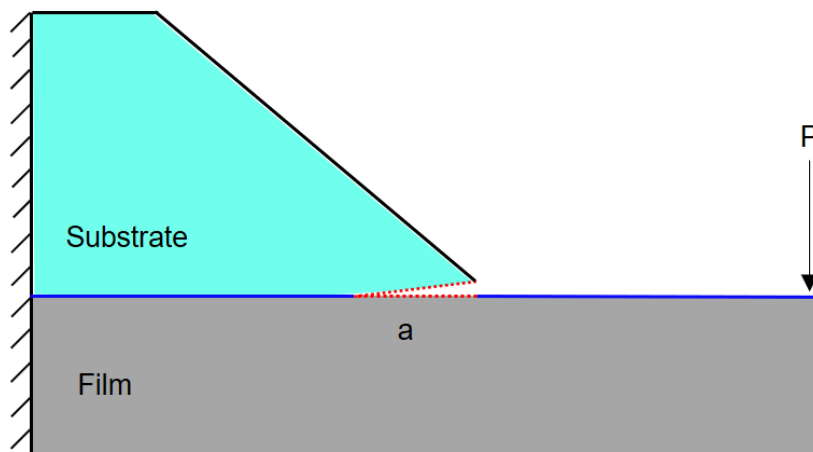


Figure 5.1: Sketch of the SCD geometry showing the crack length a lying on the interface (blue line) between the substrate and film, adapted from [208].

After dimension optimization, the crack driving force of the SCD geometry was calculated for models where the film modulus was varied by a factor of 3 with respect to the substrate. The results (Figure 5.2) show that the energy release rate increases with the crack length for all film moduli calculated until a critical point is reached where the crack driving force starts to decrease. This implies that there is an initial region of instability in the geometry beyond which the crack becomes stable in the geometry due to increased cantilever compliance. This is similar to what is observed

in other stable crack growth geometries under displacement control [1,96]. In the following experimental validation, samples were fabricated with notch length within the dashed window where stable crack growth is expected.

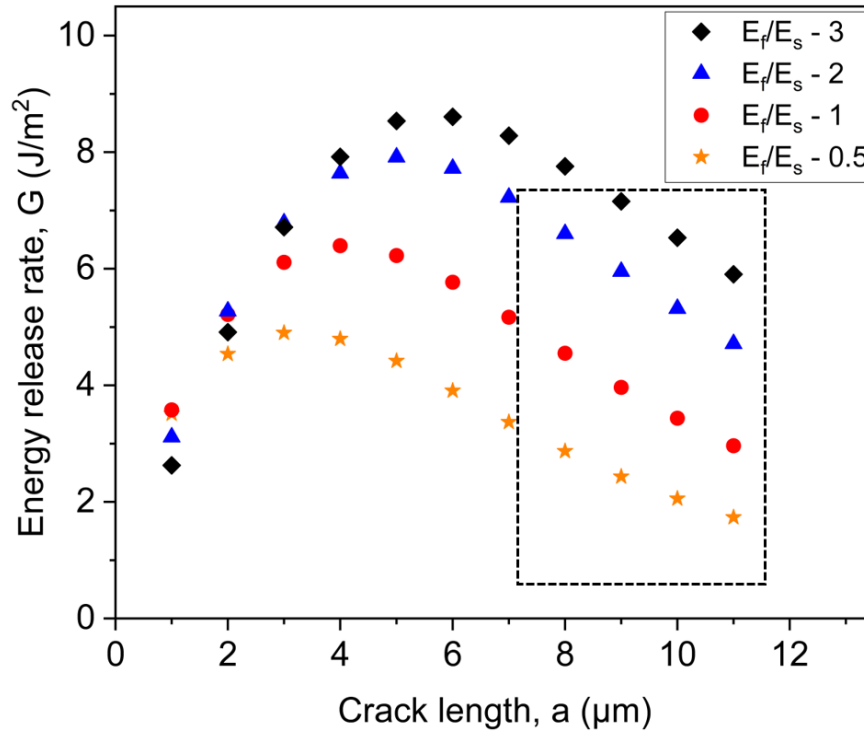


Figure 5.2: Crack driving force in SCD as a function of crack length; experimental window shown with dashed rectangle, reprinted from [208].

5.2 Experimental procedure

5.2.1 Material

The coating-substrate interface system used for the first SCD experiments comprised of a multicomponent carbide film on a (100) silicon substrate. A magnetron sputtering chamber with base pressure $< 1 \times 10^{-5}$ was used to co-sputter an equimolar composition of $\text{Hf}_{25}\text{Nb}_{25}\text{Ta}_{25}\text{Zr}_{25}$ (Plansee Composite Materials GmbH, 99.9% purity) and pyrolytic graphite (Kurt J. Lesker[®], 99.999% purity) on the substrate. The targets were 100 mm apart and oriented at 0° (graphite) and 45° ($\text{Hf}_{25}\text{Nb}_{25}\text{Ta}_{25}\text{Zr}_{25}$) to the substrate. Unlike some other sputtering processes where interfacial reactions are prevented with a barrier layer, there was no layer between the film and substrate. During sputtering all deposition conditions were set to obtain a final thickness of $\sim 3 \mu\text{m}$. The sample was sputtered in the Materials chemistry department, RWTH Aachen University, Germany. Chemical and microstructural characterisations of the resulting (Hf-Nb-Ta-Zr)C has been measured and published by [75].

5.2.2 Cantilever preparation

5 × 5 mm sample pieces cut from a starting wafer was used for the experiments. The steps shown in Figure 5.3 were used to arrive at a micro sample with the final geometry. First, a sample piece was etched in a 30 wt.% potassium hydroxide (KOH) aqueous solution heated to a temperature of 80 °C for 1 hour to get free-standing films. After etching, the sample was rinsed in acetone and isopropanol.

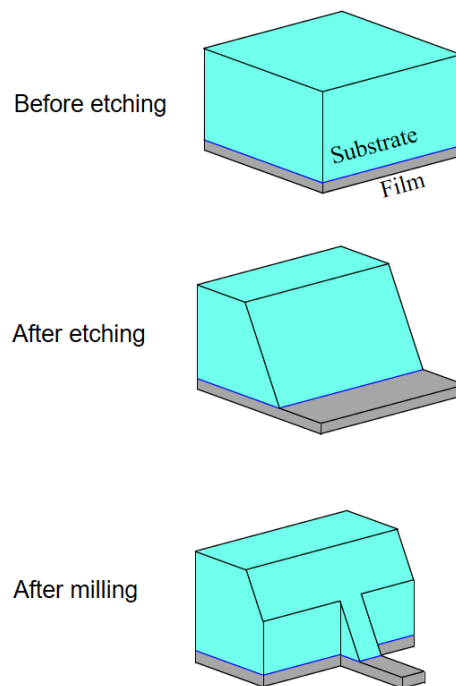


Figure 5.3: Steps to achieve the SCD geometry from cut sample piece, to etched geometry and finally milled cantilever, adapted from [208].

5.2.2.1 FIB milling cantilevers

Ga⁺ source FIB (Crossbeam 550L, Zeiss AG, Germany) was used to fabricate the cantilevers. Milling was done by on the etched surface which was aligned perpendicular to the ion source. For high throughput experiments, several cantilevers were milled along the edges of a single sample piece. Hence, it was necessary to create large trenches which would provide viewing window from the sides of the cantilevers. Large trenches were made at acceleration voltage of 30 kV and high milling currents (65 nA) and doses (50 nC/m²) leaving barriers between cuts which served as dummies to collect redeposited material (Figure 5.4a). Then the cantilevers were thinned to set dimensions keeping the same beam energy in three steps. Coarse cuts were made with a 7 nA current and dose 35 nC/m², while 1.5 nA current and dose 35 nC/m² was used for intermediate cuts, and final polishing was done with 0.7 nA current and dose 35 nC/m². SEM image of the milled cantilever showing the large trench surrounding the cantilever can be seen in Figure 5.4b. Dummy cantilevers can also be seen in the image.

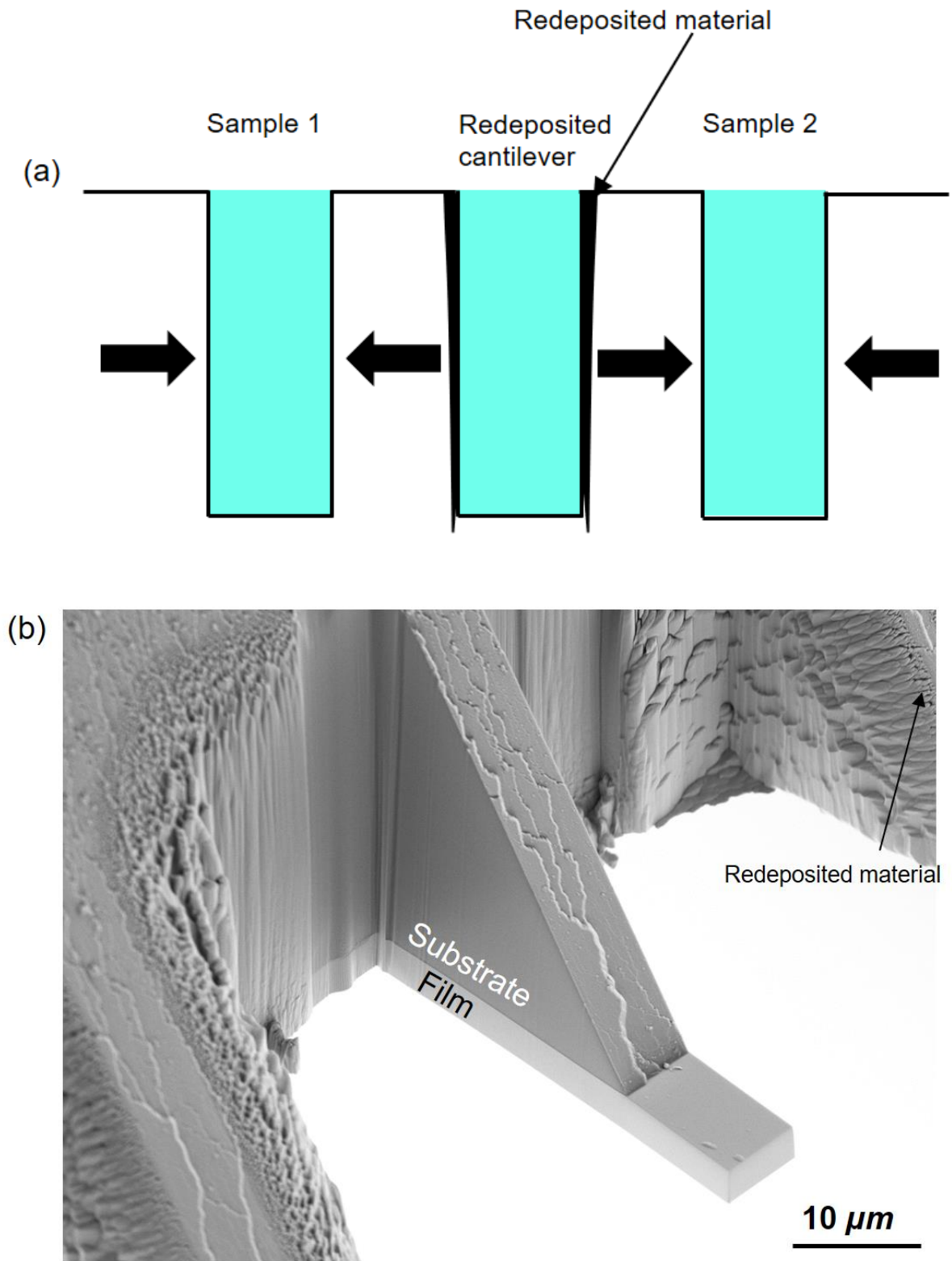


Figure 5.4: (a) Milling strategy to avoid redeposition in cantilevers and (b) SEM image showing side view of milled cantilever with film and substrate labelled.

5.2.2.2 Notches

FIB notches were introduced into the milled cantilevers by aligning the interface plane parallel to the ion source. Two notch shapes were selected for this purpose; a through notch and a chevron notch. The through notch (Figure 5.5a) runs across the width of the cantilever from point *A* to *B* and runs along the interface plane from *AB* to *CD*. Notches with radius of few nanometres was achieved using line patterns milled with 30 kV acceleration voltage, 50 pA current, 2 nC/m² dose, 1 μs dwell time which optimized exposure time and redeposition of materials. Chevron notch with an apex which serve as a point of stress concentration for easy crack nucleation was also used to create interface notches. In the SCD geometry, the apex of the chevron is placed at the top of the beam instead of the center where it is traditionally placed in other geometries for easy positioning [208]. Since this notch requires larger areas to be milled away using a two dimensional shape, higher current (50 pA) and dose (4 nC/m²) dose was used for patterning. The apex of the chevron notch lies at point *B* and the triangular ligament increases in width along *BD* and *BE* on the interface plane.

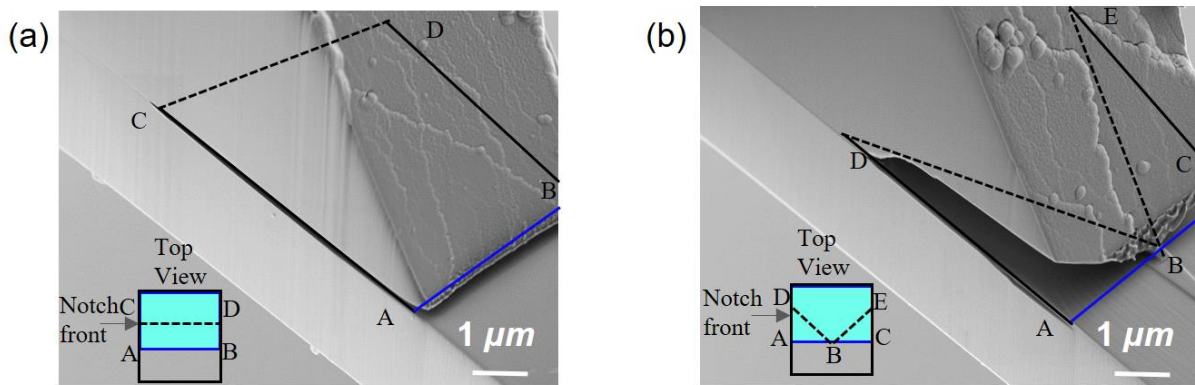


Figure 5.5: SEM image with top plane sketch of (a) through notch and (b) chevron notch, reprinted from [208].

5.2.3 Micro fracture tests

Cantilever bending experiments were performed *in situ* in an SEM (Merlin, Zeiss AG, Germany) with a PI 89NG indenter (Hysitron, Bruker, USA). The 10 μm wedge used for experiments in Chapters 3 and 4 could not be used for the tests in the SCD geometry because the opening angle of the tip (70°) are too large to approach the sample. This problem arises because of i) the thickness of the substrate and ii) the large angle of the substrate with respect to the film after etching. To circumvent this problem, an in-house wedge tip was fabricated using a combination of wet etching, femtosecond laser ablation and FIB polishing. A 300 nm diameter tungsten wire was etched by periodic dipping of the positively biased wire (AC voltage) into a 2M concentration potassium hydroxide electrolyte. Etching occurs at the electrolyte-metal interface and it results in a wire with curved tip. After etching, femtosecond laser was used to create a wedge shape by milling from the top surface and 90° orientation. Then final polishing was done with the FIB to get the final tip (Figure 5.6a).

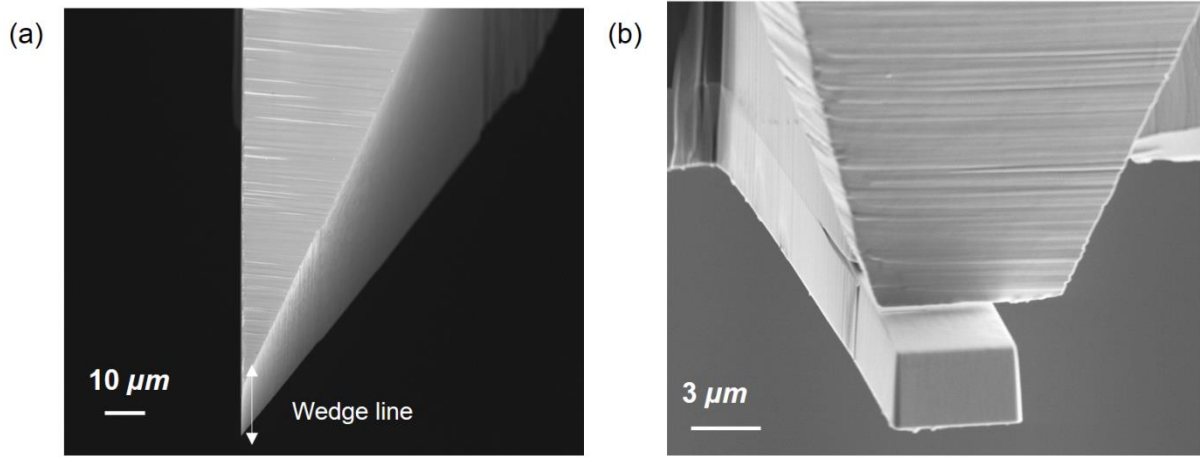


Figure 5.6: (a) Side view SEM image of custom made wedge tip and (b) front view of wedge aligned to a cantilever for *in situ* test.

This tip was then attached to the indenter and the cantilevers were aligned to tip following steps described in Section 3.24 (Figure 5.6b). Using a displacement-controlled high load transducer the cantilevers were tested a displacement rate of 10 nm/s.

5.1.1.1 Crack length estimation

During the test partial unloading was done at intervals of 300nm to monitor crack extension. The slopes of the unloading curve were also used to calculate crack length using assuming a cantilever clamped at the crack tip and applying Bernoulli theory (Eqn 5.1),

$$a^* = \left(\frac{C_M E_f B W^3}{4} \right)^{1/3} \quad (5.1)$$

where a^* stands for effective crack length which is a combination of the cantilever's load arm and the crack length, C_M is the compliance measured from the unloading slopes, E_f is the film's modulus, and B and W are the cantilever's width and thickness, respectively. Since the compliance measured from the slope would be affected by external factors from the machine, the macro specimen sample and the tip, the raw data needs to be corrected before data analysis. However, traditional correction methods using fused silica would not be suitable because of the different sample mounting and custom-made tip. Two methods were used for correcting the measured compliance. In the first method, the frame compliance (all external contributions) C_{F-C} was calculated by subtracting the compliance of the beam (C_B) (Eqn 5.2) from the compliance of the initial loading slope (C_0). Additionally, the frame compliance C_{F-M} was directly measured from the specimen in an area behind the cantilever (Figure 5.7). Then, frame compliance from both methods was subtracted from the measured compliance C_M obtained from the unloading slopes using Eqn. 5.3. The corrected measured compliance (C_M^*) was then used to calculate the crack length; substituting C_M^* into Eqn. 5.1.

$$C_B = \frac{4a^{3*}}{E_f B W^3} \quad (5.2)$$

$$C_M^* = C_M - C_F, \text{ with } (C_F = C_{F-C} \text{ or } C_{F-M}) \quad (5.3)$$

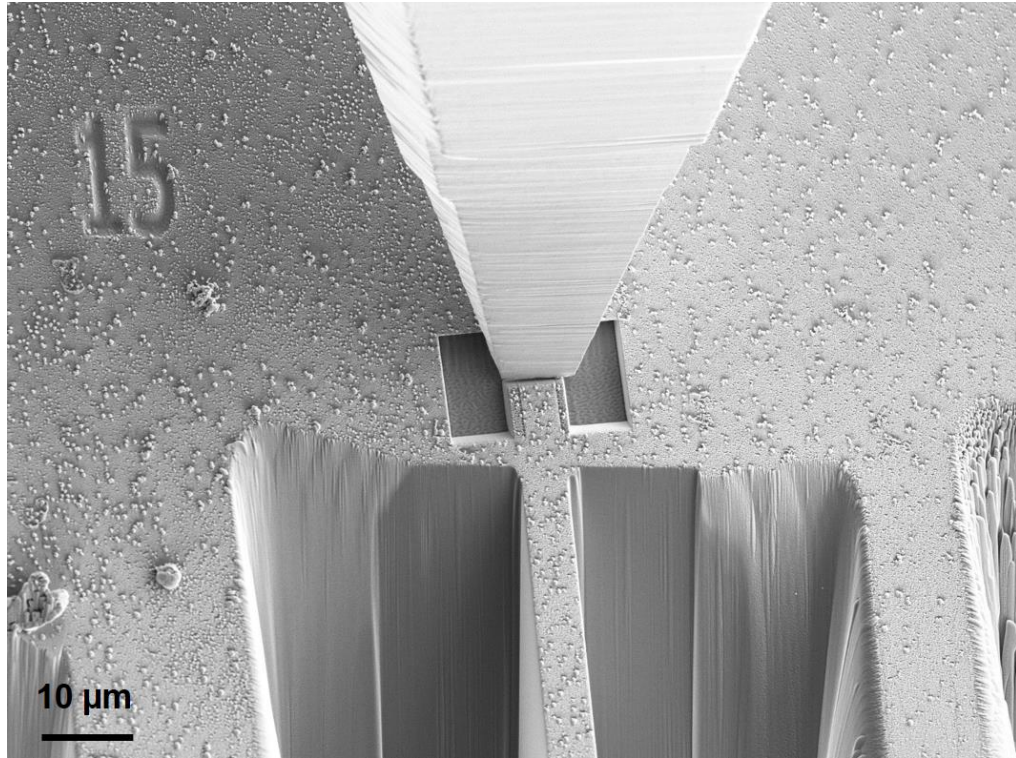


Figure 5.7: Indenter positioned to measure the compliance of the tapered specimen, reprinted from [208].

5.3 Results

5.3.1 Observation of stable crack growth

Figure 5.8a shows the load-displacement curve of a through-notched sample with partial unloading segments at 300 nm intervals. It is seen that the initial loading region sustains a maximum load of 2600 μN (point *b*) before a drop in load signifying crack growth is seen (Figure 5.8b). Between points *b* and *c*, the growing crack from the FIB notch deflects into the interface (evidence of deflection is seen around the FIB notch root in 5.8c). The deflected crack continues to extend along the interface from points *d–h*, also seen in the crack opening from the accompanying SEM image from each point (Figure 5.8d–h).

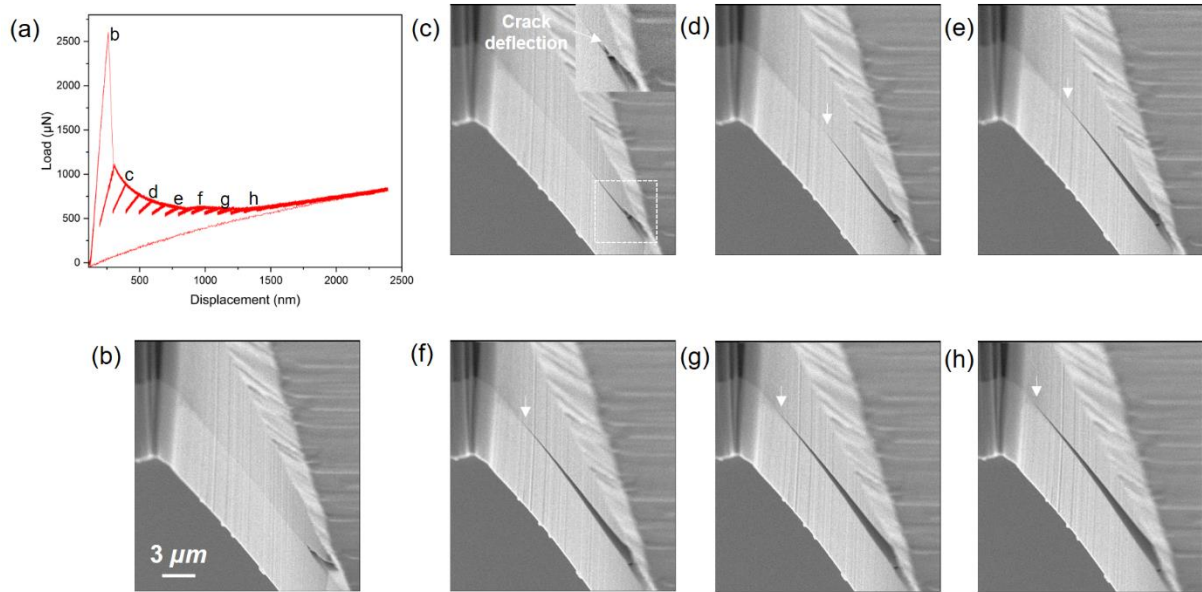


Figure 5.8: (a) Load-displacement plot of a through notched cantilever showing partial unload segments with points of different events during *in situ* test labelled and (b–h) SEM image of crack extension in the cantilever, reprinted from [208].

Similarly, the test result from a chevron-notched cantilever is presented in Figure 5.9. In this cantilever, the initial cracking event occurs at the apex (point *B*, Figure 5.5b) of the chevron where there is stress concentration. Since this point is located in the middle of the cantilever, it could not be seen during the test. However, a load drop in the load-displacement curve (Figure 5.9a and b) corresponds to this event. Once the crack starts growing, it propagates along the triangular ligament *b–c* till the end of the chevron where evidence of crack deflection (Figure 5.9c) is seen. Beyond point *c* the crack behaves like a through-thickness notch.

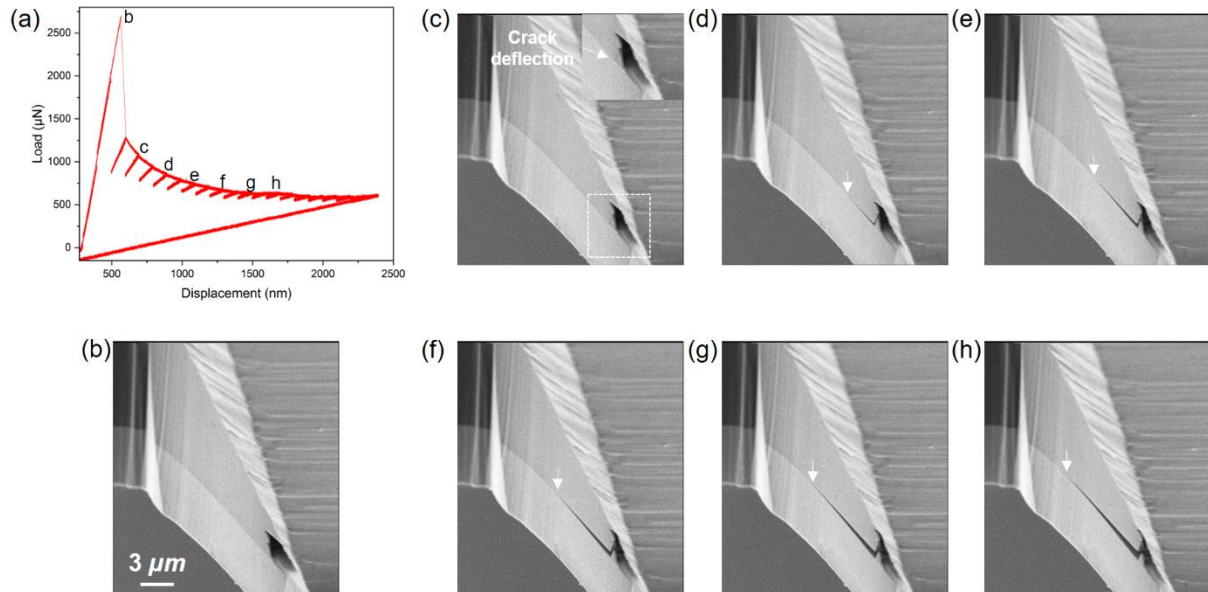


Figure 5.9: (a) Load-displacement of a chevron notched cantilever plot showing partial unload segments with points of different events during *in situ* test labelled and (b–h) SEM image of crack extension in the cantilever, reprinted from [208].

Both experiments demonstrate stable crack growth using both notches in the SCD geometry. This is evident from the absence of catastrophic failure during the tests. It signifies that the elastically stored energy in the beam is insufficient to cause instability, which increases the load-bearing capacity of the system, corroborating what was observed from the preliminary FEM calculation in Section 5.1.1. In the next section quantification of interface toughness would be discussed using the corrected crack length obtained from the unloading slope.

5.3.2 Quantitative analysis of interface toughness

Crack length measured from SEM frames (Figure 5.8 c–h) corresponding to points on the unloading slope is compared to corrected effective crack length a^* calculated using the procedure outlined in Section 5.2.3.1 and presented in Figure 5.10. It is observed that crack length increases with displacement for both measured and calculated a^* . However, the SEM measured effective crack length deviates from the calculated which could be attributed to i) the curvature of the bending beam introducing errors in SEM measurements and ii) the limitations of the cantilever theory assumptions used for the crack length calculations. This assumption which only served as an upper bound for crack length calculation, could also be responsible for the compliance correction methods being more effective at shorter lengths. Figure 5.10 does not show any clear distinction in the results from both correction methods, implying both approaches are suitable for correcting the influence of external compliances. Thus, C_{F-C} is used correct the influence to external compliances in all the cantilevers.

In the next step, the critical energy release rate (G_c) for crack extension is calculated for one test using the area method [211,212]. G_{c-H} (G_c of the interface) is calculated by dividing the energy loss due to crack extension by the crack area (Eqn 5.4). The energy loss is calculate from the area

between the load-unloading curve and the crack area is calculated using effective crack length (Figure 5.10),

$$G_{c_H} = \frac{\Delta H}{B\Delta a^*} \quad (5.4)$$

where ΔH is the energy for crack growth, B is width of the cantilever, and Δa is the crack extension. G_{c_H} as a function of crack extension is presented in Figure 5.11 for a through notched cantilever. This result show that the critical energy release rate remains relatively constant with crack growth, however some scatter is observed in the result.

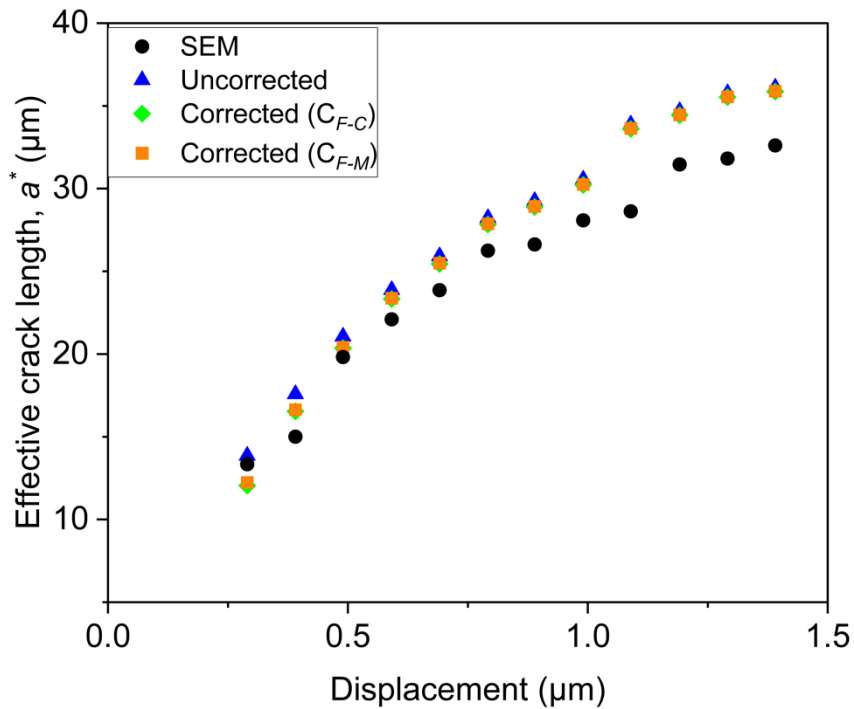


Figure 5.10: Effective crack length measured from SEM, calculated from unloading slope and compliance corrected, adapted from [208].

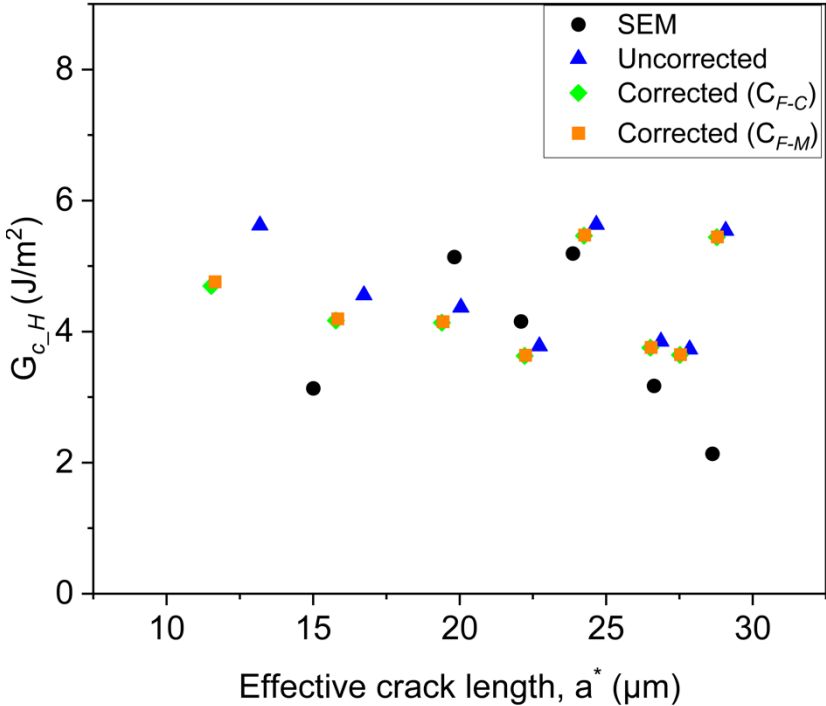


Figure 5.11: Critical energy release rate plotted as a function of effective crack length of interface, reprinted from [208].

Finally, the $G_{c,H}$ of all the cantilevers tested is shown (Figure 5.12a) to see the average toughness of the interface. The trend shows that the interface toughness remains relatively constant at long crack lengths when the crack front has grown beyond the FIB affect zone. The Interface toughness values range from 3.0 and 5.5 J/m^2 for the samples with through notch, while values between 3.3 and 9 J/m^2 are seen for the chevron notched sample. The huge scatter in the toughness values can be attributed to inaccuracies in crack length estimation. In Figure 5.12b, it is seen that the energy loss during crack growth is virtually the same for all cantilevers irrespective of notch geometry. This suggest that crack stability in the SCD geometry is not sensitive to notch type.

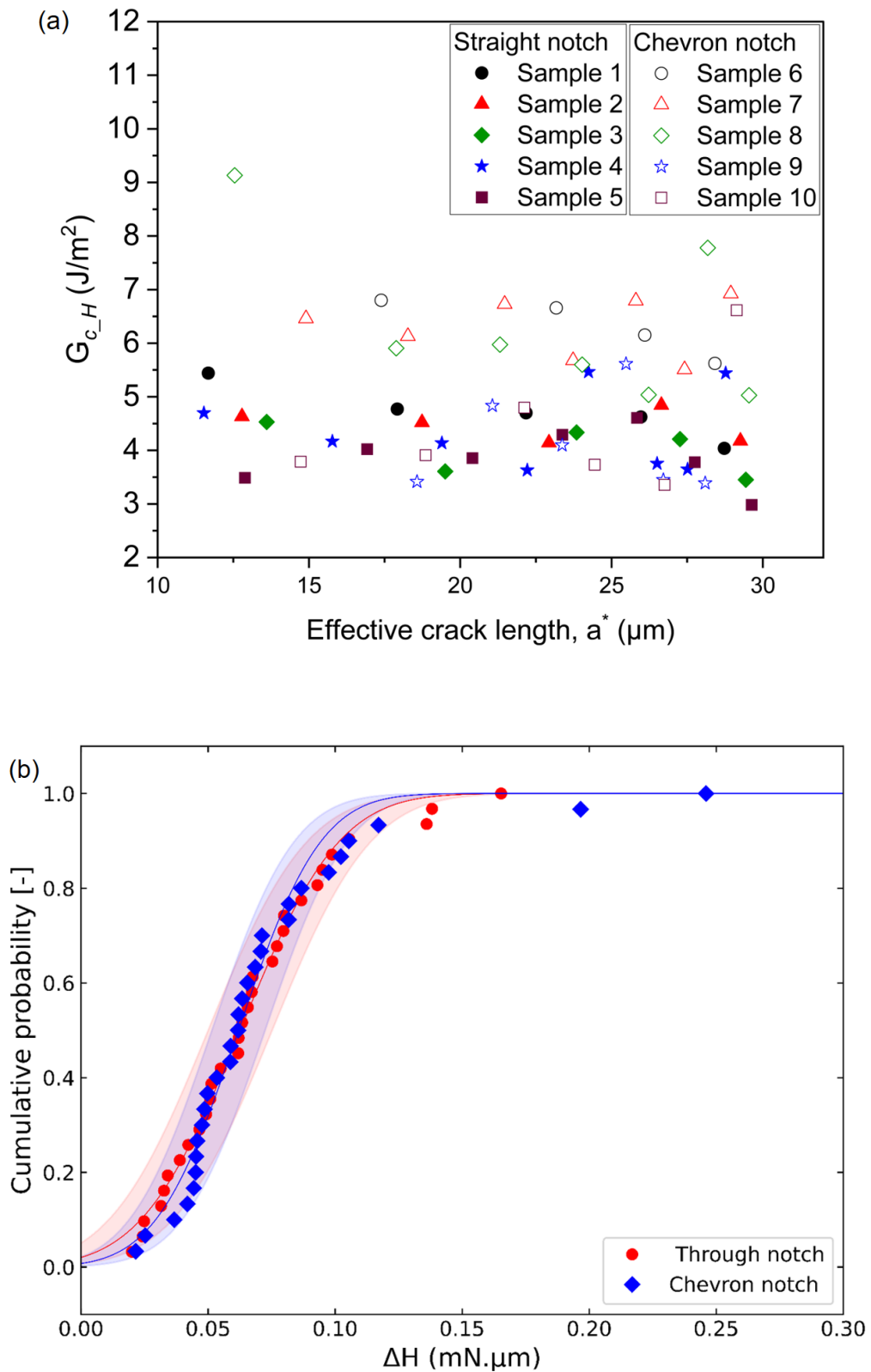


Figure 5.12: (a) Interface toughness, G_{c_H} for all cantilevers (reprinted from [208]) and (b) cumulative distribution of energy loss (ΔH) during crack growth for all cantilevers with different notch shape.

5.4 Discussion

5.4.1 Stable crack growth

A crack will propagate in an unstable manner in materials with flat resistant curve, R , because the crack driving force increases with crack length [1,213]. Modification of the testing setup using displacement-controlled experiments can lead to decreasing crack driving force, G , making stable crack growth experiments possible even in brittle materials [2,213]. Therefore, there is a growing interest in developing stable crack growth geometries for small scale experiments. In stable crack growth experiments, influences FIB artefacts on fracture toughness are minimised because catastrophic failure does not occur at the FIB milled notch. Also, such experiments are useful to monitor delamination behaviour of specific interfaces [214]. Crack extension monitoring is made possible in stable testing configurations since analysis is not limited to a single fracture toughness value. In the SCD geometry, stability is confirmed in two ways. First, the FEM calculations showed reducing crack driving force with long cracks satisfying the conditions for stable crack growth. In addition, the experimental results corroborate the calculations by the absence of catastrophic failure at the FIB notch after a maximum load and the deflection of a crack into the interface.

5.4.2 Crack deflection at interface

The SCD geometry was first tested using a hard coating–substrate interface. In interfaces, elastic mismatch between the bulk materials causes mixed mode loading at crack tip regardless of the nature of the far-field stresses [215–217]. Therefore, crack propagation in materials with interfaces depends on the mixed mode loading, the interface chemistry and interface morphology [218–220]. Any of this factors can dominate cracking in layered materials, for instance, interface penetration will dominate crack extension in a system where the interface between two bulk materials is weak [220–222]. In this case, the driving force for crack growth along the interface (G_i) is higher than the driving force for crack deflection into the bulk (G_b). Additionally, G_i is greater than the interface's resistance to crack growth (R_i). hence, a near-interface crack impinging the interface will grow along the interface to minimise the system's energy. This phenomenon describes what is observed in the SCD geometry during testing. In the absence of catastrophic failure, first, a natural crack is nucleated ahead of the true FIB milled notch front $C^*–D^*$ (Figure 5.13a) and this crack grows parallel to the interface plane before deflecting into the interface at $C–D$ (Figure 5.13b) where the influence of FIB ends. At the deflection point, the crack on the interface is sharp enough for accurate evaluation of fracture toughness [223], and free of notch artefacts like residual stresses from ion implantation, and chemical interactions. Uniform crack front along the width of the cantilever after deflection (in the absence of tunnelling effects), also reduces errors associated using through notches in micro fracture experiments.

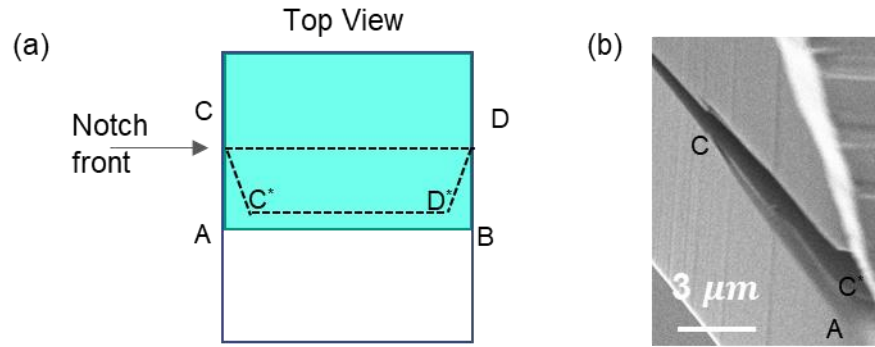


Figure 5.13: (a) sketch of the top plane of straight notch showing the actual notch (AC*D*B) and (b) SEM image showing crack propagation along the assumed plane notch before deflection, reprinted from [208]

5.4.3 Interface toughness

The interface toughness calculated using results measured from the SCD geometry plateaus at distances away from the FIB milled notch as a result of growth of a natural crack. Thus, it can be implied that the measured toughness is truly representative of interface of interest. To corroborate this assertion, the interface toughness has to be compared to expected values of (Hf-Nb-Ta-Zr)C film / silicon interface used as a model system. For this purpose, the interface toughness (Figure 5.12a) is compared to the fracture energy of the bulk materials, since the toughness of this interface have not been reported in literature. Fracture energies of the bulk serves as upper bounds because the crack path during experiments suggests that the interface offers the weakest resistance to a moving crack.

Therefore, G_{c_H} which plateaued at 3–7 J/m² is first compared to the fracture energy of transition metal carbides which is reportedly between 3–12 J/m² for different crystallographic planes [224]. Similarly, G_{c_H} is compared to fracture energies of different crystallographic planes of the silicon substrate which has energies ranging from 2.2–5.0 J/m² for different planes [225–228] derived from experiments and theoretical calculations (density functional theory). The fracture energy of the Si (100) (2.8–4.78 J/m²) [228] plane is of utmost interest because it oriented favourably for deflection with respect the loading direction. Although, the fracture energy of the substrate seems to be at the bounds of the interface toughness, it is suggested that the absence of crack branching into the substrate could be geometrical constraints of the SCD geometry. Another possible reason is the presence of a native oxide layer on the surface of silicon substrate before deposition [229–231] with fracture energies between 6.2–9 J/m²[83,232]. These comparisons justify crack deflection into the interface in the SCD geometry.

5.5 Conclusion

A novel SCD geometry was introduced and tested for fracture investigations of small volumes. FEM and experimental methods were independently used to verify the suitability of the SCD beam as a geometry for stable crack propagation. The results show that as a crack gets longer the driving force for propagation reduced. In the experiments, the geometry enabled the growth of a natural crack from FIB milled notches of different types circumventing the influence of notch artefacts.

5. Novel single cantilever delamination geometry for fracture toughness measurements

Interface toughness of a (Hf-Nb-Ta-Zr)C–silicon system calculated using the SCD geometry was between 3–7 J/m² which is expected for the interface considering the fracture energies of the film and substrate.

6.0 Numerical analysis of single cantilever delamination (SCD) geometry

Chapter 6 is intended to be submitted as journal publication.

The subsequent researchers have contributed to chapter 6. A detailed description of the individual contributions can be found in the appendix.

E. Okotete¹, S. Lee¹, S. Brinckmann², C. Kirchlechner¹.

¹Institute for Applied Materials, Mechanics of Materials and Interfaces, Karlsruhe Institute of Technology

²Institute for Energy and Climate Research, Forschungszentrum Jülich, 52425 Jülich

6.1 Introduction

The SCD geometry (Figure 6.1) offers the opportunity to perform stable crack growth experiments at the micron scale thereby circumventing FIB artefacts which have been an open topic in the micro fracture community. In chapter 5, a detailed analysis showed that crack growth in this geometry is sufficiently stable to accommodate crack deflection and growth. This initial investigation was carried out using a film-substrate system with a weak interface. Since the interface was weak, a near-interface starting crack had a high driving force to deflect and grow along the interface. This material served as a perfect starting point to demonstrate stability of crack growth when using the geometry in the presence of an existing notch.

Rising questions are its usage scope, and possible application to other single phase or multi-layered material systems. Attempting to answer this question will require a deeper understanding of the SCD geometry and critical parameters that influence the crack driving force. An experimental study of this magnitude will demand thousands of FIB milled samples to give statistically verified results. FEM calculations have been historically used in the field of fracture mechanics to understand geometry contributions to stress intensity factors for different geometries [233–236]. At the micron scale FEM calculations have been used to calculate geometry factor [83], stress intensity at material bridges [7], and influence of material anisotropy on fracture toughness [93] for single cantilever beam geometries. In the clamped beam geometry FEM is used to extract the stress intensity factor [94], while a material dependent coefficient for calculating the fracture toughness in pillar splitting geometry is extracted from FEM [100].

Similarly, this chapter intends to utilize FEM simulations to provide a better understanding of the geometry and ultimately provide guidelines for future use of the geometry in the micro fracture community. This will be achieved by first isolating the individual contributions of specific geometry dimensions on the stress intensity factor for the SCD geometry. Based on this result, the conditions for crack nucleation and crack propagation along the interface will be recommended.

Finally, an attempt will be made to obtain analytical expression which could be used to calculate the fracture toughness using the SCD geometry.

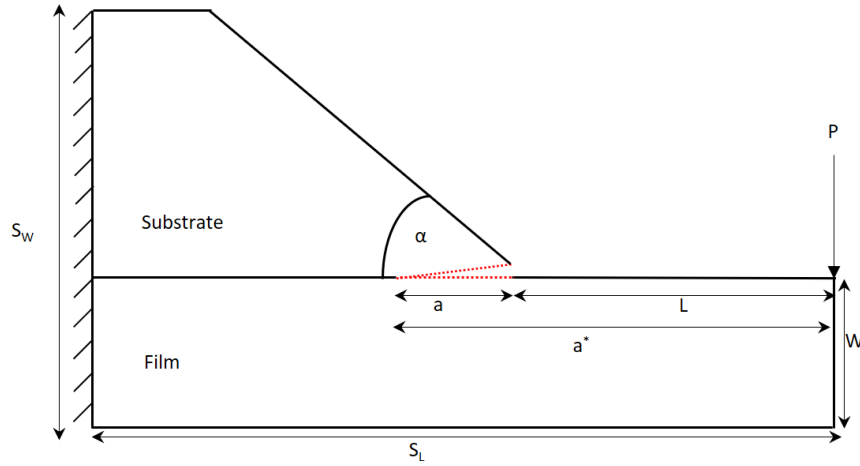


Figure 6.1: Schematic representation of the single cantilever beam geometry with an amplified crack-opening presented in the previous chapter showing applied boundary conditions for FEM simulation and the designations on the geometry are defined as follows; W —beam thickness, S_w —sample thickness, S_L —sample length, P —applied load, L —free cantilever length (distance from loading point to the substrate), a —crack length, a^* —effective crack length and α —angle between substrate and film.

6.2 FEM Model

This section used a FEM approach, which would provide the crack driving force in the SCD geometry. A contour integral FE code is available on ABAQUS/CAE 2022 (Dassault Systems, France) based on Rice's [237] J-integral for characterise crack tip conditions and its modification for analysing stress and strains at the crack [238,239] (Eqn. 6.1),

$$J = \int_{\Gamma} \left(W \, dy - T \cdot \frac{\partial u}{\partial x} \, ds \right) \quad (6.1)$$

where Γ represents a contour going around a crack tip in a counter clockwise manner from the lower to the upper surface (Figure 6.2), W is the strain energy density, T is a traction vector on the outward normal along the contour boundary, u is the displacement vector and s is the arc length.

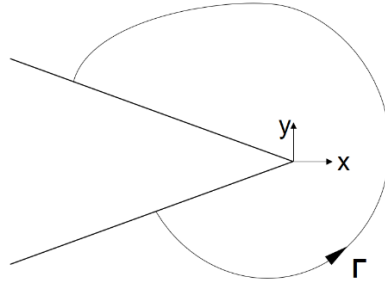


Figure 6.2: A crack with coordinates x and y describing the deformation field at the crack tip, and Γ showing the contour used for line integral evaluation.

The SCD geometry was modelled as a two-dimensional (2D) single-part with partitions used to separate two sections; a cantilever and substrate section. This type of model is used because the deformation state in the geometry can be described as a generalized 2D problem.

An elastic isotropic material model was used to assign material properties corresponding to the film and substrate to both sections of the geometry because actual material properties and grain orientation are unknown. Hence, the results are first order estimates. Thereafter, a seam (a part of the model which can open or close during analysis) is created in the chosen region of the interface between the two sections to serve as crack [240]. The contour integral crack type is assigned to the seam to specify the type of crack analysis required for the calculations, then a crack tip and crack extension direction are defined on the model. Because the stress distribution is singular at the crack tip according to elastic fracture mechanics [241], 4-node elements are degenerated using a collapsed single node with a mid-side node parameter of 0.25. Boundary conditions were applied to the model by specifying the displacement-controlled loading. In the next step, the geometry was meshed using 2nd order quadrilateral plane strain elements with focused region biased towards using circles partitioned around the crack tip (Figure 6.4). A mesh convergence study was carried out till the results were independent of element size and the final mesh had crack tip elements subtended at $\sim 11^\circ$. Afterwards, the output for the crack driving force was requested from 10 hierarchical integrals at the crack around the crack tip to check for convergence and path independence of the J-integral.

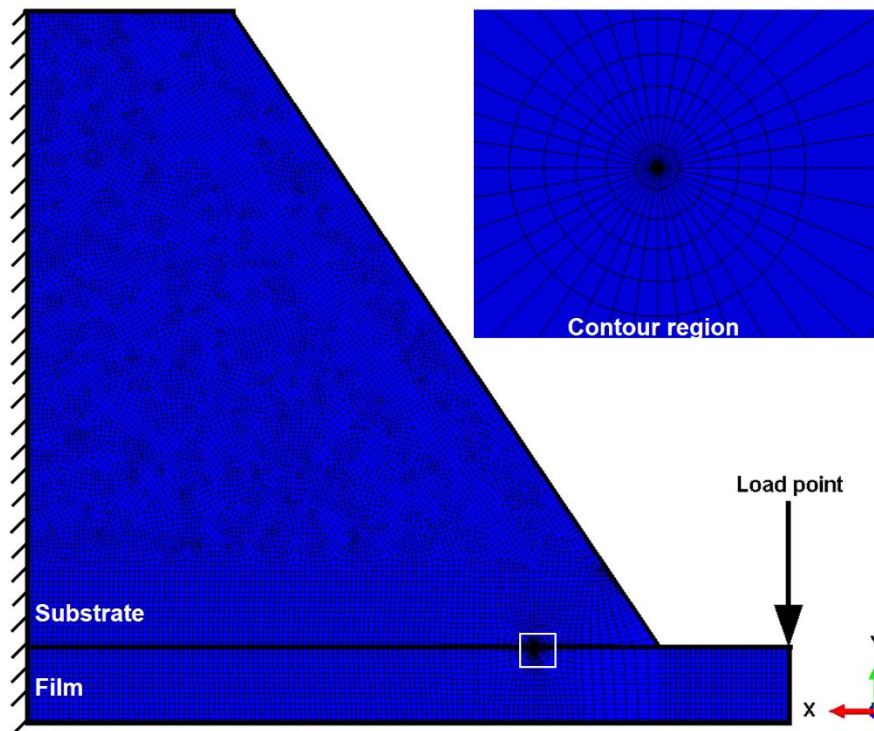


Figure 6.3: Meshed geometry with focused mesh at the crack tip.

To account for changing stress states along the crack front from the centre to the surface, data was extracted from models with plane stress and plane strain elements. Both calculations showed a 4% variation in the J-integral data. Additionally, a three-dimensional (3D) model was created to compare the results with those from a 2D plane strain model and the comparison showed no significant difference. Hence, the remainder of calculations in this chapter were made using a 2D model to save computational time.

After the preliminaries, parametric studies were carried to determine the critical geometry and elastic parameters which would influence the fracture response of a crack in the SCD geometry. This was achieved by generating and submitting input files via Abaqus python script. After analysis, the result file is opened and the critical outputs from the contour and the reaction forces are appended to an external file using python code.

6.2.1 Modelling experimental data

To simulate the precise geometry of the experiments and to compare to the experiments, a corresponding model as described above was used. In this model, the dimensions from the experiment, corrected crack length, and the max displacement before the cyclic unloading (see Figure 5.8a) are used to automatically generate input files for the analysis.

6.3 Results

6.3.1 Stress distribution at the crack tip

Figure 6.4 illustrates the same stress-tensor distribution using two model views. One view on the stress distribution focuses on crack extension pointing along the interface, this view shows the crack driving stress for delaminating crack growth (Figure 6.4a). In contrast, the other view depicts the crack extension direction towards the film (Figure 6.4b), which calculates the crack driving stress for fracture of the film. Both views arise from the same simulation, hence the same geometry and material properties. The elastic properties of silicon are assigned to the substrate, while the film is assigned properties typical of hard coatings.

According to Figure. 6.4, the maximum stress is found at the crack tip in both models. The high stresses at the crack tip comes from the singularity at the tip. For the delaminating crack, a butterfly-shaped stress pattern appears with its symmetry axis at the interface. In the other view, one butterfly-half shape appears in the film. The driving force for a crack in both directions depends on the geometry and material constants. The next sections will present calculations that demonstrate the roles of some of the geometry parameters on the stress intensity factor for crack initiation and stability of a crack in the SCD beam.

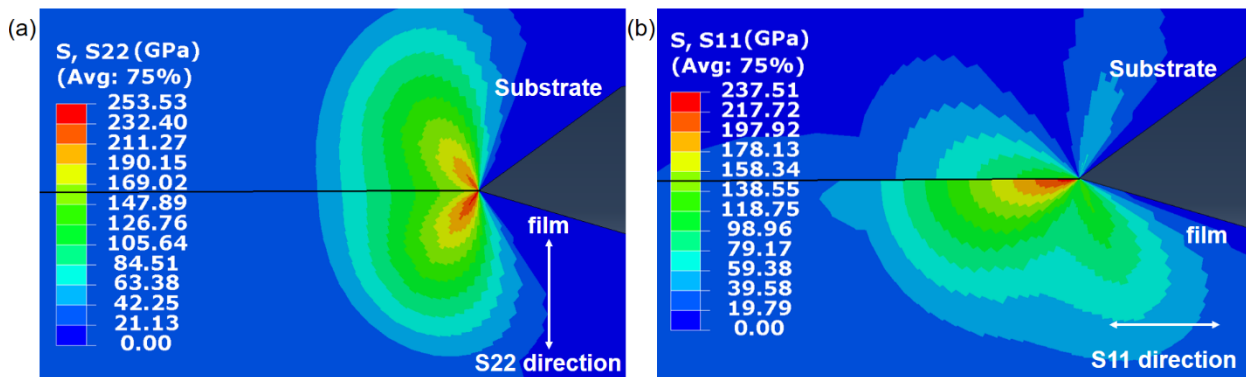


Figure 6.4: Stress distribution profile for a crack extending along the interface (a) and (b) perpendicular to the interface.

6.3.2 Stress intensity analysis of the SCD geometry

In this sections we study the deformation of crack growth is systems that consist of hard coatings and a silicon substrate since Si is the most used substrate for MEM related applications. The hard coating properties were varied within the scope of typical parameters.

6.3.2.1 Cantilever length and crack length

2D plots of the stress intensity factor as a function of the crack length (a) and the freestanding cantilever length (L) for identical geometries are shown in Figure 6.5a and b for a model with $W = 3 \mu\text{m}$, and $\alpha = 45^\circ$, and elastic properties $E_f = 400 \text{ GPa}$, $E_s = 163 \text{ GPa}$, $\nu_f = 0.2$, and $\nu_s = 0.22$. A displacement of $0.3 \mu\text{m}$ is applied to each cantilever simulated. The directions of the crack in this figure correspond to the ones in Figure 6.4a and b: (6.5a) for a crack extension along the interface

(K_{I_int}) and (6.5b) crack extension of the film (K_{I_film}). In Figure 6.5a, it can be seen that the stress intensity for the nucleation of an interface crack is highest when L and a are short (a^* less than 5 μm) attributed to the high stiffness of the short cantilever. At similar L and a , K_{I_film} for cohesive crack growth of the film is lower than the delaminating K_{I_int} suggesting that an interface crack will nucleate and grow before fracture of the coating at short effective crack length (short a and L). After crack nucleation, it is seen that the crack driving force reduces as the crack grows; this driving force reduction was already presented in the geometry validation section (see previous chapter (Figure 5.2)), which signifies the crack growth stability when using this geometry. If the crack is supposed to grow along the interface, the driving force relationship has to remain $K_{I_int} > K_{I_film}$. However, this relationship could change with increasing crack length changes as the crack grows and K_{I_film} decreases slower than K_{I_int} . At one specific crack length, a growing crack has a high chance of deflecting into the film because that will be the direction of highest driving force.

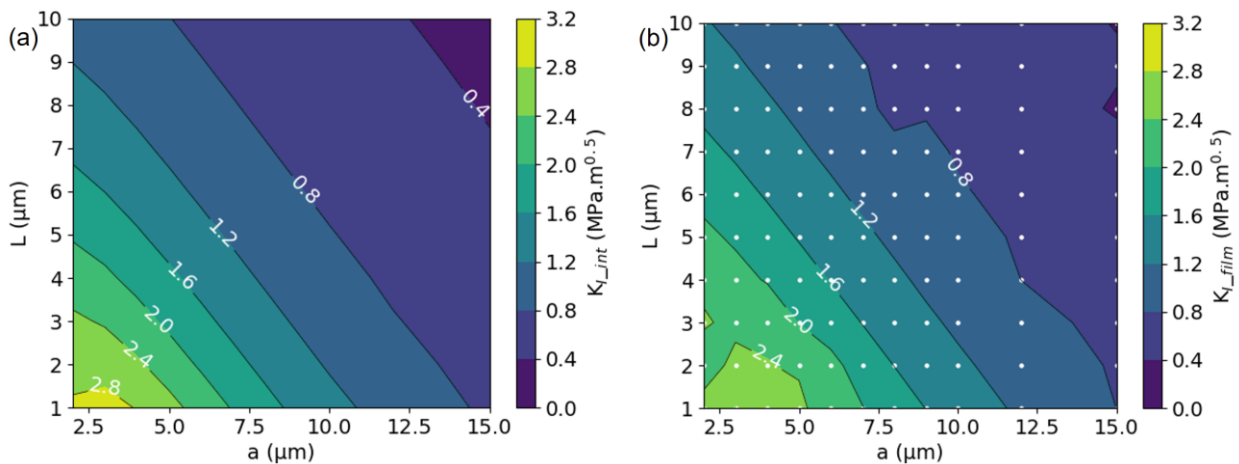


Figure 6.5: Influence of cantilever and crack length on (a) stress intensity of interface crack and (b) stress intensity of film fracture. Figure (b) shows also the individual simulation parameters that were used to create the contour diagram.

6.3.2.2 Substrate angle and beam thickness

The substrate angle and beam thickness is varied while using $L = 2 \mu\text{m}$ and $a = 3 \mu\text{m}$, which are parameters from the region of high interface stress intensity factor. The dependence of cracking driving force on substrate angle (angle between the film and substrate, α) and film thickness (W) is shown in Figure 6.6a and b. It can be observed from both plots that the stress intensity factor increases with increasing α and W , suggesting that larger angles and thicker films promote the nucleation of a crack in any direction. For very thin films ($< 1 \mu\text{m}$), the substrate angle does not really change the crack driving force and $K_{I_film} > K_{I_int}$. Here, film fracture will dominate the failure process ahead of film delamination for such films. However, as the film thickness increases the substrate angle begins to contribute to the crack driving force in the system. Figure 6.6b shows that there is a change in the trend for the stress intensity factor at film thickness greater than 3.5 μm . In this region, crack branching into the film is less favourable at high substrate angles. As the film thickness increases further, the driving force for interface crack increases much more even at small substrate angles. The results imply that interface crack nucleation in the SCD geometry is supported by thick films and large substrate angles attributed to high stiffness of the cantilever and substrate. It should be noted that the substrate angles in the silicon were controlled by etching.

Therefore, it will be challenging to increase this angle beyond the limit introduced by anisotropic etching of different planes of silicon.

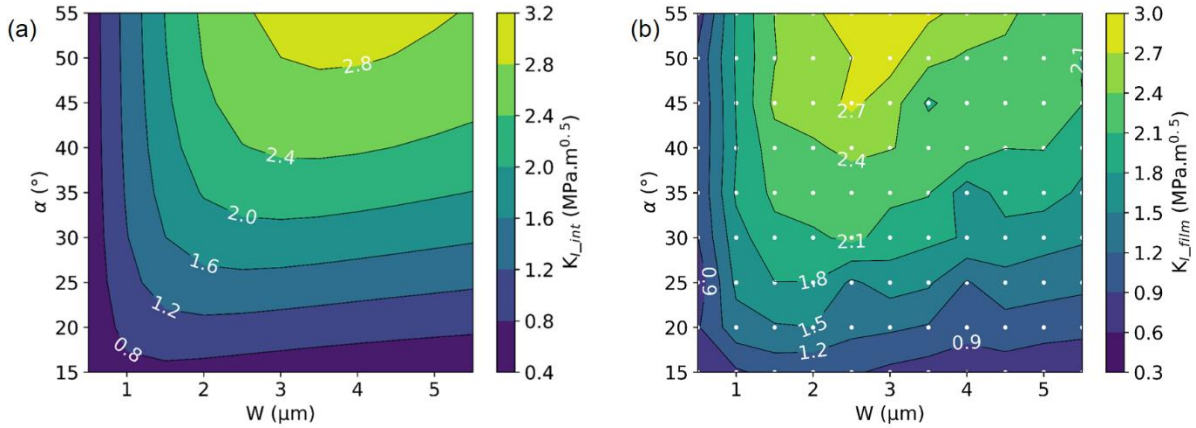


Figure 6.6: Influence of substrate angle and film thickness on the stress intensity factor of (a) interface crack and (b) film crack. Figure (b) shows also the individual simulation parameters that were used to create the contour diagram.

6.3.2.3 Elastic modulus and beam thickness

Finally, the elastic modulus and beam thickness are varied and the stress intensity factor is presented in Figure 6.7. This dataset used for the default parameters for L , a , and α from the previous two sections. It is seen here that in addition to thick films, the stress intensity factor also increases with elastic modulus of the film for both plots (Figure 6.6a and b). For films with thickness less than 3 μm, the stress intensity factor for film fracture is greater than the stress intensity factor for interface fracture ($K_{I_film} > K_{I_int}$). As the film thickness increases, stress intensity factor for film fracture also reduces, while that for interface fracture increases ($K_{I_int} > K_{I_film}$) because the cantilever becomes stiffer. K_{I_int} is maximum for film thickness between 3–4 μm and elastic modulus 500–700 GPa in the simulations conducted here. Therefore, a combination of thick films and large film modulus is needed to ensure the nucleation of interface crack.

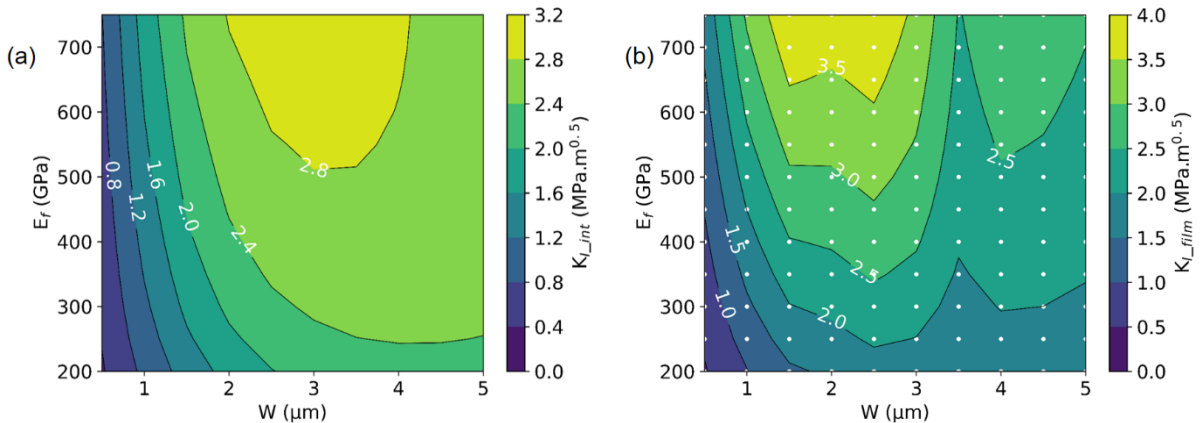


Figure 6.7: Influence of elastic modulus and film thickness on stress intensity factor of (a) interface crack and (b) film crack. Figure (b) shows also the individual simulation parameters that were used to create the contour diagram.

From all the FEM calculations, it is seen that the crack driving force for interface crack is highest at short cantilever and crack lengths, thick films, large substrate angle and large film modulus. Details about the reason for these observations will be discussed in a later section.

6.3.3 Relationship between stress intensity factor of SCB geometry and critical geometry and material parameters

Figure 6.8 shows the individual relationship between the stress intensity factor at the interface and the five parameters simulated in this chapter. To find a correlation between the crack driving force and the geometry parameters and elastic properties, the normalized stress intensity factor is plotted against the simulation data for each variable. Then a power-law fit function with an offset parameter is used to determine the relationship between the variables (Eqn. 6.2),

$$K_I/F = a(X - c)^b \quad (6.2)$$

where, a , b and c are fitting parameters, and X is the simulation parameter (W , E_F , E_S , α , L , a). The fitting parameters for each variable are presented in Table 6.1. In Figure 6.8, the fit function is seen to have a good relationship between the normalized stress intensity and both geometry and material parameters. From Figure 6.8a and b, shows that the substrate and film modulus have differing relationship with the normalized stress intensity. On one hand, the influence of the substrate modulus increases with increasing modulus (substrate gets stiffer), while the contribution of the film modulus decreases with increasing modulus (softer films). It is seen that the cantilever and crack length (Figure 6.8c and d) have a linear dependence on the normalized stress intensity, implying an increase in one of these parameters will result in a corresponding increase in geometry's response to external loading. In Figure 6.8e, the substrate angle is seen to have an increasing but low influence on the normalized stress intensity. The relationship between the film thickness and the normalized stress intensity show a reducing influence as film thickness increase. A point is reached where there is no longer a contribution of film thickness to the geometry because the thick cantilever has approached the boundary where Bernoulli beam theory can be applied.

Table 6.1: Fitting coefficients for simulated parameters.

X (parameter)	a	b	c
W	23.605	-1.5	-0.3488
α	4.090	0.09	0.20
E_F	17.0214	-0.25	~0
E_S	1.0619	0.25	~0
L	0.3050	~1	0.88
a	0.7143	0.7652	-3.915

Furthermore, the fitting functions for the simulated parameters are simplified and combined to obtain one equation which can be used to represent the relationship between the stress intensity factor and geometry and material parameters. The result is an analytical expression for K_I and is given Eqn. 6.3. Subsequently K_I calculated using Eqn. 6.3 is compared to K_I calculated from FEM.

The units used for the calculation using Eqn 6.3 are in metric system; metres, newton, and pascals for geometry dimensions, force, and modulus, respectively. It is seen from Figure 6.9 that the values from the analytical expression are in good agreement with the FEM results with exceptions for thick films (Figure 6.9) i.e thick cantilevers where the cantilever becomes too thick to considered shear-rigid. Also, the substrate angle has a small exponent and could eliminated from Eqn 6.3.

$$K_I = 95(W + 0.3488)^{-1.5} \left(\frac{3/2 a + L}{a + 33.2} \right) \left(\frac{E_S}{E_F} \right)^{0.25} ((\sin \alpha) - 0.2)^{0.09} F \quad (6.3)$$

6. Numerical analysis of single cantilever delamination (SCD) geometry

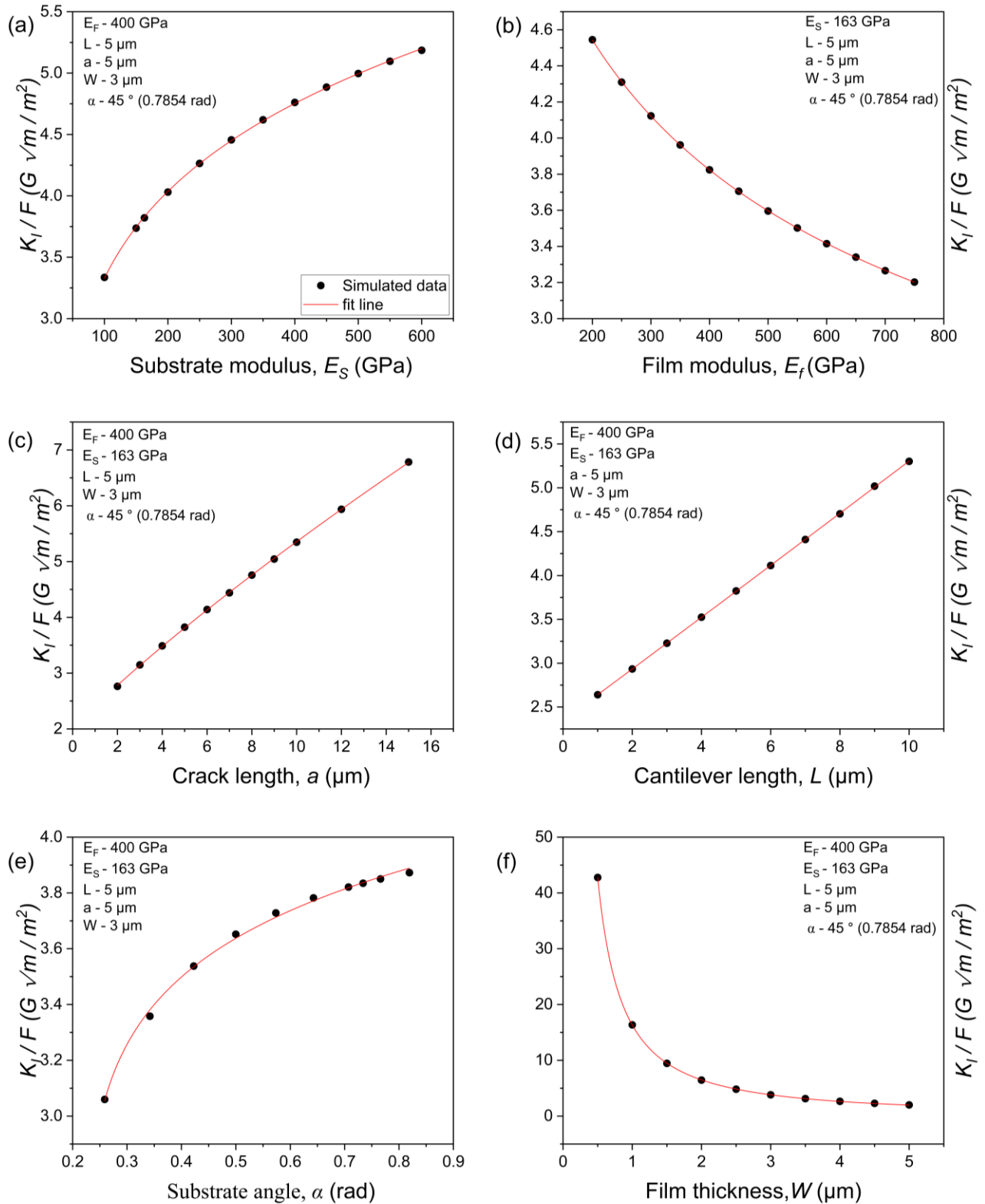


Figure 6.8: FEM simulated points and power law fit function of stress intensity factor in relation to (a) substrate modulus, (b) film modulus, (c) crack length, (d) cantilever length (e) substrate angle, and (f) film thickness.

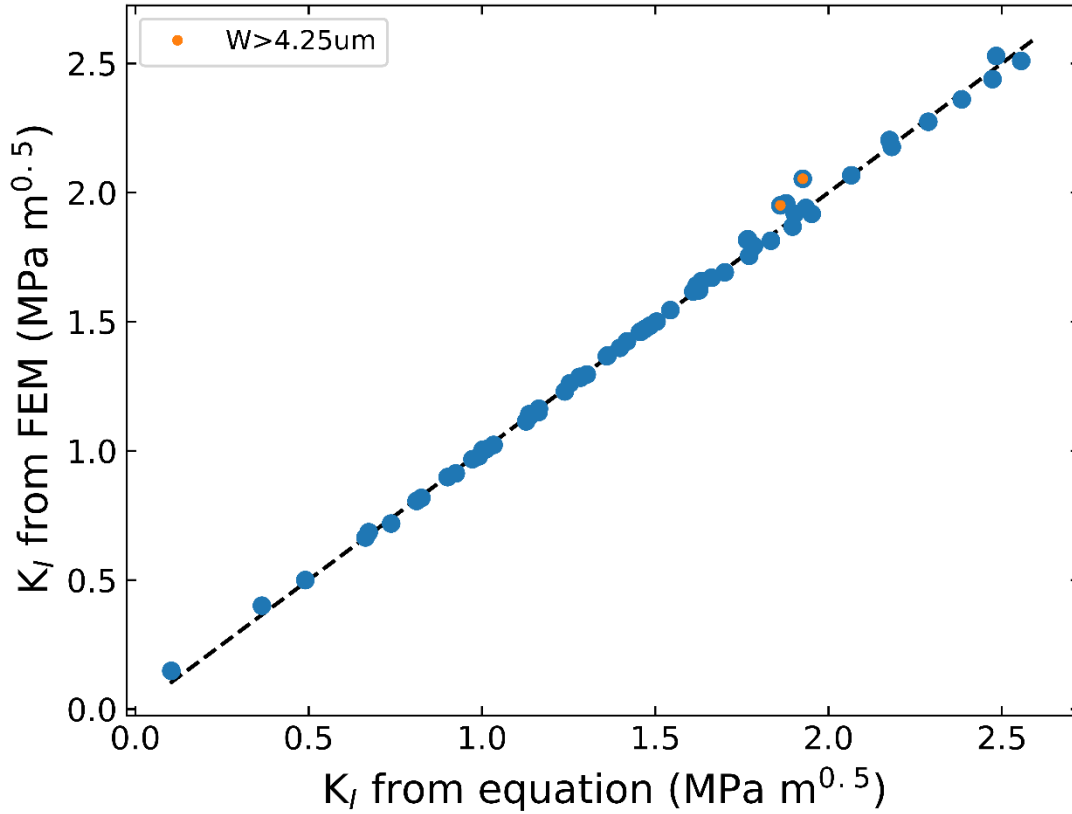


Figure 6.9: Stress intensity factor of SCD geometry calculated from FEM and analytical equation.

6.3.4 Comparing fracture toughness from experimental result and simulation calculations

Fracture toughness of the geometry calculated using the FEM models (K_{IC_FEM}) above is compared to toughness calculated from the experimental (K_{IC_Exp}) results in Chapter 5. The G_{C_H} calculated analytically from the load vs. displacement curve and corrected for external compliance (Figure 5.7) is used to calculate K_{IC_Exp} using the existing relation between K and G for linear elastic materials ($G = \frac{K^2}{E}$). Two K_{IC_Exp} is calculated for the experimental data, in the first case the film modulus (E_f) is substituted into E in the equation. Secondly, a combined modulus (film + substrate) ($E_f + E_s$) is used to calculate K_{IC_Exp} . These two values of K_{IC_Exp} act as outer bounds for the expected fracture toughness. Figure 6.10 shows that K_{IC_FEM} and the two K_{IC_Exp} are within the same range with a root mean square error of 0.31 and 0.14 for E_f and $E_f + E_s$, respectively. It is seen that at short crack lengths the influence of the substrate modulus causes the fracture toughness from the experiment to diverge from the FEM calculated toughness. However, as the crack length increases the K_{IC_Exp} calculated using both modulus converges with the FEM data.

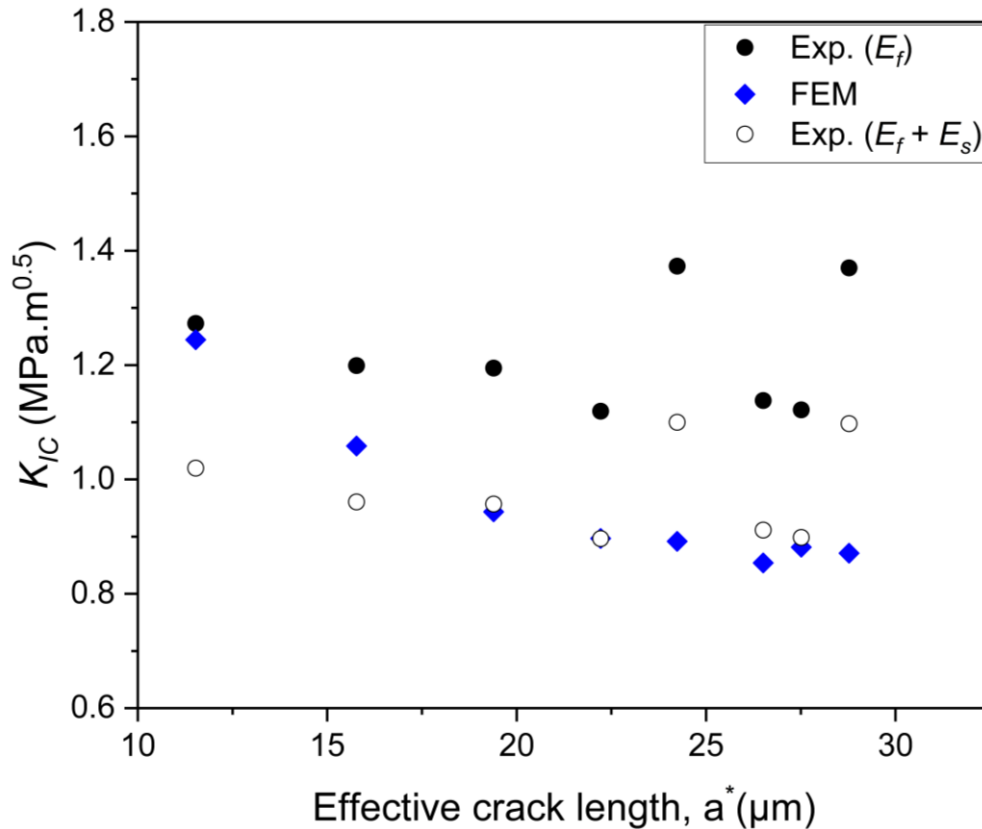


Figure 6.10: Fracture toughness from one experimental sample compared to data extracted from simulation calculations.

6.4 Discussion

6.4.1 Guidelines for geometry optimization

6.4.1.1 Crack initiation conditions

Conditions which promote interface crack nucleation in the SCD geometry depends on both the specimen dimensions as well as the material properties. For the purpose of analysis, the geometry is treated as two cantilevers joined by the interface. Emphasis is placed on the lower cantilever where the load is applied for delamination from the substrate.

Geometry and material configurations where the stress intensity factor is maximum in the direction of the interface will promote delamination crack nucleation. The calculations on the geometry show that the behaviour of the geometry can be mostly described by simple cantilever mechanics using Euler Bernoulli theory. It is well known from cantilever mechanics that reducing the length of a cantilever reduces the bending stiffness which also scales linearly with the moment of inertia. This means that load bearing capacity of short cantilever beams is increased without tensile fracture in the direction of the film. It is therefore not surprising that the stress intensity factor for a crack to extend along the interface is higher than the stress intensity factor for film fracture at small effective crack lengths (cantilever length + crack length) in section 6.3.2. A reduction in thickness of the same cantilever (loading and material parameters remain constant) would promote crack branching in the direction of the film because a reduction in the load bearing cross section

will increase the crack driving force for film fracture. Hence, an optimum cantilever thickness is needed to ensure the crack driving force for interface fracture is higher than the driving force for film fracture. Similarly, large film modulus also contributes to reducing the driving force for film fracture. From the substrate part, high substrate angles imply stiffer substrates. A combination of stiff substrate and a stiff cantilever promotes delamination ahead of crack branching.

6.4.1.2 Stable crack growth conditions

After crack nucleation at the interface, a reducing crack driving indicates that the geometry is stable enough for crack extension of the nucleated crack. Validation of the geometry in Chapter 5 (Figure 5.2) already indicated that reducing crack driving force in the geometry was responsible for stable crack growth. Using the optimised crack nucleation conditions, it is also important to see what happens to a growing crack. In Figure 6.11, it is seen that the stress intensity factor reduces as crack length increases for both crack growth directions. However, as the crack length gets longer the driving force for film fracture increases, implying that although crack growth is still stable in the geometry, crack branching could occur at longer crack lengths. This can be due to the increased compliance of the cantilever at longer crack lengths.

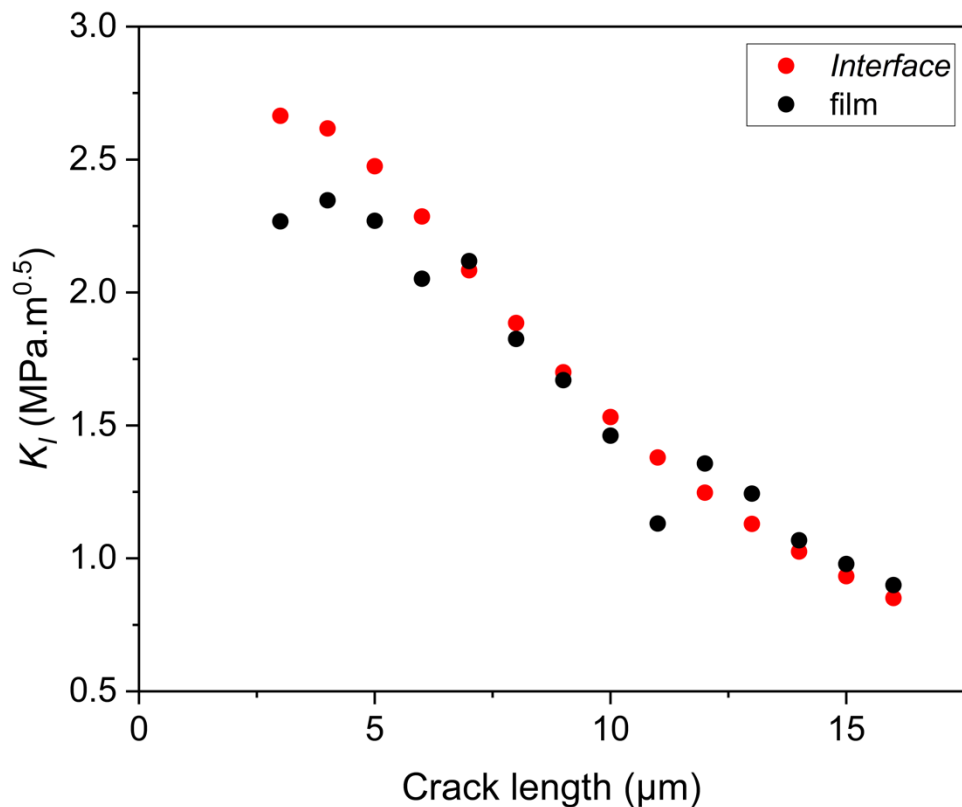


Figure 6.11: Crack driving force for interface and film propagation as a function of increasing crack length.

6.4.2 Interface fracture toughness

Using energy-based approach, the interface toughness was found to be within a range expected for crack deflection considering fracture energies of the film and substrate in Chapter 5. The fracture toughness (K_{IC}) of the interface using FEM, and data from experiments presented in Table 6.2. The data is calculated from samples with straight notch and at crack lengths beyond the FIB affected zone. The average fracture toughness is within the same range with the exception of the calculation using only the elastic modulus of the film. Hence, it is possible to analytically calculate fracture toughness of interfaces using the SCD geometry.

Table 6.2: Comparison of fracture toughness obtained by different methods

$K_{\text{interface}}$ (exp_film) MPa m ^{0.5}	$K_{\text{interface}}$ (exp_film+substrate) MPa m ^{0.5}	$K_{\text{interface}}$ (FEM) MPa m ^{0.5}	K_{film} MPa m ^{0.5}	$K_{\text{substrate}}$ (Si (100)) MPa m ^{0.5}
1.20 ± 0.07	0.96 ± 0.05	0.75 ± 0.14	2.70 [75]	0.75 -1.29 [242]

6.5 Conclusion

Simulations were used to provide guidelines for which the SCD geometry is applicable for stable crack growth experiments. For interface crack nucleation, short crack and cantilever lengths, thick films, large elastic modulus and large substrate angles are required in the geometry. However, propagation conditions may become less dependent on the geometry as compliant beams which makes the geometry stable also increase the crack driving force for film fracture. Additionally, analytical formula for calculating the fracture toughness in the geometry was derived based on FEM simulations.

7.0 Summary and outlook

7.1 Summary

The present work focuses on ways of optimizing small scale fracture experiments by reducing FIB artefacts at notches. For this purpose, three approaches were used which involve notch geometry, notching ion and sample geometry.

In the first approach, the geometry of a bridge-notched single cantilever was optimised for crack arrest. An arrested crack that grows from an FIB milled notch implies the influence of reduced damage at the notch. Therefore, the conditions for crack arrest in single crystalline silicon were found to be deep notches and thin bridges in line with FEM calculations by [7]. Shallow notches and thin bridges did not show evidence of crack arrest in the experiments, but there was no increase in fracture toughness compared to samples that showed bridge failure. On the contrary, thick bridges result in a geometry-dependent fracture toughness irrespective of notch depth. The average calculated fracture toughness for silicon using the optimised bridge and notch geometry was $1.1 \pm 0.1 \text{ MPa m}^{0.5}$.

Secondly, neon ions are used in place of gallium ions to fabricate notches in the same geometry and test material. Using this ion already eliminates some possible notch damage from liquid metal interaction due to the chemical inertness of the ion source [180]. Sharp notches were produced with this ion, however, ion implantation which precedes the formation of bubbles caused damage at the notch. Annealing the samples at $750 \text{ }^\circ\text{C}$ reduced the effect of neon-trapped bubbles on the apparent fracture toughness, and an average fracture toughness value of $1.1 \pm 0.1 \text{ MPa m}^{0.5}$ was calculated for the silicon.

The last approach does not involve modification to a notch but the introduction of an entirely new geometry. A single cantilever delamination geometry with through and chevron notches was introduced for fracture experiments. Stable crack growth was observed in the geometry when it was used to delaminate a Hf-Nb-Ta-ZrC–silicon system. A natural crack was formed from the gallium milled notch, and this crack deflected into the interface during testing. Then, the final fracture of the cantilever occurred at regions where FIB damage was no longer influencing the crack tip. Hence, the interface toughness ($3\text{--}7 \text{ J/m}^2$) measured was well within a range that justifies crack deflection and continuous delamination observed. In a further step, guidelines for using the single cantilever delamination geometry to promote crack nucleation and propagation on the interface were provided. Conditions for interface crack nucleation were short crack and cantilever lengths, thick films, large elastic modulus, and large angle between the substrate and film. Once this condition is satisfied, an interface is nucleated and will grow along the interface till the driving force for crack branching into the film surpasses the driving force for interface crack.

These approaches have jointly helped to reduce increase in fracture toughness due to ion damage at the notch as follows:

- a) the effect of finite notch radius (approach 1,2, 3).
- b) residual stresses due ion implantation (approach 1, 3).

- c) redeposition (approach 1, 3).
- d) chemical interaction and segregation (approach 2).

7.2 Outlook

Within this thesis, the successes and challenges heralding mechanistic based understanding of fracture at the micron scale using nanoindentation based techniques have been presented. Testing protocols in the community involve the use of FIB fabricated geometries, and commercially available indenter system that can apply and measure loads / displacements with reasonable accuracy.

Geometry imperfections during FIB sample fabrication have in most cases led to the measurement of system dependent fracture properties. These imperfections could also include artefacts at the notch, culminating in huge scatter in data obtained from different groups for similar material systems. Sample fabrication artefacts are more detrimental in materials which show limited plasticity, where catastrophic failure reduces fracture measurements to a single value, which could be an underestimation or overestimation of true material properties.

This study has shown that the reliability of fracture measurements in small scale experiments can be improved in materials which are brittle at room temperature by geometry modification(s). On one hand, bridge-notched single cantilever beams with optimised notch dimensions show crack arrest before final failure. In these experiments, a sharp crack resulting from the arrest of the bridge notch failures reduces the influence of artefacts from notching ions on fracture toughness. Also, fracture toughness values can be calculated from the bridge notch and through thickness notch, increasing the total number of data points from a single experiment. Alternatively, a stable crack growth geometry can be used for the same category of materials. A simple cantilever-based delamination geometry that does not have the complexities of existing stable crack geometries was also presented in this study. The stability of the crack in the geometry eliminates the need for notch modification, and a sharp crack is initiated from the notch. Multiple values for fracture toughness can be calculated as crack grows, making it possible to obtain representative material property.

After comparing the two strategies presented in this thesis for mitigating sample fabrication artefacts from FIB, it can be concluded that the stable crack growth (single cantilever delamination) geometry is the best approach. This is because the crack grows beyond the FIB affected region. However, it should be noted that the present geometry was validated for interface delamination in a two-layer system. To use this geometry for single phase systems, further studies are required. On the other hand, the crack arrest strategy is well suited for single phase materials, but it is not yet known if it can be used for interface fracture problems. It is possible that crack arrest may not be sufficient to accommodate crack deflection into weak interfaces.

As a conclusion, to avoid FIB fabrication artefacts in small scale fracture studies of single phase materials that exhibit limited plasticity, it is recommended to use the crack arrest geometry. Additionally, for interface crack problems, the single cantilever delamination geometry is recommended instead of other more complex geometries.

References

- [1] T.L. Anderson, *Fracture Mechanics*, Third, CRC Press, 2005. <https://doi.org/10.1201/9781420058215>.
- [2] B. Lawn, Continuum aspects of crack propagation I: linear elastic crack-tip field, in: *Fract. Brittle Solids*, Cambridge University Press, 1993: pp. 16–50. <https://doi.org/10.1017/CBO9780511623127.004>.
- [3] G. Dehm, C. Motz, C. Scheu, H. Clemens, P.H. Mayrhofer, C. Mitterer, Mechanical size-effects in miniaturized and bulk materials, *Adv. Eng. Mater.* 8 (2006) 1033–1045. <https://doi.org/10.1002/adem.200600153>.
- [4] O. Kraft, P.A. Gruber, R. Mönig, D. Weygand, Plasticity in confined dimensions, *Annu. Rev. Mater. Res.* 40 (2010) 293–317. <https://doi.org/10.1146/annurev-matsci-082908-145409>.
- [5] G. Dehm, B.N. Jaya, R. Raghavan, C. Kirchlechner, Overview on micro- and nanomechanical testing: New insights in interface plasticity and fracture at small length scales, *Acta Mater.* 142 (2018) 248–282. <https://doi.org/10.1016/j.actamat.2017.06.019>.
- [6] C.A. Volkert, A.M. Minor, Focused Ion Beam Microscopy and Micromachining, *MRS Bull.* 32 (2007) 389–399. <https://doi.org/10.1557/mrs2007.62>.
- [7] S. Brinckmann, K. Matoy, C. Kirchlechner, G. Dehm, On the influence of microcantilever pre-crack geometries on the apparent fracture toughness of brittle materials, *Acta Mater.* 136 (2017) 281–287. <https://doi.org/10.1016/j.actamat.2017.07.014>.
- [8] J.P. Best, J. Zechner, I. Shorubalko, J.V. Oboňa, J. Wehrs, M. Morstein, J. Michler, A comparison of three different notching ions for small-scale fracture toughness measurement, *Scr. Mater.* 112 (2016) 71–74. <https://doi.org/10.1016/j.scriptamat.2015.09.014>.
- [9] C.E. Inglis, Stress in a plate due to the presence of cracks and sharp corners, *Trans. Inst. Nav. Archit.* 55 (1913) 219–241.
- [10] B. Lawn, The Griffith concept, in: I.M. Professor Davis E. A., Professor Ward (Ed.), *Fract. Brittle Solids*, Second, Cambridge Solid State Science Series, Cambridge University Press, Cambridge, n.d.: pp. 1–15.
- [11] A.A. Griffith, VI. The phenomena of rupture and flow in solids, *Philos. Trans. R. Soc. London. Ser. A, Contain. Pap. a Math. or Phys. Character.* 221 (1921) 163–198. <https://doi.org/10.1098/rsta.1921.0006>.
- [12] G.R. Irwin, Analysis of Stresses and Strains Near the End of a Crack Traversing a Plate, *J. Appl. Mech.* 24 (1957) 361–364. <https://doi.org/10.1115/1.4011547>.
- [13] I.N. Sneddon, The distribution of stress in the neighbourhood of a crack in an elastic solid, *Proc. R. Soc. London. Ser. A. Math. Phys. Sci.* 187 (1946) 229–260.

<https://doi.org/10.1098/rspa.1946.0077>.

- [14] H.M. Westergaard, Bearing Pressures and Cracks: Bearing Pressures Through a Slightly Waved Surface or Through a Nearly Flat Part of a Cylinder, and Related Problems of Cracks, *J. Appl. Mech.* 6 (1939) A49–A53. <https://doi.org/10.1115/1.4008919>.
- [15] Annual Book of ASTM Standards, “Standard test method for plane strain fracture toughness of metallic materials,” E 399-90 (1997).
- [16] M.D. Uchic, D.M. Dimiduk, J.N. Florando, W.D. Nix, Sample dimensions influence strength and crystal plasticity, *Science* (80-.). 305 (2004) 986–989. <https://doi.org/10.1126/science.1098993>.
- [17] Y.L. Kang, Z.F. Zhang, H.W. Wang, Q.H. Qin, Experimental investigations of the effect of thickness on fracture toughness of metallic foils, *Mater. Sci. Eng. A.* 394 (2005) 312–319. <https://doi.org/10.1016/j.msea.2004.11.044>.
- [18] P.A. Gruber, E. Arzt, R. Spolenak, Brittle-to-ductile transition in ultrathin Ta/Cu film systems, *J. Mater. Res.* 24 (2009) 1906–1918. <https://doi.org/10.1557/jmr.2009.0252>.
- [19] H. Hirakata, O. Nishijima, N. Fukuhara, T. Kondo, A. Yonezu, K. Minoshima, Size effect on fracture toughness of freestanding copper nano-films, *Mater. Sci. Eng. A.* 528 (2011) 8120–8127. <https://doi.org/10.1016/j.msea.2011.07.071>.
- [20] R.A. Meirom, T.E. Clark, C.L. Muhlstein, The role of specimen thickness in the fracture toughness and fatigue crack growth resistance of nanocrystalline platinum films, *Acta Mater.* 60 (2012) 1408–1417. <https://doi.org/10.1016/j.actamat.2011.11.015>.
- [21] H. Li, F. Ebrahimi, Ductile-to-brittle transition in nanocrystalline metals, *Adv. Mater.* 17 (2005) 1969–1972. <https://doi.org/10.1002/adma.200500436>.
- [22] I.A. Ovid’Ko, A.G. Sheinerman, Ductile vs. brittle behavior of pre-cracked nanocrystalline and ultrafine-grained materials, *Acta Mater.* 58 (2010) 5286–5294. <https://doi.org/10.1016/j.actamat.2010.05.058>.
- [23] B.N. Jaya, J.M. Wheeler, J. Wehrs, J.P. Best, R. Soler, J. Michler, C. Kirchlechner, G. Dehm, Microscale Fracture Behavior of Single Crystal Silicon Beams at Elevated Temperatures, *Nano Lett.* 16 (2016) 7597–7603. <https://doi.org/10.1021/acs.nanolett.6b03461>.
- [24] E.D. Hintsala, S. Bhowmick, X. Yueyue, R. Ballarini, S.A.S. Asif, W.W. Gerberich, Temperature dependent fracture initiation in microscale silicon, *Scr. Mater.* 130 (2017) 78–82. <https://doi.org/10.1016/j.scriptamat.2016.11.016>.
- [25] W. Kang, M.T.A. Saif, In situ study of size and temperature dependent brittle-to-ductile transition in single crystal silicon, *Adv. Funct. Mater.* 23 (2013) 713–719. <https://doi.org/10.1002/adfm.201201992>.
- [26] F. Östlund, K. Rzepiejewska-Malyska, K. Leifer, L.M. Hale, Y. Tang, R. Ballarini, W.W. Gerberich, J. Michler, Brittle-to-ductile transition in uniaxial compression of silicon pillars

- at room temperature, *Adv. Funct. Mater.* 19 (2009) 2439–2444. <https://doi.org/10.1002/adfm.200900418>.
- [27] R. Pippan, S. Wurster, D. Kiener, Fracture mechanics of micro samples: Fundamental considerations, *Mater. Des.* 159 (2018) 252–267. <https://doi.org/10.1016/j.matdes.2018.09.004>.
- [28] S. Zhang, X. Zhang, Toughness evaluation of hard coatings and thin films, *Thin Solid Films*. 520 (2012) 2375–2389. <https://doi.org/10.1016/j.tsf.2011.09.036>.
- [29] Y. Xiang, J. McKinnell, W.M. Ang, J.J. Vlassak, Measuring the fracture toughness of ultra-thin films with application to AlTa coatings, *Int. J. Fract.* 144 (2007) 173–179. <https://doi.org/10.1007/s10704-007-9095-0>.
- [30] Q.R. Hou, J. Gao, Fracture toughness of diamond-like carbon films, *Mod. Phys. Lett. B.* 15 (2001) 157–162. <https://doi.org/10.1142/s0217984901001550>.
- [31] X. Li, B. Bhushan, Evaluation of fracture toughness of ultra-thin amorphous carbon coatings deposited by different deposition techniques, *Thin Solid Films*. 355 (1999) 330–336. [https://doi.org/10.1016/S0040-6090\(99\)00446-0](https://doi.org/10.1016/S0040-6090(99)00446-0).
- [32] A.D. Norton, S. Falco, N. Young, J. Severs, R.I. Todd, Microcantilever investigation of fracture toughness and subcritical crack growth on the scale of the microstructure in Al₂O₃, *J. Eur. Ceram. Soc.* 35 (2015) 4521–4533. <https://doi.org/10.1016/j.jeurceramsoc.2015.08.023>.
- [33] B.N. Jaya, C. Kirchlechner, G. Dehm, Can microscale fracture tests provide reliable fracture toughness values? A case study in silicon, *J. Mater. Res.* 30 (2015) 686–698. <https://doi.org/10.1557/jmr.2015.2>.
- [34] I.W. Rangelow, P. Hudek, Lithography and Reactive Ion Etching in Microfabrication, in: *Photons and Local Probes*, 1995: pp. 325–344. https://doi.org/10.1007/978-94-011-0423-4_30.
- [35] B.D. Gates, Q. Xu, M. Stewart, D. Ryan, C.G. Willson, G.M. Whitesides, New approaches to nanofabrication: Molding, printing, and other techniques, *Chem. Rev.* 105 (2005) 1171–1196. <https://doi.org/10.1021/cr030076o>.
- [36] R.F.W. Pease, Electron beam lithography, *Contemp. Phys.* 22 (1981) 265–290. <https://doi.org/10.1080/00107518108231531>.
- [37] A.A. Tseng, K. Chen, C.D. Chen, K.J. Ma, Electron beam lithography in nanoscale fabrication: Recent development, *IEEE Trans. Electron. Packag. Manuf.* 26 (2003) 141–149. <https://doi.org/10.1109/TEPM.2003.817714>.
- [38] A. Pimpin, W. Srituravanich, Reviews on micro- and nanolithography techniques and their applications, *Eng. J.* 16 (2012) 37–55. <https://doi.org/10.4186/ej.2012.16.1.37>.
- [39] H.I. Smith, A review of submicron lithography, *Superlattices Microstruct.* 2 (1986) 129–142. [https://doi.org/10.1016/0749-6036\(86\)90077-7](https://doi.org/10.1016/0749-6036(86)90077-7).

- [40] A.E. Grigorescu, C.W. Hagen, Resists for sub-20-nm electron beam lithography with a focus on HSQ: State of the art, *Nanotechnology*. 20 (2009). <https://doi.org/10.1088/0957-4484/20/29/292001>.
- [41] J.A. Bondur, Dry Process Technology (Reactive Ion Etching)., *J Vac Sci Technol*. 13 (1976) 1023–1029. <https://doi.org/10.1116/1.569054>.
- [42] H. Jansen, H. Gardeniers, M. De Boer, M. Elwenspoek, J. Fluitman, A survey on the reactive ion etching of silicon in microtechnology, *J. Micromechanics Microengineering*. 6 (1996) 14–28. <https://doi.org/10.1088/0960-1317/6/1/002>.
- [43] R.G. Poulsen, Plasma Etching in Integrated Circuit Manufacture - a Review., *J Vac Sci Technol*. 14 (1976) 266–274. <https://doi.org/10.1116/1.569137>.
- [44] M. Huff, Recent Advances in Reactive Ion Etching and Applications of High-Aspect-Ratio Microfabrication, *Micromachines*. 12 (2021) 991. <https://doi.org/10.3390/mi12080991>.
- [45] S. Franssila, L. Sainiemi, M. Oy, *Encyclopedia of Microfluidics and Nanofluidics*, Springer US, Boston, MA, 2013. <https://doi.org/10.1007/978-3-642-27758-0>.
- [46] A.A. Ayón, R.L. Bayt, K.S. Breuer, Deep reactive ion etching: A promising technology for micro-and nanosatellites, *Smart Mater. Struct.* 10 (2001) 1135–1144. <https://doi.org/10.1088/0964-1726/10/6/302>.
- [47] K.A. Addae-Mensah, S. Retterer, S.R. Opalenik, D. Thomas, N. V. Lavrik, J.P. Wikswo, Cryogenic etching of silicon: An alternative method for fabrication of vertical microcantilever master molds, *J. Microelectromechanical Syst.* 19 (2010) 64–74. <https://doi.org/10.1109/JMEMS.2009.2037440>.
- [48] S. Tachi, K. Tsujimoto, S. Okudaira, Low-temperature reactive ion etching and microwave plasma etching of silicon, *Appl. Phys. Lett.* 52 (1988) 616–618. <https://doi.org/10.1063/1.99382>.
- [49] M. Francou, J.S. Danel, L. Peccoud, Deep and fast plasma etching for silicon micromachining, "Sensors Actuators, A Phys. 46 (1995) 17–21. [https://doi.org/10.1016/0924-4247\(94\)00852-9](https://doi.org/10.1016/0924-4247(94)00852-9).
- [50] T. Zijlstra, E. van der Drift, M.J.A. de Dood, E. Snoeks, A. Polman, Fabrication of two-dimensional photonic crystal waveguides for 1.5 μm in silicon by deep anisotropic dry etching, *J. Vac. Sci. Technol. B Microelectron. Nanom. Struct. Process. Meas. Phenom.* 17 (1999) 2734–2739. <https://doi.org/10.1116/1.591054>.
- [51] R. Clampitt, P.W. Mingay, S.T. Davies, Micromachining with focused ion beams, *Sensors Actuators A. Phys.* 25 (1990) 15–20. [https://doi.org/10.1016/0924-4247\(90\)87003-2](https://doi.org/10.1016/0924-4247(90)87003-2).
- [52] A.A. Tseng, Recent developments in micromilling using focused ion beam technology, *J. Micromechanics Microengineering*. 14 (2004). <https://doi.org/10.1088/0960-1317/14/4/R01>.
- [53] R. Clampitt, K.L. Aitken, D.K. Jefferies, Abstract: Intense field-emission ion source of

- liquid metals, *J. Vac. Sci. Technol.* 12 (1975) 1208–1208. <https://doi.org/10.1116/1.568496>.
- [54] M.T. Postek, A.E. Vldar, J. Kramar, L.A. Stern, J. Notte, S. McVey, Helium ion microscopy: A new technique for semiconductor metrology and nanotechnology, *AIP Conf. Proc.* 931 (2007) 161–167. <https://doi.org/10.1063/1.2799363>.
- [55] K. Sugioka, Progress in ultrafast laser processing and future prospects, *Nanophotonics*. 6 (2017) 393–413. <https://doi.org/10.1515/nanoph-2016-0004>.
- [56] S. Ma, J.P. McDonald, B. Tryon, S.M. Yalisove, T.M. Pollock, Femtosecond laser ablation regimes in a single-crystal superalloy, *Metall. Mater. Trans. A Phys. Metall. Mater. Sci.* 38 A (2007) 2349–2357. <https://doi.org/10.1007/s11661-007-9260-0>.
- [57] B.N. Chichkov, C. Momma, S. Nolte, F. Alvensleben, A. Tünnermann, Femtosecond, picosecond and nanosecond laser ablation of solids, *Appl. Phys. A Mater. Sci. Process.* 63 (1996) 109–115. <https://doi.org/10.1007/BF01567637>.
- [58] Y.C. Lim, K.J. Altman, D.F. Farson, K.M. Flores, Micropillar fabrication on bovine cortical bone by direct-write femtosecond laser ablation, *J. Biomed. Opt.* 14 (2009) 064021. <https://doi.org/10.1117/1.3268444>.
- [59] T. Kim, H.S. Kim, M. Hetterich, D. Jones, J.M. Girkin, E. Bente, M.D. Dawson, Femtosecond laser machining of gallium nitride, *Mater. Sci. Eng. B.* 82 (2001) 262–264. [https://doi.org/10.1016/S0921-5107\(00\)00790-X](https://doi.org/10.1016/S0921-5107(00)00790-X).
- [60] M.J. Pfeifenberger, M. Mangang, S. Wurster, J. Reiser, A. Hohenwarter, W. Pfleging, D. Kiener, R. Pippan, The use of femtosecond laser ablation as a novel tool for rapid micro-mechanical sample preparation, *Mater. Des.* 121 (2017) 109–118. <https://doi.org/10.1016/j.matdes.2017.02.012>.
- [61] H.M. Van Driel, J.E. Sipe, J.F. Young, Laser-induced periodic surface structure on solids: A universal phenomenon, *Phys. Rev. Lett.* 49 (1982) 1955–1958. <https://doi.org/10.1103/PhysRevLett.49.1955>.
- [62] Z. Guosheng, P.M. Fauchet, A.E. Siegman, Growth of spontaneous periodic surface structures on solids during laser illumination, *Phys. Rev. B.* 26 (1982) 5366–5381. <https://doi.org/10.1103/PhysRevB.26.5366>.
- [63] M.P. Echlin, M.S. Titus, M. Straw, P. Gumbsch, T.M. Pollock, Materials response to glancing incidence femtosecond laser ablation, *Acta Mater.* 124 (2017) 37–46. <https://doi.org/10.1016/j.actamat.2016.10.055>.
- [64] B. Lawn, R. Wilshaw, Indentation fracture: principles and applications, *J. Mater. Sci.* 10 (1975) 1049–1081. <https://doi.org/10.1007/BF00823224>.
- [65] B.R. Lawn, M. V. Swain, Microfracture beneath point indentations in brittle solids, *J. Mater. Sci.* 10 (1975) 113–122. <https://doi.org/10.1007/BF00541038>.
- [66] G.R. Anstis, P. Chantiikul, B.R. Lawn, D.B. Marshall, A Critical Evaluation of Indentation Techniques for Measuring Fracture Toughness: I, Direct Crack Measurements, *J. Am.*

- Ceram. Soc. 64 (1981) 533–538. <https://doi.org/10.1111/j.1151-2916.1981.tb10320.x>.
- [67] P. Ostojic, R. McPherson, A review of indentation fracture theory: its development, principles and limitations, *Int. J. Fract.* 33 (1987) 297–312. <https://doi.org/10.1007/BF00044418>.
- [68] B.R. Lawn, A.G. Evans, A model for crack initiation in elastic/plastic indentation fields, *J. Mater. Sci.* 12 (1977) 2195–2199. <https://doi.org/10.1007/BF00552240>.
- [69] J.T. Hagan, S. Van Der Zwaag, Plastic processes in a range of soda-lime-silica glasses, *J. Non. Cryst. Solids.* 64 (1984) 249–268. [https://doi.org/10.1016/0022-3093\(84\)90221-7](https://doi.org/10.1016/0022-3093(84)90221-7).
- [70] B.R. Lawn, D.B. Marshall, Indentation Fractography: a Measure of Brittleness., *J. Res. Natl. Bur. Stand. (United States)*. 89 (1984) 435–451. <https://doi.org/10.6028/jres.089.024>.
- [71] D.S. Harding, W.C. Oliver, G.M. Pharr, Cracking during nanoindentation and its use in the measurement of fracture toughness, *Mater. Res. Soc. Symp. - Proc.* 356 (1995) 663–668. <https://doi.org/10.1557/proc-356-663>.
- [72] G.M. Pharr, Measurement of mechanical properties by ultra-low load indentation, *Mater. Sci. Eng. A.* 253 (1998) 151–159. [https://doi.org/10.1016/s0921-5093\(98\)00724-2](https://doi.org/10.1016/s0921-5093(98)00724-2).
- [73] J. il Jang, G.M. Pharr, Influence of indenter angle on cracking in Si and Ge during nanoindentation, *Acta Mater.* 56 (2008) 4458–4469. <https://doi.org/10.1016/j.actamat.2008.05.005>.
- [74] M. Sebastiani, K.E. Johanns, E.G. Herbert, G.M. Pharr, Measurement of fracture toughness by nanoindentation methods: Recent advances and future challenges, *Curr. Opin. Solid State Mater. Sci.* 19 (2015) 324–333. <https://doi.org/10.1016/j.cossms.2015.04.003>.
- [75] H. Gopalan, A. Marshal, M. Hans, D. Primetzhofer, N. Cautlaerts, B. Breitbach, B. Völker, C. Kirchlechner, J.M. Schneider, G. Dehm, On the interplay between microstructure, residual stress and fracture toughness of (Hf-Nb-Ta-Zr)C multi-metal carbide hard coatings, *Mater. Des.* 224 (2022) 111323. <https://doi.org/10.1016/j.matdes.2022.111323>.
- [76] F.F. Klimashin, L. Lobmaier, N. Koutná, D. Holec, P.H. Mayrhofer, The MoN–TaN system: Role of vacancies in phase stability and mechanical properties, *Mater. Des.* 202 (2021). <https://doi.org/10.1016/j.matdes.2021.109568>.
- [77] J.H. Lee, Y.F. Gao, K.E. Johanns, G.M. Pharr, Cohesive interface simulations of indentation cracking as a fracture toughness measurement method for brittle materials, *Acta Mater.* 60 (2012) 5448–5467. <https://doi.org/10.1016/j.actamat.2012.07.011>.
- [78] K.E. Johanns, J.H. Lee, Y.F. Gao, G.M. Pharr, An evaluation of the advantages and limitations in simulating indentation cracking with cohesive zone finite elements, *Model. Simul. Mater. Sci. Eng.* 22 (2014). <https://doi.org/10.1088/0965-0393/22/1/015011>.
- [79] K. Komai, K. Minoshima, S. Inoue, Fracture and fatigue behavior of single crystal silicon microelements and nanoscopic AFM damage evaluation, *Microsyst. Technol.* 5 (1998) 30–37. <https://doi.org/10.1007/s005420050137>.

- [80] D. Son, J.H. Jeong, D. Kwon, Film-thickness considerations in microcantilever-beam test in measuring mechanical properties of metal thin film, *Thin Solid Films*. 437 (2003) 182–187. [https://doi.org/10.1016/S0040-6090\(03\)00645-X](https://doi.org/10.1016/S0040-6090(03)00645-X).
- [81] J. McCarthy, Z. Pei, M. Becker, D. Atteridge, FIB micromachined submicron thickness cantilevers for the study of thin film properties, *Thin Solid Films*. 358 (2000) 146–151. [https://doi.org/10.1016/S0040-6090\(99\)00680-X](https://doi.org/10.1016/S0040-6090(99)00680-X).
- [82] D. Di Maio, S.G. Roberts, Measuring fracture toughness of coatings using focused-ion-beam-machined microbeams, *J. Mater. Res.* 20 (2005) 299–302. <https://doi.org/10.1557/JMR.2005.0048>.
- [83] K. Matoy, H. Schönherr, T. Detzel, T. Schöberl, R. Pippan, C. Motz, G. Dehm, A comparative micro-cantilever study of the mechanical behavior of silicon based passivation films, *Thin Solid Films*. 518 (2009) 247–256. <https://doi.org/10.1016/j.tsf.2009.07.143>.
- [84] G. Žagar, V. Pejchal, M.G. Mueller, L. Michelet, A. Mortensen, Fracture toughness measurement in fused quartz using triangular chevron-notched micro-cantilevers, *Scr. Mater.* 112 (2016) 132–135. <https://doi.org/10.1016/j.scriptamat.2015.09.032>.
- [85] M.G. Mueller, G. Žagar, A. Mortensen, Stable room-temperature micron-scale crack growth in single-crystalline silicon, *J. Mater. Res.* 32 (2017) 3617–3626. <https://doi.org/10.1557/jmr.2017.238>.
- [86] B. Völker, B. Stelzer, S. Mráz, H. Rueß, R. Sahu, C. Kirchlechner, G. Dehm, J.M. Schneider, On the fracture behavior of Cr₂AlC coatings, *Mater. Des.* 206 (2021). <https://doi.org/10.1016/j.matdes.2021.109757>.
- [87] S. Massl, W. Thomma, J. Keckes, R. Pippan, Investigation of fracture properties of magnetron-sputtered TiN films by means of a FIB-based cantilever bending technique, *Acta Mater.* 57 (2009) 1768–1776. <https://doi.org/10.1016/j.actamat.2008.12.018>.
- [88] A. Riedl, R. Daniel, M. Stefanelli, T. Schöberl, O. Kolednik, C. Mitterer, J. Keckes, A novel approach for determining fracture toughness of hard coatings on the micrometer scale, *Scr. Mater.* 67 (2012) 708–711. <https://doi.org/10.1016/j.scriptamat.2012.06.034>.
- [89] F. Iqbal, J. Ast, M. Göken, K. Durst, In situ micro-cantilever tests to study fracture properties of NiAl single crystals, *Acta Mater.* 60 (2012) 1193–1200. <https://doi.org/10.1016/j.actamat.2011.10.060>.
- [90] W. Luo, C. Kirchlechner, X. Fang, S. Brinckmann, G. Dehm, F. Stein, Influence of composition and crystal structure on the fracture toughness of NbCo₂ Laves phase studied by micro-cantilever bending tests, *Mater. Des.* 145 (2018) 116–121. <https://doi.org/10.1016/j.matdes.2018.02.045>.
- [91] C. Tian, C. Kirchlechner, The fracture toughness of martensite islands in dual-phase DP800 steel, *J. Mater. Res.* 36 (2021) 2495–2504. <https://doi.org/10.1557/s43578-021-00150-4>.
- [92] S. Gabel, S. Giese, R.U. Webler, S. Neumeier, M. Göken, Microcantilever Fracture Tests of α -Cr Containing NiAl Bond Coats, *Adv. Eng. Mater.* 24 (2022).

- <https://doi.org/10.1002/adem.202101429>.
- [93] N. Jaya B, V. Jayaram, S.K. Biswas, A new method for fracture toughness determination of graded (Pt,Ni)Al bond coats by microbeam bend tests, *Philos. Mag.* 92 (2012) 3326–3345. <https://doi.org/10.1080/14786435.2012.669068>.
- [94] B.N. Jaya, S. Bhowmick, S.A.S. Asif, O.L. Warren, V. Jayaram, Optimization of clamped beam geometry for fracture toughness testing of micron-scale samples, *Philos. Mag.* 95 (2015) 1945–1966. <https://doi.org/10.1080/14786435.2015.1010623>.
- [95] B.N. Jaya, V. Jayaram, Crack stability in edge-notched clamped beam specimens: Modeling and experiments, *Int. J. Fract.* 188 (2014) 213–228. <https://doi.org/10.1007/s10704-014-9956-2>.
- [96] B. Lawn, *Fracture of brittle solids.*, Cambridge Univeristy Press, Cambridge, 1993.
- [97] G. Sernicola, T. Giovannini, P. Patel, J.R. Kermode, D.S. Balint, T. Ben Britton, F. Giuliani, In situ stable crack growth at the micron scale, *Nat. Commun.* 8 (2017). <https://doi.org/10.1038/s41467-017-00139-w>.
- [98] S. Liu, J.M. Wheeler, P.R. Howie, X.T. Zeng, J. Michler, W.J. Clegg, Measuring the fracture resistance of hard coatings, *Appl. Phys. Lett.* 102 (2013) 1–5. <https://doi.org/10.1063/1.4803928>.
- [99] F.W. DelRio, S.J. Grutzik, W.M. Mook, S.M. Dickens, P.G. Kotula, E.D. Hintsala, D.D. Stauffer, B.L. Boyce, Eliciting stable nanoscale fracture in single-crystal silicon, *Mater. Res. Lett.* 10 (2022) 728–735. <https://doi.org/10.1080/21663831.2022.2088251>.
- [100] M. Sebastiani, K.E. Johanns, E.G. Herbert, F. Carassiti, G.M. Pharr, A novel pillar indentation splitting test for measuring fracture toughness of thin ceramic coatings, *Philos. Mag.* 95 (2015) 1928–1944. <https://doi.org/10.1080/14786435.2014.913110>.
- [101] M. Sebastiani, E. Bemporad, F. Carassiti, N. Schwarzer, Residual stress measurement at the micrometer scale: Focused ion beam (FIB) milling and nanoindentation testing, *Philos. Mag.* 91 (2011) 1121–1136. <https://doi.org/10.1080/14786431003800883>.
- [102] M. Sebastiani, C. Eberl, E. Bemporad, G.M. Pharr, Depth-resolved residual stress analysis of thin coatings by a new FIB-DIC method, *Mater. Sci. Eng. A.* 528 (2011) 7901–7908. <https://doi.org/10.1016/j.msea.2011.07.001>.
- [103] E. Rossi, J. Bauer, M. Sebastiani, Humidity-dependent flaw sensitivity in the crack propagation resistance of 3D-printed nano-ceramics, *Scr. Mater.* 194 (2021) 113684. <https://doi.org/10.1016/j.scriptamat.2020.113684>.
- [104] Y. Zhang, M. Bartosik, S. Brinckmann, S. Lee, C. Kirchlechner, Direct observation of crack arrest after bridge notch failure: A strategy to increase statistics and reduce FIB-artifacts in micro-cantilever testing, *Mater. Des.* 233 (2023) 112188. <https://doi.org/10.1016/j.matdes.2023.112188>.
- [105] J.C. Newman, A Review of Chevron-Notched Fracture Specimens, in: *Chevron-Notched*

- Specimens Test. *Stress Anal.*, 1984: pp. 5–31. <https://doi.org/10.1520/stp32719s>.
- [106] L.Y. Chao, D. Singh, D.K. Shetty, Effects of subcritical crack growth on fracture toughness of ceramics assessed in chevron-notched three-point bend tests, *J. Eng. Gas Turbines Power.* 111 (1989) 168–173. <https://doi.org/10.1115/1.3240219>.
- [107] P.A. Withey, R.L. Brett, P. Bowen, Use of chevron notches for fracture toughness determination in brittle solids, *Mater. Sci. Technol. (United Kingdom)*. 8 (1992) 805–810. <https://doi.org/10.1179/mst.1992.8.9.805>.
- [108] M.G. Mueller, V. Pejchal, G. Žagar, A. Singh, M. Cantoni, A. Mortensen, Fracture toughness testing of nanocrystalline alumina and fused quartz using chevron-notched microbeams, *Acta Mater.* 86 (2015) 385–395. <https://doi.org/10.1016/j.actamat.2014.12.016>.
- [109] F.Y. Cui, R.P. Vinci, A chevron-notched bowtie micro-beam bend test for fracture toughness measurement of brittle materials, *Scr. Mater.* 132 (2017) 53–57. <https://doi.org/10.1016/j.scriptamat.2017.01.031>.
- [110] B.S. Li, T.J. Marrow, S.G. Roberts, D.E.J. Armstrong, Evaluation of Fracture Toughness Measurements Using Chevron-Notched Silicon and Tungsten Microcantilevers, *Jom.* 71 (2019) 3378–3389. <https://doi.org/10.1007/s11837-019-03696-1>.
- [111] B. Völker, S. Venkatesan, W. Heinz, K. Matoy, R. Roth, J.M. Batke, M.J. Cordill, G. Dehm, Following crack path selection in multifilm structures with weak and strong interfaces by in situ 4-point-bending, *J. Mater. Res.* 30 (2015) 1090–1097. <https://doi.org/10.1557/jmr.2015.88>.
- [112] C. Wu, C. Wei, Y. Li, In situ mechanical characterization of the mixed-mode fracture strength of the Cu/Si interface for TSV structures, *Micromachines*. 10 (2019). <https://doi.org/10.3390/mi10020086>.
- [113] M.E.M. Zebar, M.L. Hattali, N. Mesrati, Interfacial fracture toughness measurement in both steady state and transient regimes using four-point bending test, *Int. J. Fract.* 222 (2020) 123–135. <https://doi.org/10.1007/s10704-020-00437-3>.
- [114] Z. Huang, Z. Suo, G. Xu, J. He, J.H. Prévost, N. Sukumar, Initiation and arrest of an interfacial crack in a four-point bend test, *Eng. Fract. Mech.* 72 (2005) 2584–2601. <https://doi.org/10.1016/j.engfracmech.2005.04.002>.
- [115] H. Hirakata, T. Hirako, Y. Takahashi, Y. Matsuoka, T. Kitamura, Creep crack initiation at a free edge of an interface between submicron thick elements, *Eng. Fract. Mech.* 75 (2008) 2907–2920. <https://doi.org/10.1016/j.engfracmech.2008.01.007>.
- [116] Y. Yan, T. Sumigawa, L. Guo, T. Kitamura, Strength evaluation of a selected interface in multi-layered nano-material, *Eng. Fract. Mech.* 116 (2014) 204–212. <https://doi.org/10.1016/j.engfracmech.2013.12.014>.
- [117] H. Hirakata, T. Kitamura, T. Kusano, Pre-cracking technique for fracture mechanics experiments along interface between thin film and substrate, *Eng. Fract. Mech.* 72 (2005)

- 1892–1904. <https://doi.org/10.1016/j.engfracmech.2004.08.010>.
- [118] R. Konetschnik, R. Daniel, R. Brunner, D. Kiener, Selective interface toughness measurements of layered thin films, *AIP Adv.* 7 (2017). <https://doi.org/10.1063/1.4978337>.
- [119] J.L. Mead, M. Lu, H. Huang, Inducing stable interfacial delamination in a multilayer system by four-point bending of microbridges, *Surf. Coatings Technol.* 320 (2017) 478–482. <https://doi.org/10.1016/j.surfcoat.2016.11.069>.
- [120] R. Jacobsson, Measurement of the adhesion of thin films, *Thin Solid Films.* 34 (1976) 191–199. [https://doi.org/10.1016/0040-6090\(76\)90454-5](https://doi.org/10.1016/0040-6090(76)90454-5).
- [121] T. Hull, J. Colligon, A. Hill, Measurement of thin film adhesion, *Vacuum.* 37 (1987) 327–330. [https://doi.org/10.1016/0042-207X\(87\)90018-2](https://doi.org/10.1016/0042-207X(87)90018-2).
- [122] M. Sexsmith, T. Troczynski, Peel strength of thermal sprayed coatings, *J. Therm. Spray Technol.* 5 (1996) 196–206. <https://doi.org/10.1007/BF02646433>.
- [123] J. Chen, S.J. Bull, Approaches to investigate delamination and interfacial toughness in coated systems: An overview, *J. Phys. D. Appl. Phys.* 44 (2011). <https://doi.org/10.1088/0022-3727/44/3/034001>.
- [124] Z. Chen, K. Zhou, X. Lu, Y.C. Lam, A review on the mechanical methods for evaluating coating adhesion, *Acta Mech.* 225 (2014) 431–452. <https://doi.org/10.1007/s00707-013-0979-y>.
- [125] M. Laugier, The development of the scratch test technique for the determination of the adhesion of coatings, *Thin Solid Films.* 76 (1981) 289–294. [https://doi.org/10.1016/0040-6090\(81\)90700-8](https://doi.org/10.1016/0040-6090(81)90700-8).
- [126] S.J. Bull, E.G. Berasetegui, An overview of the potential of quantitative coating adhesion measurement by scratch testing, *Tribol. Int.* 39 (2006) 99–114. <https://doi.org/10.1016/j.triboint.2005.04.013>.
- [127] P.A. Steinmann, Y. Tardy, H.E. Hintermann, Adhesion testing by the scratch test method: The influence of intrinsic and extrinsic parameters on the critical load, *Thin Solid Films.* 154 (1987) 333–349. [https://doi.org/10.1016/0040-6090\(87\)90377-4](https://doi.org/10.1016/0040-6090(87)90377-4).
- [128] S.T. Gonczy, N. Randall, An ASTM standard for quantitative scratch adhesion testing of thin, hard ceramic coatings, *Int. J. Appl. Ceram. Technol.* 2 (2005) 422–428. <https://doi.org/10.1111/j.1744-7402.2005.02043.x>.
- [129] A. Bagchi, G.E. Lucas, Z. Suo, A.G. Evans, A new procedure for measuring the decohesion energy for thin ductile films on substrates, *J. Mater. Res.* 9 (1994) 1734–1741. <https://doi.org/10.1557/JMR.1994.1734>.
- [130] A.A. Volinsky, N.R. Moody, W.W. Gerberich, Interfacial toughness measurements for thin films on substrates, *Acta Mater.* 50 (2002) 441–466. [https://doi.org/10.1016/S1359-6454\(01\)00354-8](https://doi.org/10.1016/S1359-6454(01)00354-8).
- [131] D.B. Marshall, A.G. Evans, Measurement of adherence of residually stressed thin films by

- indentation. I. Mechanics of interface delamination, *J. Appl. Phys.* 56 (1984) 2632–2638. <https://doi.org/10.1063/1.333794>.
- [132] A. Roshanghias, G. Khatibi, R. Pelzer, J. Steinbrenner, On the effects of thickness on adhesion of TiW diffusion barrier coatings in silicon integrated circuits, *Surf. Coatings Technol.* 259 (2014) 386–392. <https://doi.org/10.1016/j.surfcoat.2014.10.065>.
- [133] A. Kleinbichler, M.J. Pfeifenberger, J. Zechner, N.R. Moody, D.F. Bahr, M.J. Cordill, New Insights into Nanoindentation-Based Adhesion Testing, *Jom.* 69 (2017) 2237–2245. <https://doi.org/10.1007/s11837-017-2496-2>.
- [134] M.D. Kriese, W.W. Gerberich, N.R. Moody, Quantitative adhesion measures of multilayer films: Part I. Indentation mechanics, *J. Mater. Res.* 14 (1999) 3007–3018. <https://doi.org/10.1557/JMR.1999.0404>.
- [135] K. Matoy, T. Detzel, M. Müller, C. Motz, G. Dehm, Interface fracture properties of thin films studied by using the micro-cantilever deflection technique, *Surf. Coatings Technol.* 204 (2009) 878–881. <https://doi.org/10.1016/j.surfcoat.2009.09.013>.
- [136] J. Schaufler, C. Schmid, K. Durst, M. Göken, Determination of the interfacial strength and fracture toughness of a-C:H coatings by in-situ microcantilever bending, *Thin Solid Films.* 522 (2012) 480–484. <https://doi.org/10.1016/j.tsf.2012.08.031>.
- [137] B. Völker, W. Heinz, R. Roth, J.M. Batke, M.J. Cordill, G. Dehm, Downscaling metal-dielectric interface fracture experiments to sub-micron dimensions: A feasibility study using TEM, *Surf. Coatings Technol.* 270 (2015) 1–7. <https://doi.org/10.1016/j.surfcoat.2015.03.027>.
- [138] Y.Q. Wang, R. Fritz, D. Kiener, J.Y. Zhang, G. Liu, O. Kolednik, R. Pippan, J. Sun, Fracture behavior and deformation mechanisms in nanolaminated crystalline/amorphous micro-cantilevers, *Acta Mater.* 180 (2019) 73–83. <https://doi.org/10.1016/j.actamat.2019.09.002>.
- [139] J. Zechner, G. Mohanty, C. Frantz, H. Cebeci, L. Philippe, J. Michler, Mechanical properties and interface toughness of metal filled nanoporous anodic aluminum oxide coatings on aluminum, *Surf. Coatings Technol.* 260 (2014) 246–250. <https://doi.org/10.1016/j.surfcoat.2014.08.086>.
- [140] T. Sumigawa, T. Murakami, T. Shishido, T. Kitamura, Cu/Si interface fracture due to fatigue of copper film in nanometer scale, *Mater. Sci. Eng. A.* 527 (2010) 6518–6523. <https://doi.org/10.1016/j.msea.2010.07.002>.
- [141] R. Damani, R. Gstrein, R. Danzer, Critical Notch-Root Radius Effect in SENB-S Fracture Toughness Testing, *J. Eur. Ceram. Soc.* 16 (1996) 695–702. [https://doi.org/10.1016/0955-2219\(95\)00197-2](https://doi.org/10.1016/0955-2219(95)00197-2).
- [142] C.V. Rocha, C. Albano Da Costa, Effect of notch-root radius on the fracture toughness of composite Si₃N₄ ceramics, *J. Mater. Eng. Perform.* 15 (2006) 591–595. <https://doi.org/10.1361/105994906X136106>.
- [143] L.S. Nui, C. Chehimi, G. Pluvinaige, Stress field near a large blunted tip V-notch and

- application of the concept of the critical notch stress intensity factor (NSIF) to the fracture toughness of very brittle materials, *Eng. Fract. Mech.* 49 (1994) 325–335. [https://doi.org/10.1016/0013-7944\(94\)90262-3](https://doi.org/10.1016/0013-7944(94)90262-3).
- [144] S. Wurster, C. Motz, R. Pippan, Characterization of the fracture toughness of micro-sized tungsten single crystal notched specimens, *Philos. Mag.* 92 (2012) 1803–1825. <https://doi.org/10.1080/14786435.2012.658449>.
- [145] J.P. Best, J. Zechner, J.M. Wheeler, R. Schoeppner, M. Morstein, J. Michler, Small-scale fracture toughness of ceramic thin films: the effects of specimen geometry, ion beam notching and high temperature on chromium nitride toughness evaluation, *Philos. Mag.* 96 (2016) 3552–3569. <https://doi.org/10.1080/14786435.2016.1223891>.
- [146] P.J. Burnett, T.F. Page, An investigation of ion implantation-induced near-surface stresses and their effects in sapphire and glass, *J. Mater. Sci.* 20 (1985) 4624–4646. <https://doi.org/10.1007/BF00559353>.
- [147] A.M. Korsunsky, J. Guérolé, E. Salvati, T. Sui, M. Mousavi, A. Prakash, E. Bitzek, Quantifying eigenstrain distributions induced by focused ion beam damage in silicon, *Mater. Lett.* 185 (2016) 47–49. <https://doi.org/10.1016/j.matlet.2016.08.111>.
- [148] E.I. Preiß, B. Merle, Y. Xiao, F. Gannott, J.P. Liebig, J.M. Wheeler, M. Göken, Applicability of focused Ion beam (FIB) milling with gallium, neon, and xenon to the fracture toughness characterization of gold thin films, *J. Mater. Res.* 36 (2021) 2505–2514. <https://doi.org/10.1557/s43578-020-00045-w>.
- [149] S. Lee, J. Jeong, Y. Kim, S.M. Han, D. Kiener, S.H. Oh, FIB-induced dislocations in Al submicron pillars: Annihilation by thermal annealing and effects on deformation behavior, *Acta Mater.* 110 (2016) 283–294. <https://doi.org/10.1016/j.actamat.2016.03.017>.
- [150] D. Kiener, C. Motz, M. Rester, M. Jenko, G. Dehm, FIB damage of Cu and possible consequences for miniaturized mechanical tests, *Mater. Sci. Eng. A.* 459 (2007) 262–272. <https://doi.org/10.1016/j.msea.2007.01.046>.
- [151] J. Marien, J.M. Plitzko, R. Spolenak, R.M. Keller, J. Mayer, Quantitative electron spectroscopic imaging studies of microelectronic metallization layers, *J. Microsc.* 194 (1999) 71–78. <https://doi.org/10.1046/j.1365-2818.1999.00476.x>.
- [152] E.I. Preiß, B. Merle, M. Göken, Understanding the extremely low fracture toughness of freestanding gold thin films by in-situ bulge testing in an AFM, *Mater. Sci. Eng. A.* 691 (2017) 218–225. <https://doi.org/10.1016/j.msea.2017.03.037>.
- [153] J.M. Cairney, P.R. Munroe, Redeposition effects in transmission electron microscope specimens of FeAl-WC composites prepared using a focused ion beam, *Micron.* 34 (2003) 97–107. [https://doi.org/10.1016/S0968-4328\(03\)00007-6](https://doi.org/10.1016/S0968-4328(03)00007-6).
- [154] T. Vermeij, E. Plancher, C.C. Tasan, Preventing damage and redeposition during focused ion beam milling: The “umbrella” method, *Ultramicroscopy.* 186 (2018) 35–41. <https://doi.org/10.1016/j.ultramic.2017.12.012>.

- [155] H. Yamaguchi, A. Shimase, S. Haraichi, T. Miyauchi, Characteristics of Silicon Removal By Fine Focused Gallium Ion Beam., *J. Vac. Sci. Technol. B Microelectron. Process. Phenom.* 3 (1984) 71–74. <https://doi.org/10.1116/1.583294>.
- [156] S. Rubanov, P.R. Munroe, FIB-induced damage in silicon, *J. Microsc.* 214 (2004) 213–221. <https://doi.org/10.1111/j.0022-2720.2004.01327.x>.
- [157] Y. Huang, D.J.H. Cockayne, C. Marsh, J.M. Titchmarsh, A.K. Petford-Long, Self-organized amorphous material in silicon (0 0 1) by focused ion beam (FIB) system, *Appl. Surf. Sci.* 252 (2005) 1954–1958. <https://doi.org/10.1016/j.apsusc.2005.03.175>.
- [158] S. Rajsiri, B.W. Kempshall, S.M. Schwarz, L.A. Giannuzzi, FIB damage in silicon: Amorphization or redeposition?, *Microsc. Microanal.* 8 (2002) 50–51. <https://doi.org/10.1017/s1431927602101577>.
- [159] N.I. Borgardt, A. V. Romyantsev, R.L. Volkov, Y.A. Chaplygin, Sputtering of redeposited material in focused ion beam silicon processing, *Mater. Res. Express.* 5 (2018). <https://doi.org/10.1088/2053-1591/aaace1>.
- [160] K.A. Unocic, M.J. Mills, G.S. Daehn, Effect of gallium focused ion beam milling on preparation of aluminium thin foils, *J. Microsc.* 240 (2010) 227–238. <https://doi.org/10.1111/j.1365-2818.2010.03401.x>.
- [161] Y. Xiao, J. Wehrs, H. Ma, T. Al-Samman, S. Korte-Kerzel, M. Göken, J. Michler, R. Spolenak, J.M. Wheeler, Investigation of the deformation behavior of aluminum micropillars produced by focused ion beam machining using Ga and Xe ions, *Scr. Mater.* 127 (2017) 191–194. <https://doi.org/10.1016/j.scriptamat.2016.08.028>.
- [162] Y. Xiao, V. Maier-Kiener, J. Michler, R. Spolenak, J.M. Wheeler, Deformation behavior of aluminum pillars produced by Xe and Ga focused ion beams: Insights from strain rate jump tests, *Mater. Des.* 181 (2019) 107914. <https://doi.org/10.1016/j.matdes.2019.107914>.
- [163] R.C. Hugo, R.G. Hoagland, In-situ TEM observation of aluminum embrittlement by liquid gallium, *Scr. Mater.* 38 (1998) 523–529. [https://doi.org/10.1016/S1359-6462\(97\)00464-8](https://doi.org/10.1016/S1359-6462(97)00464-8).
- [164] R.C. Hugo, R.G. Hoagland, Kinetics of gallium penetration into aluminum grain boundaries - in situ TEM observations and atomistic models, *Acta Mater.* 48 (2000) 1949–1957. [https://doi.org/10.1016/S1359-6454\(99\)00463-2](https://doi.org/10.1016/S1359-6454(99)00463-2).
- [165] K.E. Petersen, Silicon as a mechanical material, *Micromechanics MEMS Class. Semin. Pap. to 1990.* 70 (1997) 58–95. <https://doi.org/10.1109/9780470545263.sect1>.
- [166] M. Hopcroft, What is the Young 's Modulus of Silicon ? What is the Crystal Orientation in a Silicon Wafer ?, *Phys. Acoust.* 19 (2007) 229–238.
- [167] T. Kim, J. Lee, Fabrication and characterization of silicon-on-insulator wafers, *Micro Nano Syst. Lett.* 11 (2023). <https://doi.org/10.1186/s40486-023-00181-y>.
- [168] L. Haobing, F. Chollet, Layout controlled one-step dry etch and release of MEMS using deep RIE on SOI wafer, *J. Microelectromechanical Syst.* 15 (2006) 541–547.

<https://doi.org/10.1109/JMEMS.2006.876660>.

- [169] R.O. Ritchie, Failure of silicon: Crack formation and propagation, in: 13th Work. Crystalline Sol. Cell Mater. Process. Vail Color., 2003.
- [170] R.O. Ritchie, 3 th Workshop on Crystalline Solar Cell Materials and Processes Failure of Silicon: Failure of Silicon: Crack Formation and Propagation Crack Formation and Propagation Work supported by the, Comput. Methods Appl. Mech. Eng. 320 (2003) 287–334. <https://linkinghub.elsevier.com/retrieve/pii/S0045782516316176>.
- [171] M. Tanaka, K. Higashida, H. Nakashima, H. Takagi, M. Fujiwara, Orientation dependence of fracture toughness measured by indentation methods and its relation to surface energy in single crystal silicon, Int. J. Fract. 139 (2006) 383–394. <https://doi.org/10.1007/s10704-006-0021-7>.
- [172] F.W. DelRio, R.F. Cook, B.L. Boyce, Fracture strength of micro- and nano-scale silicon components, Appl. Phys. Rev. 2 (2015). <https://doi.org/10.1063/1.4919540>.
- [173] J.R. Michael, Focused Ion Beam Induced Microstructural Alterations: Texture Development, Grain Growth, and Intermetallic Formation, Microsc. Microanal. 17 (2011) 386–397. <https://doi.org/10.1017/S1431927611000171>.
- [174] B.A. Benson, R.G. Hoagland, Crack growth behavior of a high strength aluminum alloy during LME by gallium, Scr. Metall. 23 (1989) 1943–1948. [https://doi.org/10.1016/0036-9748\(89\)90487-0](https://doi.org/10.1016/0036-9748(89)90487-0).
- [175] N. Tsutsui, H. Koizumi, Intergranular / transgranular fracture in the liquid metal embrittlement of polycrystalline embrittlement of polycrystalline zinc, Procedia Struct. Integr. 13 (2018) 849–854. <https://doi.org/10.1016/j.prostr.2018.12.162>.
- [176] S. Tan, R. Livengood, P. Hack, R. Hallstein, D. Shima, J. Notte, S. McVey, Nanomachining with a focused neon beam: A preliminary investigation for semiconductor circuit editing and failure analysis, J. Vac. Sci. Technol. B, Nanotechnol. Microelectron. Mater. Process. Meas. Phenom. 29 (2011). <https://doi.org/10.1116/1.3660797>.
- [177] J. Notte, B. Ward, N. Economou, R. Hill, R. Percival, L. Farkas, S. McVey, An introduction to the helium ion microscope, AIP Conf. Proc. 931 (2007) 489–496. <https://doi.org/10.1063/1.2799423>.
- [178] L. Scipioni, D.C. Ferranti, V.S. Smentkowski, R.A. Potyrailo, Fabrication and initial characterization of ultrahigh aspect ratio vias in gold using the helium ion microscope, J. Vac. Sci. Technol. B, Nanotechnol. Microelectron. Mater. Process. Meas. Phenom. 28 (2010) C6P18–C6P23. <https://doi.org/10.1116/1.3517514>.
- [179] G. Hlawacek, V. Veligura, R. van Gastel, B. Poelsema, Helium ion microscopy, J. Vac. Sci. Technol. B, Nanotechnol. Microelectron. Mater. Process. Meas. Phenom. 32 (2014) 39-1-39–11. <https://doi.org/10.1116/1.4863676>.
- [180] F.I. Allen, A review of defect engineering, ion implantation, and nanofabrication using the helium ion microscope, Beilstein J. Nanotechnol. 12 (2021) 633–664.

<https://doi.org/10.3762/BJNANO.12.52>.

- [181] S. He, R. Tian, W. Wu, W. Di Li, D. Wang, Helium-ion-beam nanofabrication: Extreme processes and applications, *Int. J. Extrem. Manuf.* 3 (2020). <https://doi.org/10.1088/2631-7990/abc673>.
- [182] F.H.M. Rahman, S. McVey, L. Farkas, J.A. Notte, S. Tan, R.H. Livengood, The prospects of a subnanometer focused neon ion beam, *Scanning.* 34 (2012) 129–134. <https://doi.org/10.1002/sca.20268>.
- [183] R.H. Livengood, S. Tan, R. Hallstein, J. Notte, S. McVey, F.H.M. Faridur Rahman, The neon gas field ion source - A first characterization of neon nanomachining properties, *Nucl. Instruments Methods Phys. Res. Sect. A Accel. Spectrometers, Detect. Assoc. Equip.* 645 (2011) 136–140. <https://doi.org/10.1016/j.nima.2010.12.220>.
- [184] S. Tan, R. Livengood, D. Shima, J. Notte, S. McVey, Gas field ion source and liquid metal ion source charged particle material interaction study for semiconductor nanomachining applications, *J. Vac. Sci. Technol. B, Nanotechnol. Microelectron. Mater. Process. Meas. Phenom.* 28 (2010) C6F15-C6F21. <https://doi.org/10.1116/1.3511509>.
- [185] D. Xia, Y.B. Jiang, J. Notte, D. Runt, GaAs milling with neon focused ion beam: Comparison with gallium focused ion beam milling and subsurface damage analysis, *Appl. Surf. Sci.* 538 (2021). <https://doi.org/10.1016/j.apsusc.2020.147922>.
- [186] N. Klingner, G. Hlawacek, P. Mazarov, W. Pilz, F. Meyer, L. Bischoff, Imaging and milling resolution of light ion beams from helium ion microscopy and FIBs driven by liquid metal alloy ion sources, *Beilstein J. Nanotechnol.* 11 (2020) 1742–1749. <https://doi.org/10.3762/bjnano.11.156>.
- [187] H. Guo, H. Itoh, C. Wang, H. Zhang, D. Fujita, Focal depth measurement of scanning helium ion microscope, *Appl. Phys. Lett.* 105 (2014). <https://doi.org/10.1063/1.4890390>.
- [188] T. Wirtz, P. Philipp, J.N. Audinot, D. Dowsett, S. Eswara, High-resolution high-sensitivity elemental imaging by secondary ion mass spectrometry: From traditional 2D and 3D imaging to correlative microscopy, *Nanotechnology.* 26 (2015). <https://doi.org/10.1088/0957-4484/26/43/434001>.
- [189] Y. Drezner, Y. Greenzweig, A. Raveh, Strategy for focused ion beam compound material removal for circuit editing, *J. Vac. Sci. Technol. B, Nanotechnol. Microelectron. Mater. Process. Meas. Phenom.* 30 (2012). <https://doi.org/10.1116/1.3674280>.
- [190] M. Kolíbal, T. Matlocha, T. Vystavěl, T. Šikola, Low energy focused ion beam milling of silicon and germanium nanostructures, *Nanotechnology.* 22 (2011). <https://doi.org/10.1088/0957-4484/22/10/105304>.
- [191] M. Rauscher, E. Plies, Low energy focused ion beam system design, *J. Vac. Sci. Technol. A Vacuum, Surfaces, Film.* 24 (2006) 1055–1066. <https://doi.org/10.1116/1.2208989>.
- [192] E. Oliviero, S. Peripolli, P.F.P. Fichtner, L. Amaral, Characterization of neon implantation damage in silicon, *Mater. Sci. Eng. B.* 112 (2004) 111–115.

<https://doi.org/10.1016/j.mseb.2004.05.014>.

- [193] A.G. Cullis, T.E. Seidel, R.L. Meek, Comparative study of annealed neon-, argon-, and krypton-ion implantation damage in silicon, *J. Appl. Phys.* 49 (1978) 5188–5198. <https://doi.org/10.1063/1.324414>.
- [194] S. Peripolli, E. Oliviero, P.F.P. Fichtner, M.A.Z. Vasconcellos, L. Amaral, Characterization of neon cavity in silicon, *Nucl. Instruments Methods Phys. Res. Sect. B Beam Interact. with Mater. Atoms.* 242 (2006) 494–497. <https://doi.org/10.1016/j.nimb.2005.08.138>.
- [195] E. Oliviero, S. Peripolli, L. Amaral, P.F.P. Fichtner, M.F. Beaufort, J.F. Barbot, S.E. Donnelly, Damage accumulation in neon implanted silicon, *J. Appl. Phys.* 100 (2006). <https://doi.org/10.1063/1.2220644>.
- [196] H.O. Funsten, S.M. Ritzau, R.W. Harper, J.E. Borovsky, R.E. Johnson, Energy loss by keV ions in silicon, *Phys. Rev. Lett.* 92 (2004) 2–5. <https://doi.org/10.1103/PhysRevLett.92.213201>.
- [197] N. Imanishi, S. Ninomiya, Nuclear and Electronic Sputtering Induced by High Energy Heavy Ions, *J. Nucl. Radiochem. Sci.* 5 (2004) R9–R17. <https://doi.org/10.14494/jnrs2000.5.r9>.
- [198] T. Wirtz, O. De Castro, J.N. Audinot, P. Philipp, Imaging and Analytics on the Helium Ion Microscope, *Annu. Rev. Anal. Chem.* 12 (2019) 523–543. <https://doi.org/10.1146/annurev-anchem-061318-115457>.
- [199] L. Pelaz, L.A. Marqués, J. Barbolla, Ion-beam-induced amorphization and recrystallization in silicon, *J. Appl. Phys.* 96 (2004) 5947–5976. <https://doi.org/10.1063/1.1808484>.
- [200] R. Livengood, S. Tan, Y. Greenzweig, J. Notte, S. McVey, Subsurface damage from helium ions as a function of dose, beam energy, and dose rate, *J. Vac. Sci. Technol. B Microelectron. Nanom. Struct. Process. Meas. Phenom.* 27 (2009) 3244–3249. <https://doi.org/10.1116/1.3237101>.
- [201] C.M. Gonzalez, R. Timilsina, G. Li, G. Duscher, P.D. Rack, W. Slingenbergh, W.F. van Dorp, J.T.M. De Hosson, K.L. Klein, H.M. Wu, L.A. Stern, Focused helium and neon ion beam induced etching for advanced extreme ultraviolet lithography mask repair, *J. Vac. Sci. Technol. B, Nanotechnol. Microelectron. Mater. Process. Meas. Phenom.* 32 (2014). <https://doi.org/10.1116/1.4868027>.
- [202] R. Li, R. Zhu, S. Chen, C. He, M. Li, J. Zhang, P. Gao, Z. Liao, J. Xu, Study of damage generation induced by focused helium ion beam in silicon, *J. Vac. Sci. Technol. B, Nanotechnol. Microelectron. Mater. Process. Meas. Phenom.* 37 (2019). <https://doi.org/10.1116/1.5096908>.
- [203] M.G. Stanford, B.B. Lewis, V. Iberi, J.D. Fowlkes, S. Tan, R. Livengood, P.D. Rack, In Situ Mitigation of Subsurface and Peripheral Focused Ion Beam Damage via Simultaneous Pulsed Laser Heating, *Small.* 12 (2016) 1779–1787. <https://doi.org/10.1002/smll.201503680>.

- [204] M.A. Nguyen, M.O. Ruault, F. Fortuna, Formation and growth of nanocavities and cavities induced by He⁺ implantation in silicon, *Adv. Nat. Sci. Nanosci. Nanotechnol.* 3 (2012). <https://doi.org/10.1088/2043-6262/3/1/015015>.
- [205] J.H. Evans, A. Van Veen, C.C. Griffioen, The annealing of helium-induced cavities in silicon and the inhibiting role of oxygen, *Nucl. Inst. Methods Phys. Res. B.* 28 (1987) 360–363. [https://doi.org/10.1016/0168-583X\(87\)90176-5](https://doi.org/10.1016/0168-583X(87)90176-5).
- [206] M.F. Beaufort, J.F. Barbot, M. Drouet, S. Peripolli, E. Oliviero, L. Amaral, P.F.P. Fichtner, Nanocavities induced by neon Plasma Based Ion Implantation in silicon, *Nucl. Instruments Methods Phys. Res. Sect. B Beam Interact. with Mater. Atoms.* 257 (2007) 750–752. <https://doi.org/10.1016/j.nimb.2007.01.128>.
- [207] P. Grünewald, J. Rauber, M. Marx, C. Motz, F. Schaefer, Fatigue crack growth in micro specimens as a tool to measure crack–microstructure interactions, *Fatigue Fract. Eng. Mater. Struct.* 43 (2020) 3037–3049. <https://doi.org/10.1111/ffe.13354>.
- [208] E. Okotete, S. Brinckmann, S. Lee, C. Kirchlechner, How to avoid FIB-milling artefacts in micro fracture? A new geometry for interface fracture, *Mater. Des.* 232 (2023) 112134. <https://doi.org/10.1016/j.matdes.2023.112134>.
- [209] Y. Hu, J.H. Huang, J.M. Zuo, In situ characterization of fracture toughness and dynamics of nanocrystalline titanium nitride films, *J. Mater. Res.* 31 (2016) 370–379. <https://doi.org/10.1557/jmr.2016.4>.
- [210] Dassault Systèmes Simulia Corp., Analysis User’s Manual Volume 1: Introduction, Spatial modeling, execution and output, Abaqus 6.12. I (2012) 831.
- [211] J.M. Whitney, C.E. Browning, W. Hoogsteden, Double Cantilever Beam Tests for Characterizing Mode I Delamination of Composite Materials., *J. Reinf. Plast. Compos.* 1 (1982) 297–313. <https://doi.org/10.1177/073168448200100402>.
- [212] H.W. Andresen, A.T. Echtermeyer, Critical energy release rate for a CSM reinforced carbon fibre composite/steel bonding, *Compos. Part A Appl. Sci. Manuf.* 37 (2006) 742–751. <https://doi.org/10.1016/j.compositesa.2005.06.009>.
- [213] Y.W. Mai, B.R. Lawn, Crack Stability and Toughness Characteristics in Brittle Materials., *Annu. Rev. Mater. Sci.* 16 (1986) 415–4239. <https://doi.org/10.1146/annurev.ms.16.080186.002215>.
- [214] J.L. Mead, M. Lu, H. Huang, Microscale interfacial adhesion assessment in a multilayer by a miniaturised four-point bending test, *Mech. Mater.* 129 (2019) 341–351. <https://doi.org/10.1016/j.mechmat.2018.12.003>.
- [215] J.W. Hutchinson, MIXED MODE FRACTURE MECHANICS OF INTERFACES, in: *Met. Interfaces*, Elsevier, 1990: pp. 295–306. <https://doi.org/10.1016/B978-0-08-040505-6.50037-4>.
- [216] L. Banks-Sills, 50th anniversary article: Review on interface fracture and delamination of composites, *Strain.* 50 (2014) 98–110. <https://doi.org/10.1111/str.12082>.

- [217] M. Charalambides, A.J. Kinloch, Y. Wang, J.G. Williams, On the analysis of mixed-mode failure, *Int. J. Fract.* 54 (1992) 269–291. <https://doi.org/10.1007/BF00035361>.
- [218] V. Stamos, V. Kostopoulos, S.D. Peteves, Fracture Criteria for Interface Cracks. A Case Study, *Interfacial Sci. Ceram. Join.* (1998) 267–279. https://doi.org/10.1007/978-94-017-1917-9_23.
- [219] J.W. Hutchinson, *Advances in Applied Mechanics*, Volume 16, 1976., 1976.
- [220] R.O. Ritchie, R.M. Cannon, B.J. Dalgleish, R.H. Dauskardt, J.M. McNaney, Mechanics and mechanisms of crack growth at or near ceramic-metal interfaces: interface engineering strategies for promoting toughness, *Mater. Sci. Eng. A.* 166 (1993) 221–235. [https://doi.org/10.1016/0921-5093\(93\)90325-9](https://doi.org/10.1016/0921-5093(93)90325-9).
- [221] J.W. Hutchinson, M.E. Mear, J.R. Rice, Crack paralleling an interface between dissimilar materials, *J. Appl. Mech. Trans. ASME.* 54 (1987) 828–832. <https://doi.org/10.1115/1.3173124>.
- [222] H. Ming-Yuan, J.W. Hutchinson, Crack deflection at an interface between dissimilar elastic materials, *Int. J. Solids Struct.* 25 (1989) 1053–1067. [https://doi.org/10.1016/0020-7683\(89\)90021-8](https://doi.org/10.1016/0020-7683(89)90021-8).
- [223] D. Picard, D. Leguillon, C. Putot, A method to estimate the influence of the notch-root radius on the fracture toughness measurement of ceramics, *J. Eur. Ceram. Soc.* 26 (2006) 1421–1427. <https://doi.org/10.1016/j.jeurceramsoc.2005.02.016>.
- [224] H. Yu, G.B. Thompson, C.R. Weinberger, The role of chemistry and bonding in regulating fracture in multiphase transition metal carbides and nitrides, *Extrem. Mech. Lett.* 17 (2017) 1–6. <https://doi.org/10.1016/j.eml.2017.09.004>.
- [225] S.B. Bhaduri, F.F.Y. Wang, Fracture surface energy determination in {1 1 0} planes in silicon by the double torsion method, *J. Mater. Sci.* 21 (1986) 2489–2492. <https://doi.org/10.1007/BF01114295>.
- [226] J.A. Hauch, D. Holland, M.P. Marder, H.L. Swinney, Dynamic fracture in single crystal silicon, *Phys. Rev. Lett.* 82 (1999) 3823–3826. <https://doi.org/10.1103/PhysRevLett.82.3823>.
- [227] R. Pérez, P. Gumbsch, Directional anisotropy in the cleavage fracture of silicon, *Phys. Rev. Lett.* 84 (2000) 5347–5350. <https://doi.org/10.1103/PhysRevLett.84.5347>.
- [228] A.A. Stekolnikov, J. Furthmüller, F. Bechstedt, Absolute surface energies of group-IV semiconductors: Dependence on orientation and reconstruction, *Phys. Rev. B - Condens. Matter Mater. Phys.* 65 (2002) 1–10. <https://doi.org/10.1103/PhysRevB.65.115318>.
- [229] A. Sherman, In situ removal of native oxide from silicon wafers, *J. Vac. Sci. Technol. B Microelectron. Process. Phenom.* 8 (1990) 656–657. <https://doi.org/10.1116/1.584991>.
- [230] C. Lin, *Encyclopedia of Microfluidics and Nanofluidics*, *Encycl. Microfluid. Nanofluidics.* (2013) 1–11. <https://doi.org/10.1007/978-3-642-27758-0>.

- [231] M. Morita, T. Ohmi, E. Hasegawa, M. Kawakami, M. Ohwada, Growth of native oxide on a silicon surface, *J. Appl. Phys.* 68 (1990) 1272–1281. <https://doi.org/10.1063/1.347181>.
- [232] T. Rouxel, S. Yoshida, The fracture toughness of inorganic glasses, *J. Am. Ceram. Soc.* 100 (2017) 4374–4396. <https://doi.org/10.1111/jace.15108>.
- [233] C. Bjerkén, C. Persson, Numerical method for calculating stress intensity factors for interface cracks in bimetals, *Eng. Fract. Mech.* 68 (2001) 235–246. [https://doi.org/10.1016/S0013-7944\(00\)00098-9](https://doi.org/10.1016/S0013-7944(00)00098-9).
- [234] P. Albrecht, K. Yamada, Rapid Calculation of Stress Intensity Factors, *ASCE J Struct Div.* 103 (1977) 377–389. <https://doi.org/10.1061/jsdeag.0004556>.
- [235] E.F. Rybicki, M.F. Kanninen, A finite element calculation of stress intensity factors by a modified crack closure integral, *Eng. Fract. Mech.* 9 (1977) 931–938. [https://doi.org/10.1016/0013-7944\(77\)90013-3](https://doi.org/10.1016/0013-7944(77)90013-3).
- [236] A.Y.T. Leung, Z. Zhou, X. Xu, Determination of stress intensity factors by the finite element discretized symplectic method, *Int. J. Solids Struct.* 51 (2014) 1115–1122. <https://doi.org/10.1016/j.ijsolstr.2013.12.017>.
- [237] J.R. Rice, A path independent integral and the approximate analysis of strain concentration by notches and cracks, *J. Appl. Mech. Trans. ASME.* 35 (1968) 379–388. <https://doi.org/10.1115/1.3601206>.
- [238] RICE J. R. and Rosengren G.F, Plane strain deformation near a crack tip in a power-law hardening material, *J. Mech. Phys. SolidsMechanics.* 16 (1968) 1 to 12. [https://doi.org/https://doi.org/10.1016/0022-5096\(68\)90013-6](https://doi.org/https://doi.org/10.1016/0022-5096(68)90013-6).
- [239] J.W. Hutchinson, Singular behaviour at the end of a tensile crack in a hardening material, *J. Mech. Phys. Solids.* 16 (1968) 13–31.
- [240] Abaqus CAE/User's Manual, 6.11, Simulia, 2011.
- [241] Michael Smith, ABAQUS / CAE User ' s Manual, ABAQUS/CAE User's Man. (2001) 1–847.
- [242] A. Masolin, P.O. Bouchard, R. Martini, M. Bernacki, Thermo-mechanical and fracture properties in single-crystal silicon, *J. Mater. Sci.* 48 (2013) 979–988. <https://doi.org/10.1007/s10853-012-6713-7>.

Appendix

Contribution of co-authors

Chapter 3: Optimisation of bridge notch geometry in single cantilever beams: an approach for minimising FIB artefacts

E. Okotete: Conceptualization, Investigation, Formal analysis, Writing - original draft.

S. Brinckmann: Formal analysis, Writing - review & editing.

S. Lee: Conceptualization, Methodology, Formal analysis, Writing - review & editing.

C. Kirchlechner: Conceptualization, Formal analysis, Supervision, Writing - review & editing, Funding acquisition.

Chapter 4: Role of notching ion species on fracture toughness of single crystalline silicon

E. Okotete: Conceptualization, Investigation, Formal analysis, Writing - original draft.

S. Lee: Conceptualization, Methodology, Formal analysis, Writing - review & editing.

C. Kirchlechner: Conceptualization, Formal analysis, Supervision, Writing - review & editing, Funding acquisition.

Chapter 5: Novel single cantilever delamination geometry for fracture toughness measurements

E. Okotete: Conceptualization, Investigation, Formal analysis, Writing - original draft.

S. Brinckmann: Formal analysis, Writing - review & editing.

S. Lee: Methodology, Formal analysis, Writing - review & editing.

C. Kirchlechner: Conceptualization, Methodology, Formal analysis, Supervision, Writing - review & editing, Funding acquisition.

Chapter 6: Numerical analysis of the single cantilever delamination (SCD) geometry

E. Okotete: Conceptualization, Investigation, Formal analysis, Writing - original draft.

S. Lee: Formal analysis, Writing - review & editing.

S. Brinckmann: Conceptualization, Methodology, Formal analysis, Writing - review & editing.

C. Kirchlechner: Conceptualization, Formal analysis, Supervision, Writing - review & editing, Funding acquisition.

List of Publications

- 2024 **E. Okotete**, S. Brinckmann, J. Hohmann, M. Kohl, S. Lee, C. Kirchlechner, “Optimisation of bridge notch geometry in single cantilever beams: an approach for minimising FIB artefacts”, *in preparation*, 2024
- 2024 **E. Okotete**, S. Mück, S. Lee, C. Kirchlechner, “Role of notching ion species on fracture toughness of single crystalline silicon”, *in preparation*, 2024
- 2024 **E. Okotete**, S. Lee, S. Brinckmann, C. Kirchlechner, “Numerical analysis of single cantilever delamination (SCD) geometry”, *in preparation*, 2024
- 2023 **E. Okotete**, S. Brinckmann, S. Lee, C. Kirchlechner, “How to avoid FIB-milling artefacts in micro fracture? A new geometry for interface fracture,” *Materials Design* 232 (2023) 112134.
- 2021 K. Alaneme, S. Babalola, M. Bodunrin, L. Chown, **E. Okotete**, N. Maledi, “Hot deformation of nickel particles reinforced aluminium based composites: flow behaviour, microstructural evolution and processing map analyses”, *Materials Research Express* 8 (1) (2021) 016510
- 2017 K. Alaneme, **E. Okotete**, N. Maledi, “Phase characterisation and mechanical behaviour of Fe–B modified Cu–Zn–Al shape memory alloys”, *Journal of Materials Research and Technology* 6 (2) (2017) 136-146
- 2017 K. Alaneme, **E. Okotete**, M. Bodunrin, “Microstructural analysis and corrosion behaviour of Fe, B, and Fe-B-modified Cu-Zn-Al shape memory alloys”, *Corrosion Reviews* 35 (1) (2017) 3-11
- 2016 K. Alaneme, **E. Okotete**, “Reconciling viability and cost-effective shape memory alloy options – A review of copper and iron based shape memory metallic systems”, *Engineering Science and Technology, an International Journal* 19(3) (2016) 1582-1592